UNIVERSITEIT ANTWERPEN
Faculteit Wetenschappen
Departement Fysica

Combining the modified local density approach with variational calculus: a flexible tandem for studying electron transport in nano-devices

---

De lokale dichtheidsbenadering in combinatie met variatierekening: een flexibele tandem voor de studie van elektronentransport in nano-componenten

Proefschrift ingediend ter verkrijging van de graad van
Doctor in de Wetenschappen
aan de Universiteit Antwerpen, te verdedigen door

Hamilton Carrillo Nuñez

Promoters
Prof. dr. Wim Magnus,
Prof. dr. François M. Peeters

Antwerpen, December 2012

Members of the Jury:
Chairman
Prof. dr. Wim Wenseleers, Universiteit Antwerpen,Belgium
Promotors
Prof. dr. Wim Magnus, Universiteit Antwerpen, Belgium
Prof. dr. François. M. Peeters, Universiteit Antwerpen, Belgium
Members
Prof. dr. Nick van Remortel, Universiteit Antwerpen, Belgium
Prof. dr. Bart Partoens, Universiteit Antwerpen, Belgium
Dr. Geert Eneman, imec, Belgium
Prof. dr. Wil H. A. Schilders, Technische Universiteit Eindhoven, Netherlands.

Contact Information
Hamilton Carrillo Nuñez
Universiteit Antwerpen
Departement Fysica
Groenenborgerlaan 171
2020 Antwerpen
Belgium
hacarrillo@gmail.com

Acknowledgement

The first person I would like to thank is professor François Peeters for having given me the great opportunity to pursuit my Ph.D in the condensed matter theory group at Antwerpen. I would also like to thank Hilde Evans, who helped me on numerous administrative issues with a lot of patience.

I would like to express my deep gratitude to my advisor professor Wim Magnus. His continuous support, patient guidance and enthusiastic encouragement helped me during the past 4 years. Also, his comments on my Ph.D thesis, these last months, not only were fruitful, but also will improve my future academic writing. All these could not have been possible without his kind supervision.

Besides my promotors, I am grateful to professors Wim Wenseleers, Nick van Remortel, Bart Partoens, Geert Eneman and Wil H. A. Schilders for willing to be the members of the jury.

I would like to thank so much to my flatmates Ricardo Egoavil and William Muñoz for the wonderful living environment at the G199, it was like being at home. Also, to all my colleagues at the CMT group, specially to my good old friend Eduardo Galvan for all useful discussions I had with him during the last years.

Finally, I own a very special thank to my lovely friend Lucie Soulard. Without her help, understanding and patience, my early stay in Europe would have been harder. For that and much more, Merci beaucoup Lucie !

This work was supported by Flemish Science Foundation FWO-VI and the Interuniversity Attraction Poles, Belgium State, Belgium Science Policy.

Antwerpen, December 2012

Hamilton Carrillo Nuñez

Table of Contents

List of Acronyms

A

AC	Acoustic

B

BTE	Boltzmann transport equation
BTBT	Band-to-band tunneling

C

CMOS	Complementary Metal-oxide-silicon

E

EMA	Effective mass approximation

G

GNR	Graphene nanoribbon
GNRFET	Graphene nanoribbon field-effect transistor

L

LDA	Local density approximation

M

MOSFET	Metal-oxide-silcion field-effect transistor
MLDA	Modified local density approximation
MCC	Method of characteristic curves

N

NEGF	Non-equilibrium Green function

O

1D	One dimensional

R

Ref.	Reference

S

SR	Surface roughness

T

3D	Three dimensional
TB	Tight-binding
TFET	Tunneling field-effect transistor

W

WTE	Wigner transport equation

1 Introduction

1.1 Overview

The 20th century will be remembered as the golden century for the electronics industry. Starting with the radio in 1901 and followed by the invention of the transistor in Bell Labs 1948, Shockley, Brattain and Bardeen were awarded with the Nobel prized in physics in 1956. Due to the small size of the transistor, the new *microelectronics* area was born. The materials used for the fabrication of such devices are the well-known semiconductors, e.g. silicon. During the 1950's, the integrated circuits came into existence. In the history of the microelectronics this industry was an important development since it improved the efficiency and power of the electronic devices. Inside an integrated circuit many transistors can be located on a single silicon chip, and over the years the number of transistors increased while the size scaled down. During the 1970s, it was already possible to incorporate complicated circuits to create the small microprocessor allowing the miniaturization of devices, a key concept for the industry. The downscaling of semiconductor devices was noticeable so that the Intel co-founder Gordon E. Moore described the trend in his 1965 paper [1]. He stated that the number of components integrated circuits had doubled every year from the invention of the integrated circuit in 1958 until 1965 and suggested that the trend would continue for at least ten years, i.e. until 1975. The latter is known as *Moore's law*, named after him. Moore's law has proved to be surprisingly accurate and continued already for more than half a century. Moreover, the law has been used

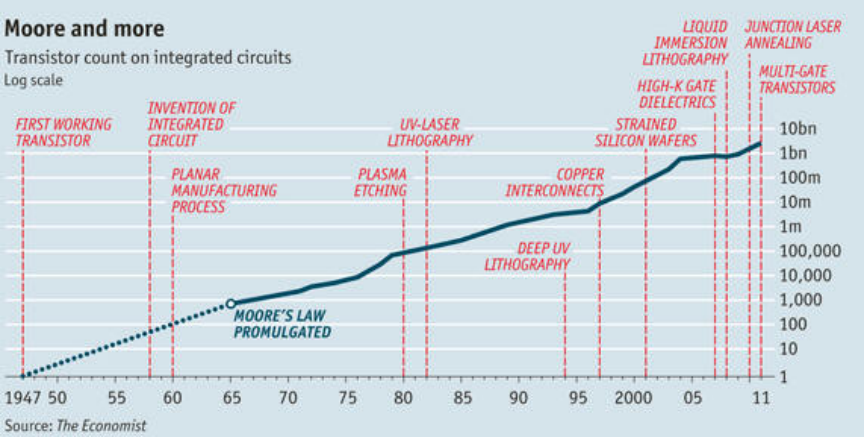

(a)

(b)

Figure 1.1: (a) Moore's law: Plot of transistor count on integrated circuits as a function of the date of introduction. (b) An Osborne executive portable computer, from 1982 with a Zilog Z80 4MHz CPU, and a 2007 Apple iPhone with a 412MHz ARM11 CPU. The Executive weights 100 times more and is nearly 500 times larger in volume.

in the semiconductor industry roadmaps and to achieve targets for research and development in the market.

Nowadays, technology is an important part of our life. We find electronics devices everywhere we go or we see. It looks like we are immersed in an ocean of technology, and sometimes we do not image how it would be to live without them. It is amazing what a "simple" phone can do these days, much smaller and faster than the fastest regular desktop PC at the beginning of the 2000's and just to compare, 500 times smaller and 200 times faster than one of the first portable computer in 1982, see Fig. 1.1. This has been made possible

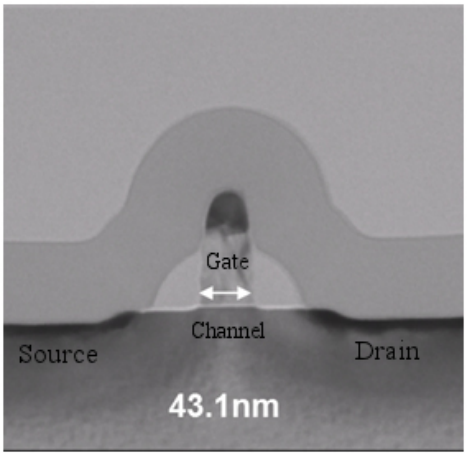

Figure 1.2: MOSFET fabricated on a planar bulk silicon structure.

due to the continuous miniaturization of transistors which in turn not only enhance their performance but also reduce the cost of its production. The latter requires innovations and improvements in the fabrication techniques of devices accompanied with technological support in order to satisfy the fast growing market of electronic products in the semiconductor industry. Over the years the number of transistors on chips increased dramatically, from Intels first commercial processor containing only 3500, until the current ability to jam as many as 2.2 billion transistors in 2011. However, the downscaling of transistors has pointed out some important issues and challenges during the manufacturing of devices and structures. For instance, with the scaling of a planar bulk metal-oxide-semiconductor field-effect-transistor (MOSFET), as depicted in Fig. 1.2, the doping concentration of the channel will need to be increased to undesirably high levels in order to gain adequate control of short-channel effects and to set the threshold voltage properly. As a result of the high channel doping, the mobility of holes and electrons will be reduced and the junction leakage due to band-to-band tunneling (BTBT) will increase. Moreover, with scaling planar bulk MOSFETs, advanced devices such as multiple-gates, particularly TriGate MOSFETs or nanowire MOSFETs, as depicted in Fig. 1.3, are considered candidates to overcome the downscaling challenges. Lately, Intel has announced the commercialization of a 22nm TriGate transistor [2]. They have found that the 22nm TriGate transistor performs better and uses less energy than the current 32nm planar transistor. Such development keeps Moore's Law alive, however, as D. K. Ferry claims in his paper "*Nanowires in Nanoelectronics*" [3], this evolution cannot continue down this same path much longer due to the "end of the road" that has led many to seek an alternative to the ubiquitous silicon transistor.

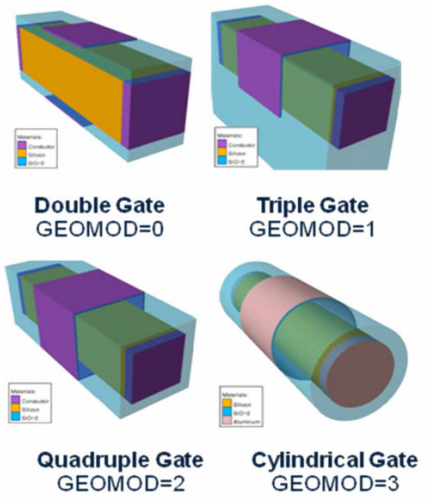

Figure 1.3: Different multi-gate architectures.

Among the candidates are the nanowires transistors. These nanowires can be carbon nanotubes or are made from silicon, as well as a variety of other semiconductors, thanks to new technologies, there are remarkable expectations for the usefulness of these nanowires.

1.2 Nanowires for electronic devices

If a structure has one of its dimensions less than 100 nm, it is considered a nanostructure. Among these nanostructures, we find the nanowires that are obtained by reducing the dimensionality of the electron's environment from a two-dimensional quantum well to one-dimensional, therefore the electron (or hole) is free to move in only one direction as sketched in Fig. 1.4(a) showing an example of silicon nanowires [4]. Nowadays nanowires are being fabricated by many groups around the world [4–6], and it is expected that the future transistor architecture would be built of relatively thin silicon nanowires that would form the transistor channel, surrounded on all sides by a wraparound silicon oxide and a high-K metal gate, as observed in Fig. 1.4(b). The silicon nanowire transistor has been considered as "The Next Big Thing in design chips" by Mukesh Khare, the IBM's director of semiconductor technology research, at the Common Platform Technology Forum (CPTF) 2012. So far, the planar MOSFETs has powered chips for many process generations, and are now being replaced by the Intel's Fin/TriGate-FET. The cylindrical nanowire transistor, depicted in Fig. 1.3 and Fig. 1.4(b), has a the gate that is all-around the device looking like

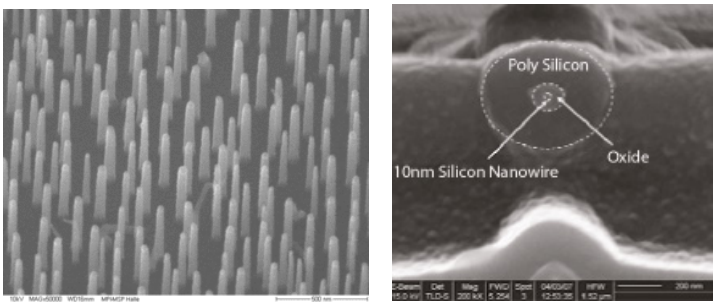

(a) (b)

Figure 1.4: (a) Epitaxial growth of silicon nanowires using an aluminum catalyst. (b) Scanning electron microscope image of the fabricated silicon nanowire transistor with 10nm diameter.

a kind of multiple-gate transistor with better electrostatic control capability and improved transport properties. According to Khare, there is very good R&D going on in research labs that is attempting to extend the 3D FinFET process integration and process technology into an ultimate nanowire technology. This does not mean that silicon nanowires will be introduced in commercial chips anytime soon since there is still a lot of issues concerning tweaking, optimizing and perfecting. Moreover, the latter remains to be accomplished with the FinFET-based chips, however, the FinFET is expected not to be an one-solution generation but a many-generation solutions.

1.3 MOSFETs and TFETs: differences and expectations

The down-scaling of MOSFETs has enabled extraordinary improvements in the switching speed, density, functionality and cost of microprocessors, however, MOSFET technology is facing two major problems that results in high power energy consumption: the increasing difficulty in reducing the supply voltage, and the rising leakage current that degrade the switching ratio of "on" and "off" currents, i.e. $I_{\mathrm{ON}}/I_{\mathrm{OFF}}$. In a MOSFET, the current switching process involves the thermionic (temperature-dependent) injection of electrons surmounting an energy barrier, and this limits the transition slope from the off state to the on state since today's MOSFET requires at least a subthreshold swing (SS) of $k_{\mathrm{B}}T\ln 10/e$ $\approx$ 60 mV decade^{-1} to increase the current by one order of magnitude at room temperature. Therefore, new devices, with a steep SS less than $k_{\mathrm{B}}T\ln 10/e$, are being proposed [7] and could be obtained by exploiting physical principles other

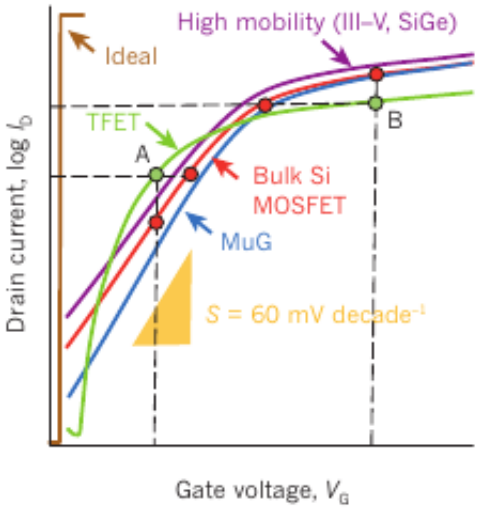

Figure 1.5: Qualitative comparison of three engineering solutions to improve the characteristics of the bulk silicon MOSFET switch (red): a multigate device (MuG, blue); a high-mobility channel (purple); and a TFET (green).

than thermionic injection. For instance Fig. 1.5, taken from Ref. [7], shows a qualitative comparison of some major candidates to improve the characteristics of bulk silicon MOSFET switches: multigate devices for improved electrostatics; high-mobility channels exploiting group III-V and SiGe materials; and TFETs that use quantum–mechanical BTBT to inject charge carriers into the device channel. At the operation point A, we may observe that the TFET offers not only improved $I_{\mathrm{ON}}/I_{\mathrm{OFF}}$ but also better performance, i.e. higher I_{ON} at the same voltage, or power savings at the same performance, i.e. lower voltage for the same I_{ON}, over the MOSFET. However, MOSFET still shows higher performance at the operation point B.

The TFET working principle is based on the charge carrier transfer from the valence band to the conduction band, for instance, near a $p^+ - i - n^+$ junction. This tunneling mechanism was first observed by Zener in 1934. In a TFET, the BTBT is switched on and off abruptly by controlling the band bending in the channel region by means of the gate bias as depicted in Fig. 1.6(a) where we show a planar $p^+ - i - n^+$ TFET. The dashed blue line in Fig. 1.6(b) shows the TFET off state when the valence band edge (E_{v}) inside the channel is located below the conduction band edge (E_{c}) of the source, so no BTBT occurs and the current is suppressed leading to small I_{OFF}–state. When a negative gate voltage is applied, the energy bands are pulled up, as depicted by the red line in

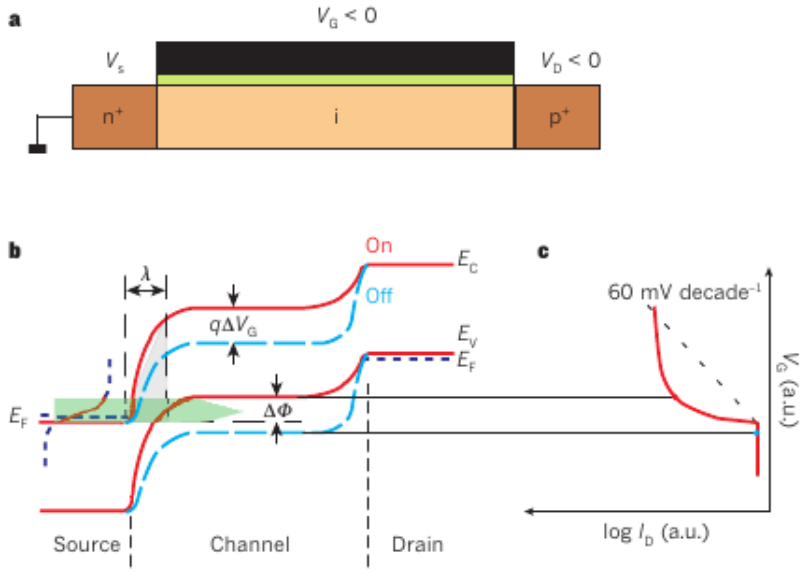

Figure 1.6: (a) Cross-section of a $p^+ - i - n^+$ TFET with applied source (V_S), gate (V_G) and drain (V_D) voltages. (b), The energy band profile for the off state (dashed blue lines) and the on state (red lines).

Fig. 1.6(b). Then, a conductive window $\Delta\Phi$ is opened when the channel valence band has lifted above the source conduction band, therefore carriers can now tunnel, from the filled states of the source into the empty states of the channel. This window $\Delta\Phi$ works as a filter which cuts off the high-energy part of the source Fermi distribution [8]. Then, the electron system is effectively "cooled down", acting as a MOSFET at a lower temperature. This filtering makes it possible to achieve a SS lower than 60 mV decade^{-1} (Fig. 1.6(c)). Moreover, in contrast to the MOSFET, a TFET has a slope that is not linear on a logarithmic scale due to the complex dependency of the tunnel current on the transmission probability through the potential barrier, as well as on the number of available states determined by the source and channel Fermi functions. Therefore, nowadays TFETs represent a promising steep-slope switch candidate offering significant power savings, however, it is still a big challenge to achieve high performance, i.e. high I_{ON}.

1.4 Outline

Due to the demanding device industry market, experiment is ahead of theoretical studies. So, it is important to study the nanodevice working principles from the theoretical point of view. For such purpose, many formalisms to deal with elec-

tronic transport have been developed. Among them, we may find: the Boltzmann transport equation, the Wigner transport equation, the non-equilibrium Green function method. Recently, a new approach has been introduced to study the BTBT mediated by phonon scattering in indirect semiconductors [9, 10] such as silicon. The latter formalisms, summarized in chapter 2, involve a self-consistent solution of Poisson and Schrödinger equations during the simulations of the device working principles. Moreover, when quantum effects are taken into account, as the case of nanowires, the simulations may become computationally very expensive. In this light, the present PhD work aims at proposing a numerical tool that accelerates the convergence of the self–consistent solution of Schrödinger and Poisson equations and the non-linear constitutive equations linking them, which is usually the most time consuming part in the simulations. Our approach is based on the modified local density approximation introduce by Paasch and Übensee in Ref. [11]. Then, using a non–linear variational principle, we have shown that the minimization of a suitable action yields a self–consistent solution of both Schrödinger and Poisson equations. This is explained in detail in chapter 3, where we have presented the modified local density approximation in combination with the non–linear variational principle providing a numerical algorithm for future implementation. Although, the modified local density approximation is used for the self–consistency, we have applied it to study electronic transport in different cylindrical nanowire devices. In chapter 4 and 5, we have investigated a cylindrical nanowire MOSFET. In these, we have expressed the current density, low-field mobility, low-field conductivity and scattering mechanisms such as surface roughness and electron–phonon interaction within the framework of the modified local density approximation. The latter can be evaluated once the potential is known from the self–consistency. Also, in chapter 4, in case of non–equilibrium, the Boltzmann transport equation has been solved analytically within the modified local density approximation for the ballistic steady–state by using the method of the characteristic curves as explained in appendix A.

Chapters 6 and 7 are devoted to the study of the phonon-assisted BTBT in silicon cylindrical nanowires by implementing the recent formalism introduced by Vandenberghe *et–al* in Refs. [9, 10]. In chapter 6, the Zener tunneling current through a $p - n$ junction embedded in a cylindrical silicon nanowire has been computed numerically. Unlike the other chapters, we have performed a full self-consistent solution of Poisson and Schrödinger equations. In chapter 7, the BTBT and its corresponding current density are expressed within the modified local density approximation for a cylindrical nanowire TFET. Evaluating the latter, we have found that the onset voltage strongly depends on the nanowire radius. It is worth to mention that although experiment for devices such as nanowire MOSFETs have been carried out, for instance see Refs. [4, 12], we have not made any comparison since we have focused more on the advantage of

our theoretical approach over the conventional methods as we will see during this Ph.D dissertation. However, we could implement our approach to study devices such as the Trigate-MOSFET where the MLDA is a reasonable approximation. Finally, the main conclusions as well as an outlook towards future research are given in the last chapter of this thesis.

2

Electronic transport in semiconductors

In semiconductors, the electric currents are due to the flow of electrons and holes under applied bias voltage, whereas transport is the process that describes the motion of charged carriers. Electronic transport in semiconductors can be very complicated depending on the size of the samples. Therefore, it is worth discussing charge transport within both the classical and quantum mechanical frameworks.

2.1 Boltzmann transport equation

At thermodynamic equilibrium, the statistical distribution of electrons is the Fermi-Dirac function

$$F(E) = \frac{1}{1 + \mathrm{e}^{(E-E_\mathrm{F})/k_\mathrm{B}T}}. \tag{2.1}$$

When an external force is applied, the electron distribution function is no longer described by the Fermi-Dirac function, but by a function $f_\mathbf{k}$ that depends on time, space and momentum. In the classical limit, the non-equilibrium function $f_\mathbf{k}$ is obtained by solving the Boltzmann transport equation (BTE)

$$\frac{\partial f_\mathbf{k}}{\partial t} + \mathbf{v} \cdot \nabla_\mathbf{r} f_\mathbf{k} + \frac{1}{\hbar}\mathcal{F} \cdot \nabla_\mathbf{k} f_\mathbf{k} = \left.\frac{\partial f_\mathbf{k}}{\partial t}\right|_{scat} \tag{2.2}$$

where $\mathbf{v}$ is the electron velocity and $\mathcal{F}$ is the external force acting on the system. The term labeled "scat" describes the distribution function due to the different

scattering mechanisms that is defined as

$$\left.\frac{\partial f_{\mathbf{k}}}{\partial t}\right|_{scat} = -\int \mathrm{d}\mathbf{k}' \left[f_{\mathbf{k}}(1-f_{\mathbf{k}'})W_{\mathbf{k},\mathbf{k}'} - f_{\mathbf{k}'}(1-f_{\mathbf{k}})W_{\mathbf{k}',\mathbf{k}}\right] \tag{2.3}$$

where the term $(1 - f_{\mathbf{k}(\mathbf{k}')})$ represents the probability of having a vacancy in the state $\mathbf{k}(\mathbf{k}')$ and $W_{\mathbf{k}',\mathbf{k}}(W_{\mathbf{k},\mathbf{k}'})$ are the rates at which the electron makes a transition from state $\mathbf{k}(\mathbf{k}')$ to state $\mathbf{k}'(\mathbf{k})$. The BTE allows us to describe many transport processes in semiconductors. However, it describes transport as a classical phenomena since the simultaneous description of position and momentum contradicts the Heisenberg uncertainty principle and, therefore, the BTE is not valid to tackle quantum effects such as tunneling.

2.1.1 Relaxation time approximation

In practice, the non-equilibrium distribution function $f_{\mathbf{k}}$ is obtained by solving numerically the BTE since an analytical solution is difficult to find due to the presence of scattering mechanisms. However, if one assumes a characteristic time τ, called relaxation time, to relax from the non-equilibrium state to the equilibrium state in the steady state, i.e. $\partial f_{\mathbf{k}}/\partial t = 0$, and that $f_{\mathbf{k}}$ is spatially uniform such that $\nabla_{\mathbf{r}} f_{\mathbf{k}} = 0$, the BTE is reduced to

$$\mathcal{F} \cdot \mathbf{v}_n \, f'(E_n(\mathbf{k})) = -\frac{f(E_n(\mathbf{k})) - F(E_n(\mathbf{k}))}{\tau_n}, \tag{2.4}$$

where the term $(1/\hbar)\nabla_{\mathbf{k}}$ has been replaced by $\mathbf{v}_n \, \partial/\partial E_n$, $E_n(\mathbf{k})$ being the energy dispersion relation while n is an index denoting all quantum numbers due to confinement. Moreover, if the external force is due to a constant applied electric field $\mathcal{F} = -e\mathcal{E}$ along the transport direction and weak enough to assume $f'(E_n(\mathbf{k})) \approx F'(E_n(\mathbf{k}))$, we can find that the low-field distribution function is

$$f_n(E) = F(E) + e\mathcal{E}\, F'(E)\, v_n(E)\tau_n(E). \tag{2.5}$$

Bearing in mind that the drift velocity is proportional to electric field, $v_{\mathrm{D}} = -\mu\mathcal{E}$, the proportionality constant μ, defined as the low-field mobility, can be computed from (2.5), that in case of a quasi-one-dimensional system such as a nanowire is written as

$$\mu = \frac{2e}{\pi n_{1\mathrm{D}}\hbar} \sum_n \int_{E_n}^{\infty} \frac{\mathrm{d}E}{4k_{\mathrm{B}}T} \frac{\tau_n(E)v_n(E)}{\cosh^2[(E-E_{\mathrm{F}})/2k_{\mathrm{B}}T]}, \tag{2.6}$$

where $n_{1\mathrm{D}}$ is the 1D electron density and all subband indices are included in n, whereas τ_n is the total relaxation time extracted from the Matthiessen's rule

$$\frac{1}{\tau_n} = \sum_j \frac{1}{\tau_n^j}. \tag{2.7}$$

In the latter, the summation is done for all scattering mechanisms being considered in the system, e.g. intra valley acoustic phonons, surface roughness, etc.

2.1.2 Method of characteristic curves

In case of inhomogeneous fields, there is no analytical solution for the BTE. Therefore, numerical approaches, i.e. such as the Monte Carlo method, should be implemented. Alternatively, in this work, we have invoked the method of characteristic curves (MCC) [13–15]. Briefly, the MCC is based on the classical trajectories $\mathbf{R}(t)$ and $\mathbf{P}(t)$ defined as

$$m\frac{\mathrm{d}\mathbf{R}(t)}{\mathrm{d}t} = \mathbf{P}(t), \quad \frac{\mathrm{d}\mathbf{P}(t)}{\mathrm{d}t} = \mathcal{F}[\mathbf{R}(t)] \tag{2.8}$$

with initial conditions $\mathbf{R}(0) = \mathbf{r}$ and $\mathbf{P}(0) = \mathbf{p}$. The latter allows to write the BTE as a total differential

$$\frac{\mathrm{d}\bar{f}(s)}{\mathrm{d}s} = \bar{\mathcal{R}}(s) \tag{2.9}$$

where $\bar{f}(s)$ is

$$\bar{f}(s) \overset{\text{def}}{=} f\left[\mathbf{R}(s), \mathbf{P}(s), T(s)\right], \quad T(s) \equiv t + s, \tag{2.10}$$

whereas $\bar{\mathcal{R}}(s)$ is related to the collision term in (2.2). Integrating (2.9) from $s = -t$ to $s = 0$ with $t > 0$ yields

$$f(\mathbf{r}, \mathbf{p}, t) = F(\mathbf{R}(-t), \mathbf{P}(-t)) + \int_0^t \mathrm{d}t'\, \bar{\mathcal{R}}(t' - t). \tag{2.11}$$

The latter is the non-equilibrium function at time t that takes into account all past trajectories between $-t$ and the initial time. In practice, the integral in (2.11) is carried out numerically by defining a grid time and implementing a quadrature procedure [15].

As we will see in chapter 4 and appendix A, a distribution function can be assigned to each subband in order to incorporate confinement quantum effects. As an example, we have solved the 1D ballistic-BTE analytically within the framework of the MCC only for the steady-state and extended it to the two-dimensional case of a cylindrical nanowire MOSFET. Nevertheless, the BTE can not deal with other quantum effects affecting electron propagation such as tunneling through a thin source-drain barrier in MOSFETs or Zener tunneling in case of TFET. Although the Wigner transport equation (WTE) is able to include such physical effects, we have not used it during the studies done in this thesis. Instead, we have applied the non-equilibrium Green function method and the new approach introduced by Vandenberghe *et–al* in Ref. [9, 10] to compute the Zener current in indirect semiconductors under inhomogeneous fields.

2.2 Non-equilibrium Green function method

Given the device Hamiltonian $H(\mathbf{r})$, its corresponding Green function can be computed by solving the differential equation

$$[E - H(\mathbf{r}) + i\eta]\, G(\mathbf{r}, \mathbf{r}'; E) = \delta(\mathbf{r} - \mathbf{r}'). \tag{2.12}$$

Numerically, the differential equation is solved by discretizing the spatial coordinates using the finite difference method, as schematically depicted in Fig. 2.1, so that the Green function can be written in a matrix form

$$[E - H + i\eta]\, G(E) = I, \tag{2.13}$$

where I is the identity matrix and H is the matrix representation of the Hamiltonian operator which is divided into $N + 2$ thin slices, with a finite number of transversal channels or modes. The slices with indices $n \leq 0$ and $n \geq N + 1$ represent the left and right leads, respectively. In principle, we could just invert the matrix $[E - H + i\eta]$ to obtain the Green function. However, the finite/infinite size of the matrix would depend on the boundary conditions of the system. For instance, $[E - H + i\eta]$ would be finite if we simply truncate the matrix by imposing finite leads, i.e. the one-electron wave function vanishes at the ends. Although, the latter would be an appropiate boundary condition if we had a infinite potential wall at the end of the leads, in a real device, we are actually dealing with open boundary conditions allowing for carrier transport. This is better described by periodic boundary conditions [16] which wrap the right lead around and connect it to the left making the device an artificially ring. If our insterest was limited only to close system there would be few reason to implement Green's functions. However, the active region of a real device is connected to semi-infinite leads, and the Green's function method allows to replace the effect of all external contacts with self-energies [16, 17] as we have described below in this section to handle properly the open boundary conditions as well as the infinite size of the matrix due to semi-infinite leads. First, we should reformulate the problem by defining the device Hamiltonian as

$$H = \begin{pmatrix} H_L & V_L & 0 \\ V_L^\dagger & H_D & V_R^\dagger \\ 0 & V_R & H_R \end{pmatrix} \tag{2.14}$$

where $H_L(H_R)$ is the Hamiltonian of the left (right) lead, whereas H_D represents the Hamiltonian of the active region of the device connected to the leads through

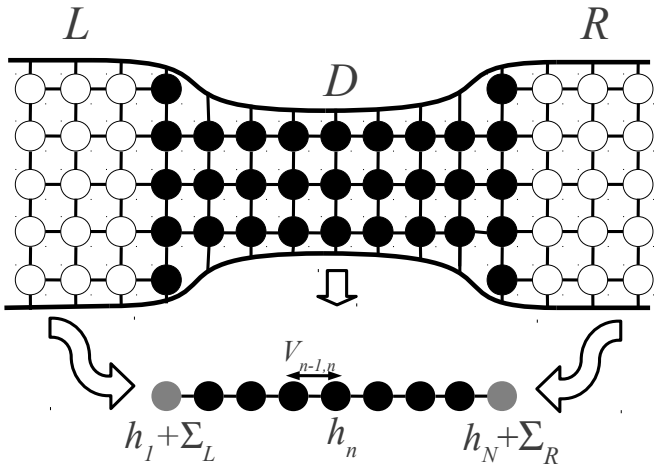

Figure 2.1: A device described by the Hamiltonian H_D, connected to the leads L and R. After discretization, the leads can be replaced by their corresponding self-energy terms added to the site energies $h_{1,N}$. $V_{i,j}$ is the coupling matrix between nearest neighbors sites.

the coupling matrices V_L and V_R. Inserting (2.14) into (2.13), we obtain

$$\begin{pmatrix} E+i\eta-H_L & V_L & 0 \\ V_L^\dagger & E-H_D & V_R^\dagger \\ 0 & V_R & E+i\eta-H_R \end{pmatrix} \begin{pmatrix} G_L & G_{LD} & G_{LR} \\ G_{DL} & G_D & G_{DR} \\ G_{RL} & G_{RD} & G_R \end{pmatrix} = I \tag{2.15}$$

where each element is a block sub matrix. For instance, the matrix $[E+i\eta-H_{L(R)}]$ represents the semi-infinite isolated left (right) lead, while the matrix $[E-H_D]$ represents the active region of the device. V_L and V_R are the coupling matrices that connect the left and right lead to the device, respectively. Solving the linear system of equations in (2.15), we may find an analytical expression for the Green function G_D that is the part we are interested in

$$G_D = [E - H_D - \Sigma_L - \Sigma_R]^{-1} \tag{2.16}$$

where the so called " self-energies" $\Sigma_{L,R}$ are defined as

$$\Sigma_L = V_L G_0^L V_L^\dagger, \quad \Sigma_R = V_R G_0^R V_R^\dagger, \tag{2.17}$$

whereas G_0^L and G_0^R are the Green function of the isolated left and right lead, respectively. Usually, these Green functions can be determined analytically only for a few trivial cases. However, there is always the option to compute them numerically by implementing a recursive approach [18].

Once the Green function is known, the transmission coefficient $T(E)$ can be evaluated as

$$T(E) = \mathrm{Tr}\left[\Gamma_L(E) G_D(E) \Gamma_R G_D^\dagger(E)\right] \tag{2.18}$$

where "Tr" represents the trace, while the matrices $\Gamma_{L,R}$ are given as

$$\Gamma_L \equiv i[\Sigma_L - \Sigma_L^\dagger], \quad \Gamma_R \equiv i[\Sigma_R - \Sigma_R^\dagger], \tag{2.19}$$

and determine the electron exchange rates between the active region and leads that in case of a MOSFET works as the source/drain reservoirs. Also, we can compute the spectral function that gives information about the density of states inside the device taking the leads into account,

$$A_L(E) = G_D(E)\Gamma_L G_D^\dagger(E), \quad A_R(E) = G_D(E)\Gamma_R G_D^\dagger(E). \tag{2.20}$$

As we will see in the next chapters, the non-equilibrium Green function method will be applied to compute the spectral functions (2.20) of the conduction and valence bands in nanowire devices with cylindrical geometry, specially in case of silicon-TFETs where the overlap between the spectral function of the conduction and valence bands is important for the band-to-band tunneling [9, 10].

2.2.1 Recursive Green function algorithm

Once the infinite leads have been eliminated, according to (2.16), all transport properties can be expressed in terms of quantities that are defined inside the active region of the device. Therefore, assuming that the decoupled Green functions denoted by G_0^L and G_0^R have been predetermined, and thus also their self-energies $\Sigma_{L,R}$, we can write $[E - H_D \ -\Sigma_L - \Sigma_R]$ as

$$\begin{pmatrix} E - h_1 - \Sigma_L & V_{1,2} & & & & & \\ V_{2,1}^\dagger & E - h_2 & V_{2,3} & & & & \\ & V_{3,2}^\dagger & E - h_3 & V_{3,4} & & & \\ & & \ddots & \ddots & \ddots & & \\ & & & V_{N-1,N-2}^\dagger & E - h_{N-1} & V_{N-1,N} & \\ & & & & V_{N,N-1}^\dagger & E - h_N - \Sigma_R \end{pmatrix}. \tag{2.21}$$

Although, the inversion of the latter, a finite-matrix, is a quite straightforward procedure, from the numerical point of view, this is a limitation since there will be an upper limit to the size of the matrices due to the number of sites we could handle. Alternatively, we may implement a recursive algorithm to calculate only the elements of the Green function we need for the transport properties, as well

as a LU descomposition of the band diagonal matrix (2.21) which requires a comparable compuatational effort. However, we have only implemented the recursive Green function method which is summarized as follows.

The Green function of the isolated slices should also be established before the recurrent calculations. In case of $n > 1$ and $n < N$, the latter is defined as $g_n \equiv [E - h_n]^{-1} = D_n^{-1}$. For the slices $n = 1, N$, the isolated Green function is $g_{1,N} \equiv [E - h_n - \Sigma_{L,R}]^{-1} = D_{1,N}^{-1}$, where, the leads are represented by their self-energies and have been added to the first and last sites. Then, the device connected to infinite leads has been replaced by an equivalent finite device with self-energy terms. From now on, we will use subscripts to denote spatial indices for the Green functions. Then, the total Green function $G_{i,j}(E)$ is the matrix Green function connecting the slices i and j. Notice that the subscript D has been dropped.

During the procedure to compute $G(E)$, it is necessary first to generate recursively two families of Green functions, $G_{i,j}^{LR}(E)$ and $G_{i,j}^{RL}(E)$, from left to right and vice versa, respectively. Starting with $G_{1,1}^{LR} = D_1^{-1}$, we may generate $G_{2,2}^{LR}, G_{3,3}^{LR}, \cdots, G_{N,N}^{LR}$ from

$$G_{i,i}^{LR} = \left(D_i - V_{i,i-1} G_{i-1,i-1}^{LR} V_{i-1,i}\right)^{-1}. \tag{2.22}$$

Similarly to the left, the G^{RL} family may be generated recursively from

$$G_{i,i}^{RL} = \left(D_i - V_{i,i+1} G_{i+1,i+1}^{RL} V_{i+1,i}\right)^{-1}, \tag{2.23}$$

starting with $G_{N,N}^{RL} = D_N^{-1}$. The last block $G_{N,N}^{LR}$ in (2.22), is the exact solution for $G_{N,N}$ and will be used as input to start the recursive procedure to find the Green function elements we are interested in. The diagonal elements are computed from

$$G_{i-1,i-1} = G_{i-1,i-1}^{RL} \left(I + V_{i-1,i} G_{i,i} V_{i,i-1} G_{i-1,i-1}^{RL}\right), \tag{2.24}$$

whereas the off-diagonal elements are obtained recursively from

$$G_{i,j}|_{i>j} = -G_{i,i}^{RL} V_{i,i-1} G_{i-1,j}, \quad G_{i,j}|_{i<j} = -G_{i,i}^{LR} V_{i,i+1} G_{i+1,j}. \tag{2.25}$$

Finally, we could compute all Green function elements from (2.24) and (2.25), of which we just need the following elements

$$G_{n,1}|_{n>1} = -G_{n,n}^{RL} V_{n,n-1} G_{n-1,1}, \quad G_{n,N}|_{n<N} = -G_{n,n}^{LR} V_{n,n+1} G_{n+1,N}, \tag{2.26}$$

since the spectral functions and transmission probability are defined as

$$A_L(x_n; E) = G_{n,1} \Gamma_L G_{n,1}^{\dagger} \tag{2.27}$$

$$A_R(x_n; E) = G_{n,N} \Gamma_R G_{n,N}^{\dagger} \tag{2.28}$$

$$T(E) = \mathrm{Tr}\left[\Gamma_L G_{n,N} \Gamma_R G_{n,N}^{\dagger}\right]. \tag{2.29}$$

2.3 Band-to-band tunneling in indirect semiconductors

An indirect-band-gap semiconductor is a material in which the valence band maximum and the conduction band minimum have a difference of momentum $\mathbf{k}_0$. Then, the BTBT or Zener tunneling in an indirect semiconductor can be assisted by phonon scattering in contrast with conventional transport, where the phonon scattering is merely a dissipative mechanisms for the current. In this section we briefly present the formalism provided by Vandenberghe *et–al* in Refs. [9, 10], where the BTBT current is calculated due to the phonon-assisted tunneling in indirect semiconductors.

In second quantization, the one-electron Hamiltonian is written as

$$H_{\mathrm{el}} = \sum_{l} E_{\mathrm{v}l}\hat{b}_l^{\dagger}\hat{b}_l + E_{\mathrm{c}l}\hat{c}_l^{\dagger}\hat{c}_l \tag{2.30}$$

where $E_{\mathrm{v(c)}l}$ is the eigenvalue of electrons in the valence (conduction) band whereas $\hat{b}_l(\hat{c}_l)$ annihilates an electron in the valence (conduction) band. l is the subband index containing all relevant quantum numbers due to confinement. In case of free phonons, the corresponding Hamiltonian in second quantization is given by

$$H_{\mathrm{ph}} = \sum_{\mathbf{q}} \hbar\omega_{\mathbf{q}}\hat{a}_{\mathbf{q}}^{\dagger}\hat{a}_{\mathbf{q}} \tag{2.31}$$

where $\hat{a}_{\mathbf{q}}$ annihilates a phonon of mode $\mathbf{q}$ with energy $\hbar\omega_{\mathbf{q}}$. Then, considering only the interaction between electrons and short-wavelength phonons, we can build a bridge between the top of the valence band and the bottom of the conduction band by defining the following interaction Hamiltonian

$$H' = \sum_{ll'\mathbf{q}} g_{\mathrm{v}l\mathrm{c}l'\mathbf{q}}\hat{b}_l^{\dagger}\hat{c}_{l'}\left(\hat{a}_{\mathbf{q}} + \hat{a}_{-\mathbf{q}}^{\dagger}\right) + \mathrm{h.c.} \tag{2.32}$$

with the coupling strengths $g_{\mathrm{v}l\mathrm{c}l'\mathbf{q}}$ incorporating all possible inter-band transitions. Taking $H_0 = H_{\mathrm{ph}} + H_{\mathrm{el}}$ as the non-interacting Hamiltonian, we could express the time dependent density matrix in the interacting picture to calculate its corresponding time evolution from

$$i\hbar\frac{\mathrm{d}}{\mathrm{d}t}\tilde{\varrho}(t) = \left[\tilde{H}'(t), \tilde{\varrho}(t)\right] \tag{2.33}$$

where $\tilde{A}(t)$ denotes a time dependent operator in the interaction picture. Keeping only terms of first order in $\tilde{H}'(t)$ in the integration of (2.33), we can write the

density matrix as

$$\tilde{\varrho}(t) = \hat{\varrho}_0 - \frac{i}{\hbar}\int_0^t \mathrm{d}\tau \big[\tilde{H}'(\tau), \hat{\varrho}_0\big]. \tag{2.34}$$

Replacing the latter into

$$I_{\mathrm{v(c)}} = -e \lim_{t\to\infty} \frac{\mathrm{d}}{\mathrm{d}t} \mathrm{Tr}\Big(\hat{N}_{\mathrm{v(c)}}\tilde{\varrho}(t)\Big), \tag{2.35}$$

where $\hat{N}_{\mathrm{v(c)}}$ is the electron number operator of the valence (conduction) band, we may find an expression for the steady-state current carried by the electron-phonon interaction. First, we have to carry out the integral in (2.35) that has the form

$$I_{\mathrm{v(c)}} = -\frac{e}{\hbar^2} \lim_{t\to\infty} \int_0^t \mathrm{d}\tau \mathrm{Tr}\Big(\big[\big[\hat{N}_{\mathrm{v(c)}}, \tilde{H}'(t)\big], \tilde{H}'(\tau)\big]\hat{\varrho}_0\Big), \tag{2.36}$$

and due to particle conservation, $I_{\mathrm{v}} + I_{\mathrm{c}} = 0$ must hold. Bearing in mind that the initial equilibrium density matrix describes an uncoupled system, the commutators in (2.36) can be evaluated straightforwardly finding that the steady-current is given as

$$\begin{aligned} I_{\mathrm{v}} = -\frac{2\pi e}{\hbar} \sum_{ll'\mathbf{q}} \big|g_{\mathrm{v}lcl'\mathbf{q}}\big|^2 \\ \times \Big(& f_{\mathrm{v}}(E_{\mathrm{v}l'})(1 - f_{\mathrm{c}}(E_{cl}))(1 + \nu(\hbar\omega_{\mathbf{q}}))\delta(E_{\mathrm{v}l} - E_{cl'} - \hbar\omega_{\mathbf{q}}) \\ & - f_{\mathrm{c}}(E_{cl'})(1 - f_{\mathrm{v}}(E_{\mathrm{v}l}))\nu(\hbar\omega_{\mathbf{q}})\delta(E_{\mathrm{v}l} - E_{cl'} - \hbar\omega_{\mathbf{q}}) \\ & + f_{\mathrm{v}}(E_{\mathrm{v}l})(1 - f_{\mathrm{c}}(E_{cl'}))\nu(\hbar\omega_{\mathbf{q}})\delta(E_{\mathrm{v}l} - E_{cl'} + \hbar\omega_{\mathbf{q}}) \\ & - f_{\mathrm{c}}(E_{cl'})(1 - f_{\mathrm{v}}(E_{\mathrm{v}l}))(1 + \nu(\hbar\omega_{\mathbf{q}}))\delta(E_{\mathrm{v}l} - E_{cl'} + \hbar\omega_{\mathbf{q}}) \Big) \end{aligned} \tag{2.37}$$

where $f_{\mathrm{v(c)}}(E)$ is the Fermi-Dirac distribution for the valence (conduction) band and $\nu(E)$ denotes the Bose-Einstein distribution. Defining the probability of exciting an electron from the valence band to the conduction band with emission or absorption of a phonon as

$$T_{\mathrm{v}}^{\mathrm{abs,em}}(E, \mathbf{q}) = (2\pi)^2 \sum_{ll'} \big|g_{\mathrm{v}lcl'\mathbf{q}}\big|^2 \delta(E - E_{\mathrm{v}l})\, \delta(E - E_{cl'} \pm \hbar\omega_{\mathbf{q}}), \tag{2.38}$$

the expression for the current in (2.37) can be rewritten as follows

$$I_{\rm v} = -\frac{e}{\hbar}\int \frac{{\rm d}E}{2\pi}\sum_{\mathbf{q}}\Big(\big(f_{\rm v}(E)(1-f_{\rm c}(E-\hbar\omega_{\mathbf{q}}))(1+\nu(\hbar\omega_{\mathbf{q}}))\\ - f_{\rm c}(E-\hbar\omega_{\mathbf{q}})(1-f_{\rm v}(E))\nu(\hbar\omega_{\mathbf{q}})\big)T_{\rm v}^{\rm em}(E,\mathbf{q})\\ + \big(f_{\rm v}(E)(1-f_{\rm c}(E+\hbar\omega_{\mathbf{q}}))\nu(\hbar\omega_{\mathbf{q}})\\ - f_{\rm c}(E+\hbar\omega_{\mathbf{q}})(1-f_{\rm v}(E))(1+\nu(\hbar\omega_{\mathbf{q}}))\big)T_{\rm v}^{\rm abs}(E,\mathbf{q})\Big). \tag{2.39}$$

For the numerical evaluation of the current, the scattering matrix elements are taken from the deformation potential interaction as

$$g_{{\rm v}lcl'\mathbf{q}} = M_{\mathbf{q}}\int {\rm d}^3\mathbf{r}\,\chi_{{\rm v}l}^*(\mathbf{r})\exp\big({\rm i}(\mathbf{q}+\mathbf{k}_0)\big)\,\chi_{cl'}(\mathbf{r}),\quad M_{\mathbf{q}} = D|\mathbf{q}|\sqrt{\frac{\hbar}{2\rho_{\rm s}\omega_{\mathbf{q}}\Omega}} \tag{2.40}$$

where $\chi_{{\rm v},cl}$ is the corresponding envelope function for the eigenvalue $E_{{\rm v},cl}$ that is obtained from the solution of the Schrödinger equation, while $M_{\mathbf{q}}$ is the bulk coupling strength and the parameters $\rho_{\rm s}$, D and Ω represent the semiconductor mass density, the deformation potential and the total volume, respectively. Then, using the definition of the one-electron spectral function $A_{\rm v,c}(\mathbf{r},\mathbf{r}';E) = 2\pi\sum_l \chi_{{\rm v},cl}^*(\mathbf{r})\,\delta(E-E_{{\rm v},cl})\chi_{{\rm v},cl}(\mathbf{r}')$, the tunneling probability can be re-expressed in terms of only diagonal elements of the spectral function

$$T_{\rm v}^{\rm abs,em}(E) = \Omega\big|M_{\mathbf{q}}\big|^2\int {\rm d}^3\,\mathbf{r}A_{\rm v}(\mathbf{r},\mathbf{r};E)A_{\rm c}(\mathbf{r},\mathbf{r};E\pm\hbar\omega_{\mathbf{k}_0}), \tag{2.41}$$

where we have assumed negligible dispersion for the phonon assisting the tunneling processes since the matrix elements are strongly peaked for $\mathbf{q} = -\mathbf{k}_0$. Therefore, the final expression for the phonon-assisted current is

$$I_{\rm v} = -\frac{e}{\hbar}\int \frac{{\rm d}E}{2\pi}\Big(\big(f_{\rm v}(E)(1-f_{\rm c}(E-\hbar\omega_{\mathbf{k}_0}))(1+\nu(\hbar\omega_{\mathbf{k}_0}))\\ - f_{\rm c}(E-\hbar\omega_{\mathbf{k}_0})(1-f_{\rm v}(E))\nu(\hbar\omega_{\mathbf{k}_0})\big)T_{\rm v}^{\rm em}(E)\\ + \big(f_{\rm v}(E)(1-f_{\rm c}(E+\hbar\omega_{\mathbf{k}_0}))\nu(\hbar\omega_{\mathbf{k}_0})\\ - f_{\rm c}(E+\hbar\omega_{\mathbf{k}_0})(1-f_{\rm v}(E))(1+\nu(\hbar\omega_{\mathbf{k}_0}))\big)T_{\rm v}^{\rm abs}(E)\Big). \tag{2.42}$$

For practical application in a real device, where the fields are non-uniform, the one-electron spectral functions have to be computed numerically by assuming

that the external potential is uniform in the two contact regions, i.e. source and drain, while, the Schrödinger equation is discretized in order to implement the non-equilibrium Green function method to compute the spectral functions, and the corresponding BTBT tunneling probability and phonon-assisted current. Although, the latter formalism has been only applied to planar structures [9, 10], we will adapt it for cylindrical nanowire devices such as a nanowire $p - n$ diode and a nanowire TFET, as we will see in chapters 6 and 7, respectively.

3

The modified local density approximation and the non-linear variational principle as a computational tool for the self-consistent solution of Poisson and Schrödinger equations

3.1 Introduction

Today's miniaturization of semiconductor devices and components not only has led to substantial complications on the side of processing, fabrication and reliability, but has also tremendously increased the mathematical complexity encountered when nano-scaled devices are to be modeled with acceptable accuracy. On the one hand quantum mechanics inevitably determines the behavior of moving

*The results of this chapter were published as:
Wim Magnus, H. Carrillo-Nuñez and Bart Sorée, chapter 9 in *CMOS Nanoelectronics: Innovative Devices, Architectures and Applications*, N. Collaert. Ed. Pan Stanford Publishing, September, 2012.

charges, either through the transverse quantization of subband energies in narrow conduction channels, or when the device working principle is found to rely on quantum interference effects.

On the other hand, even when electron-electron interactions are treated only up to the level of the Hartree or the random phase approximation, the potential profile becomes strongly dependent on position, especially inside the active device areas. Emerging as a solution of Poisson's equation, the potential profile generally appears both in the Schrödinger equation governing the transverse subband ladders, and the quantum-kinetic equations that account for the quantum effects observed in the transport direction, such as the Wigner-Liouville equation [15] and the Pauli-Van Hove-Van Vliet master equations [19, 20]. Consequently, the prediction of transport characteristics of modern nanodevices requires the self-consistent solution of Poisson's equation, the Schrödinger equation and the appropriate transport equations as well as the constitutive equations that provide various non-equilibrium occupation numbers. Although Poisson's equation itself can be considered a linear differential equation, given the potential profile, the self-consistent solution scheme reveals a highly non-linear dependence of the distribution functions, wave functions etc. on the local potential. Hence, the numerical iteration loops swapping back and forth between Poisson's equation and the kinetic/constitutive equations are still burdening the computational efficiency as well as the stability of the numerical results obtained.

As is well known, the calculus of variations is based on the principle of least – or, more generally – stationary action. In the framework of differential equations, the latter amounts to the observation that the exact solution to a differential equation minimizes a properly constructed action functional. For instance, being commonly known in the field of electromagnetism [21, 22], the action functional and the corresponding Lagrangian underlying the Maxwell equations, has been successfully applied to generate approximate analytical expressions for the electromagnetic potentials by minimizing explicitly the action w.r.t. a number of tunable, free parameters. However, the use of the variational principle in the context of transport modeling is much less a common practice. In the recent past [23] the action functional related to Poisson's equation and the classical constitutive equations is minimized analytically to study a class of semiconductor devices in quasi-equilibrium. In this chapter, we will show that the variational principle can be exploited as a numerical tool to self-consistently solve the Poisson and Schrödinger equations within the framework of the modified local density approximation (MLDA), introduced earlier by Paasch and Übensee in Ref. [11], to deal with abrupt changes in the potential such as the barrier potential at the semiconductor-insulator interface found in devices. Foundations of both LDA and MLDA are given in the following sections below.

3.2 The local density approximation

The local density approximation (LDA) is the simplest approximation for the calculation of the density of a many-electron system. The method has been applied successfully either to the degenerate case [24] or to the non-degenerate case in semiconductors [25, 26], and can be summarized as follows.

Usually, conducting electrons in semiconductors are described by their one-electron eigenvalues ϵ_i and wave functions $\Phi_i(\mathbf{r})$ obtained by solving Schrödinger equation within the effective mass approximation

$$H\,\Phi_i(\mathbf{r}) = \epsilon_i\,\Phi_i(\mathbf{r}); \qquad H = -\frac{\hbar^2}{2m_{\rm c}}\nabla^2_{\mathbf{r}} + U(\mathbf{r}), \tag{3.1}$$

with the effective potential $U(\mathbf{r})$ and the effective conduction mass $m_{\rm c}$. The density can be determined by

$$n(\mathbf{r}) = 2\sum_i |\Phi_i(\mathbf{r})|^2\, F(\epsilon_i), \tag{3.2}$$

where $F(E) = (1+\exp(\beta(E-E_{\rm F}))^{-1}$ represents the Fermi-Dirac distribution function. Here, we respectively denote by $E_{\rm F}$ and T the Fermi energy and the ambient temperature, whereas $\beta = 1/k_{\rm B}T$ and spin degeneracy is included by the factor 2. This is a problem where Schrödinger and Poisson equations must be solved self-consistently, since $U(\mathbf{r})$ generally depends on the density $n(\mathbf{r})$. According to the density-functional formalism [24, 27], the effective potential $U(\mathbf{r})$ is given by

$$U(\mathbf{r}) = U_0(\mathbf{r}) + U_{\rm e}(\mathbf{r}) + U_{\rm xc}(\mathbf{r}), \tag{3.3}$$

where $U_0(\mathbf{r})$ is an external potential specified by the system, mainly due to fields or doping in an ideal semiconductor. $U_{\rm e}(\mathbf{r})$ is the Hartree potential obtained from the solution of the Poisson equation

$$\nabla^2\big[\epsilon(\mathbf{r})U_{\rm e}(\mathbf{r})\big] = -e^2\,n(\mathbf{r}), \tag{3.4}$$

with a dielectric constant $\epsilon(\mathbf{r})$ varying spatially. The last term in (3.3) is the exchange and correlation potential due to the many-body effects. The simplest approximation for it is the exchange potential

$$U_{\rm xc}(\mathbf{r}) = -\frac{3\alpha e^2}{4\pi\epsilon_0}\left(\frac{3n(\mathbf{r})}{8\pi}\right)^{\frac{1}{3}}. \tag{3.5}$$

The parameter α ranges [27, 28] from 2/3 to 1. In materials like semiconductors, where the the electron density is relatively low, electrons have room to move

away from each other and a Hartree or Hartree-Fock treatment is a sufficient approximation. However, in case of larger densities, like in metals, the interelectronic distance decreases, and the exchange correlation potential must be taken into account [29–32].

In order to invoke the LDA, we have to calculate the density of a homogeneous system with a constant potential. Then the potential is replaced by a spatially varying one. Consequently, the density becomes a local functional of the potential, as can be observed in the following examples.

3.2.1 LDA for an electron-gas: the Thomas-Fermi model

Using the LDA for a degenerate system at $T = 0$, we can find the Thomas-Fermi equation as follows. We should start from the homogeneous electron gas with density

$$\bar{n} = \frac{k_{\mathrm{F}}^3}{3\pi^2} \tag{3.6}$$

where the Fermi wave number k_{F}, the density $\bar{n}$ and Fermi energy E_{F} are connected by

$$E_{\mathrm{F}} - \bar{U} = \frac{\hbar^2 k_{\mathrm{F}}^2}{2m} \tag{3.7}$$

with a constant potential denoted by $\bar{U}$. Combining (3.6) and (3.7), then replacing the constant potential by a spatially varying one, i.e. $\bar{U} \to U(\mathbf{r})$, we find the density within the framework of LDA

$$n(\mathbf{r}) = \frac{1}{3\pi^2}\left[\frac{2m}{\hbar^2}\big(E_{\mathrm{F}} - U(\mathbf{r})\big)\right]^{3/2} \tag{3.8}$$

as function of the local value $U(\mathbf{r})$. Finally, from (3.3), (3.4) and (3.8), the Thomas-Fermi equation [24] is obtained

$$\nabla^2\big[\epsilon(\mathbf{r})U_{\mathrm{e}}(\mathbf{r})\big] = -\frac{e^2}{3\pi^2}\left[\frac{2m}{\hbar^2}\big(E_{\mathrm{F}} - U_0(\mathbf{r}) - U_{\mathrm{e}}(\mathbf{r})\big)\right]^{3/2}. \tag{3.9}$$

For the latter, U_{xc} has been neglected. Also, starting from (3.8), we can derive the Thomas-Fermi approximation for screening in the electron gas [25]. Writing the potential $U(\mathbf{r}) = \bar{U} + \delta U(\mathbf{r})$, the density within the LDA can be linearized as

$$n(\mathbf{r}) = \bar{n} + \left.\frac{\partial n}{\partial U}\right|_{\bar{U}} \delta U(\mathbf{r}), \tag{3.10}$$

which in connection with the Poisson equation, the latter leads to the Thomas-Fermi screening.

3.2.2 LDA for semiconductors at $T \neq 0$

In case of bulk semiconductor devices, within the EMA, the electron density is given by

$$n = N_{\mathrm{c}} \frac{2}{\sqrt{\pi}} \mathrm{F}_{1/2} \left(\frac{E_{\mathrm{F}} - E_{\mathrm{c}}}{k_{\mathrm{B}} T} \right). \tag{3.11}$$

In the latter expression, which is only valid for non-degenerate electron systems at equilibrium, E_{c} is the conduction band edge and E_{F} is the Fermi energy, while N_{c} is the effective conduction density. The function $\mathrm{F}_{1/2}(x)$ is the well-known 1/2 Fermi-Dirac integral

$$\mathrm{F}_{1/2}(x) = \int_0^\infty \mathrm{d}t \frac{t^{1/2}}{1 + \mathrm{e}^{t-x}}. \tag{3.12}$$

The presence of external perturbations results in a potential felt by the electrons. If we assume that the potential varies smoothly w.r.t $\mathbf{r}$, i.e. $\nabla V(\mathbf{r}) \approx 0$ on the scale of the Fermi wavelength, the constant value of the band edge may be replaced by a spatially varying one, $E_{\mathrm{c}} \to V(\mathbf{r})$, in (3.11) leading to a varying spatially electron density, $n = n(\mathbf{r})$ within the LDA. As we will see later, analogous expressions can be found for the hole density in the valence band.

In practice, as we already mentioned, the LDA requires that the potentials vary smoothly w.r.t $\mathbf{r}$. This is a disadvantage for device modeling where the potentials vary strongly, for instance, in the silicon-oxide interface in MOSFETs. In such structures, LDA is no longer valid although it is still used for the smoother parts of the potentials near the interfaces [33]. In order to include the abrupt varying potentials, we will work within the MLDA, which we extended in order to take into account quantum effects in nanodevices. The latter will be shown in the following chapters. Let us present the foundation of the MLDA and the useful applications to an infinite barrier and the well-known triangular potential.

3.3 The foundation of modified LDA

In order to present a systematic foundation of the MLDA, we start from the one-electron spectral function defined by

$$\begin{aligned} A(\mathbf{r}, \mathbf{r}'; E) &= 2\pi \left\langle \mathbf{r} \,|\, \delta(E - H) \,|\, \mathbf{r}' \right\rangle = 2\pi\, \delta(E - H)\, \delta(\mathbf{r} - \mathbf{r}') \\ &= \int_{-\infty}^{\infty} \mathrm{d}s\, \mathrm{e}^{\frac{i}{\hbar}(E-H)s} \delta(\mathbf{r} - \mathbf{r}') \end{aligned} \tag{3.13}$$

From the latter, the local density of states (LDOS) can be computed by taking $\mathbf{r} = \mathbf{r}'$. For the approximate evaluation of the spectral function in (3.13), we may

consider the total potential as a contribution of two parts, $V(\mathbf{r}) = V_1(\mathbf{r}) + V_2(\mathbf{r})$. The first part, $V_1(\mathbf{r})$, takes into account the abrupt changes in the potential, whereas the second part, $V_2(\mathbf{r})$ varies smoothly with $\mathbf{r}$. Accordingly, the Hamiltonian can be split, $H = H_1 + H_2$, with

$$H_1 = \hat{T}_1 - eV_1(\mathbf{r}) \tag{3.14}$$

$$H_2 = \hat{T}_2 - eV_2(\mathbf{r}). \tag{3.15}$$

The choice of both, H_1 and H_2 and their corresponding kinetic energy operators $\hat{T}_{1,2}$, depends on the particular problem being considered. Since $V_2(\mathbf{r})$ is assumed a weak function of $\mathbf{r}$, the commutator between H_1 and H_2 can be neglected, i.e. $[H_1, H_2] \approx 0$. Similarly, $[\hat{T}_2, V_2(\mathbf{r})] \approx 0$. The latter implies that the spectral function takes the approximate form

$$A(\mathbf{r}, \mathbf{r}'; E) = \int_{-\infty}^{+\infty} \mathrm{d}s \exp\left(\frac{\mathrm{i}}{\hbar} eV_2(\mathbf{r})s\right) \exp\left(\frac{\mathrm{i}}{\hbar}(E - H_1)s\right) \times \exp\left(-\frac{\mathrm{i}}{\hbar}\hat{T}_2 s\right) \delta(\mathbf{r} - \mathbf{r}'), \tag{3.16}$$

within the framework of MLDA. In case of no abrupt changes in the potential, $V_1(\mathbf{r}) = 0$. Therefore $V_2(\mathbf{r}) = V(\mathbf{r})$, and the density within the simple LDA given in (3.8) can be straightforwardly recovered by integrating the LDOS obtained from (3.16). The latter is the derivation of the LDA from the general framework of the MLDA.

Summarizing, the MLDA adopts the LDA as a classical description of the spectral function in those regions where the potentials vary relatively smoothly, and provides a quantum mechanical treatment to steep potentials by solving the Schrödinger equation with boundary conditions for the wave functions corresponding, for instance, to an interface modeled by an infinite barrier. This can be observed in the following example introduced by Paasch and Übensee in Ref. [11], which we have summarized below in order to acquire a better understanding of the MLDA.

3.3.1 MLDA for an infinite potential barrier

In devices such as MOSFETs or TFETs, the difference between the band edges of the silicon and the oxide at the interface is several eV. For such situations, the barrier at the silicon-oxide interface, say $z = 0$, is often modeled as an infinite barrier potential

$$V(\mathbf{r}) = \begin{cases} V(\mathbf{r}) & \text{for } z > 0 \\ \infty & \text{otherwise} \end{cases}. \tag{3.17}$$

Then, the LDA as described previously gives wrong results since the condition for its applicability is no longer valid, i.e. a slowly varying potential. In order to modify the simple LDA to treat the potential in (3.17), we have to take into account the boundary condition for the wave functions obtained from the Schrödinger equation, $\Phi_i(\mathbf{r})|_{z\leq 0} = 0$. For this purpose, we choose H_1 and H_2 as:

$$H_1 = -\frac{\hbar^2}{2m}\frac{\partial^2}{\partial z^2} - eV_\infty\theta(-z) \tag{3.18}$$

$$H_2 = -\frac{\hbar^2}{2m}\left(\frac{\partial^2}{\partial x^2} + \frac{\partial^2}{\partial y^2}\right) - eV(\mathbf{r}). \tag{3.19}$$

Solving the Schrödinger equation for H_1, we find that the appropriate wave functions in $z-$ direction are of the form $\chi_{k_z}(z) = \sqrt{2\pi^{-1}}\sin k_z z$. Then, replacing $\delta(\mathbf{r}-\mathbf{r}')$ by its completeness relation, we find that the spectral function is

$$A(\mathbf{r},\mathbf{r}';E) = 4\pi\int_{-\infty}^{+\infty}\frac{\mathrm{d}^3k}{(2\pi)^3}\sin k_z z\sin k_z z' \times \mathrm{e}^{\mathrm{i}k_x(x-x')+\mathrm{i}k_y(y-y')}\delta\left(E - \frac{\hbar^2k^2}{2m} + eV(\mathbf{r})\right), \tag{3.20}$$

where $k = \sqrt{k_x^2+k_y^2+k_z^2}$ is the length of the wave vector. Changing to spherical coordinates in phase space, the integral for LDOS can be carried out analytically

$$A(\mathbf{r};E) = \begin{cases} \frac{m}{\pi^2\hbar^2}k\big(E,V(\mathbf{r})\big)\left[1-\mathrm{j}_0\left(2zk\big(E,V(\mathbf{r})\big)\right)\right] & \text{for } z\geq 0, E > V(\mathbf{r}) \\ 0 & \text{for } z\leq 0, E < V(\mathbf{r}) \end{cases} \tag{3.21}$$

with

$$k\big(E,V(\mathbf{r})\big) = \sqrt{\frac{2m}{\hbar^2}\big(E+eV(\mathbf{r})\big)}, \qquad \mathrm{j}_0(x) = \frac{\sin x}{x}. \tag{3.22}$$

Notice that the term containing the spherical Bessel function $\mathrm{j}_0(x)$, i.e. $1-\mathrm{j}_0\left(2zk\big(E,V(\mathbf{r})\big)\right)$, is a correction to the usual LDA. Due to this correction the LDOS oscillates near the barrier and becomes zero at the interface as expected for the potential (3.17). Both characteristics are consequences of quantum effects such as the interference of the incoming and reflected waves.

Once the LDOS is known analytically (or numerically) the density can be

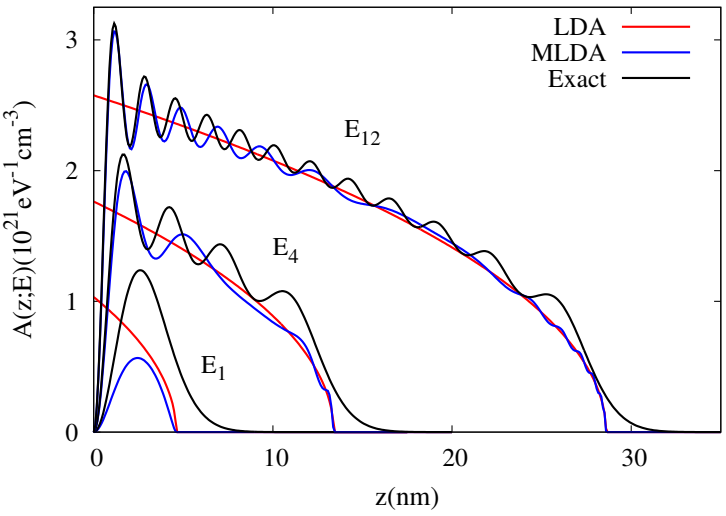

Figure 3.1: Local density of states for three energies corresponding to $E_1 = 0.023$ eV, $E_4 = 0.067$ eV and $E_{12} = 0.143$ eV eigenvalue of the triangular potential.

computed from

$$\begin{aligned} n(\mathbf{r}) &= 2\int \mathrm{d}E A(\mathbf{r};E)F(E,E_\mathrm{F}) \\ &= \frac{m}{\pi^2\hbar^2}\int_{-eV(\mathbf{r})}^{\infty} \mathrm{d}E\, k\big(E,V(\mathbf{r})\big)\left[1-\mathrm{j}_0\left(2zk\big(E,V(\mathbf{r})\big)\right)\right]\, F(E,E_\mathrm{F}). \end{aligned} \tag{3.23}$$

Then, introducing the new variables

$$\zeta = \frac{E+eV(\mathbf{r})}{k_\mathrm{B}T}; \quad \kappa = \frac{E_\mathrm{F}+eV(\mathbf{r})}{k_\mathrm{B}T}, \tag{3.24}$$

the density can be written in a more familiar form,

$$n(\mathbf{r}) = N_\mathrm{c}\frac{2}{\sqrt{\pi}}\int_0^\infty \frac{\mathrm{d}\zeta\,\zeta 1/2}{1+\mathrm{e}^{\zeta-\kappa(\mathbf{r})}}\left[1-\mathrm{j}_0\left(\frac{2z}{L}\zeta^{1/2}\right)\right] \tag{3.25}$$

where the characteristic length L and effective conduction band density N_c are defined as

$$L = \frac{\hbar}{\sqrt{2mk_\mathrm{B}T}}, \qquad N_\mathrm{c} = \frac{m}{\pi^2\hbar^2}\left(\frac{2m}{\hbar^2}\right)(k_\mathrm{B}T)^{3/2}\frac{\sqrt{\pi}}{2}. \tag{3.26}$$

As we can see, the first term in (3.25) is the usual LDA for semiconductors, whereas the second term is the correction represented by the spherical Bessel

function j_0. This is the final result for the electron density which takes into account the infinite barrier potential at $z = 0$.

In general, the electron density cannot be always derived analytically as we have shown above. Therefore, a numerical implementation of the MLDA would be necessary. First, we have to compute the LDOS for the potential $V_1(\mathbf{r})$ and the corresponding wave function and eigenvalues for the Hamiltonian H_1. Then, in the result the energy potential $-eV_2(\mathbf{r})$ is added to the eigenvalues of H_1 making, in the most general case, the eigenvalues of H_1 spatially varying as obtained, for instance, in case of cylindrical MOSFETs in chapter 4. This is a simple way to implement the MLDA for the numerical evaluation of the charge density and transport properties in more complex systems as we will see in the next chapters.

3.3.1.1 Triangular model potential within MLDA

The most simple manner to model a real inversion layer, in a semiconductor near an insulator interface, is through a triangular potential,

$$V(\mathbf{r}) = \begin{cases} Fz & \text{for } z > 0 \\ \infty & \text{otherwise,} \end{cases} \tag{3.27}$$

F is the electric field at the interface. For the triangular potential, the Schrödinger equation can be solved analytically and its solutions are Airy functions. Then it is possible to compare the MLDA and LDA with the exact results given in terms of these Airy functions. In a real inversion layer both the electric field F and the Fermi energy are not independent. However, for the sake of simplicity, in this example they are considered as independent parameters.

In Fig. 3.1, we compare the LDOS $A(z; E)$ obtained by using LDA, MLDA and the exact result, for the first, fourth and twelfth eigenvalue of the triangular potential. The value of the electric field is $F = 5 \times 10^6 V/m$, which in case of a silicon-oxide interface corresponds to a moderate inversion [34]. It can be observed that the MLDA is in good agreement with the exact result at the interface as well as the oscillations near the interface, whereas the behavior of the LDOS within LDA in this region is completely wrong. As the distance increases the MLDA approaches the usual LDA, although, oscillations can still be observed. At the classical turning point z_n, where $E_n = -eV(z_n)$, both curves become zero. Therefore, quantum effects in the region $E_n < -eV(z)$, such as tunneling and oscillations near the turning point, are not contained in both approximations. However, the agreement between the MLDA and the exact result is better for higher energies and for extremely high energies the LDA becomes again as good an approximation as the classical result.

The electron concentration for two combinations of F and E_{F} values are plotted in Fig. 3.2. Figure 3.2(a) corresponds to the case of a weak inversion layer,

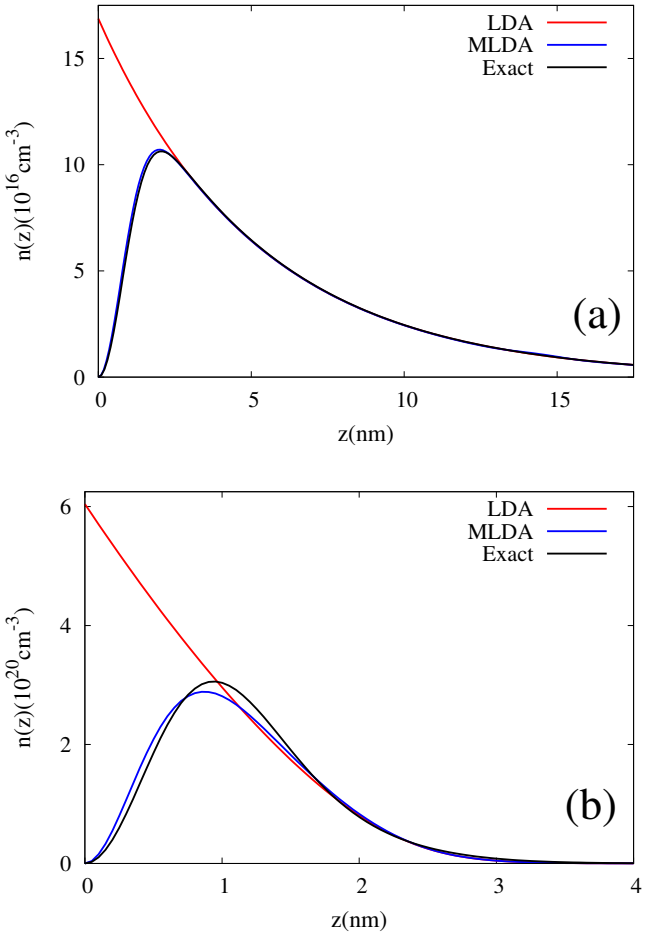

Figure 3.2: Electron concentration for the triangular potential: (a) $F = 5 \times 10^6$ V/m, $E_{\mathrm{F}} = -5k_{\mathrm{B}}T$, (b) $F = 10^8$ V/m, $E_{\mathrm{F}} = 10k_{\mathrm{B}}T$.

i.e. low F and low E_{F}, while the electron concentration of a strong inversion is shown in figure 3.2(b) with high E_{F}, i.e $E_{\mathrm{F}} = 10k_{\mathrm{B}}T$ which corresponds to a degenerate electron gas. The results suggest that the MLDA is a better approximation in comparison with LDA due to the significant improvement observed in Fig. 3.2. In the first case, i.e. non-degenerate case, the MLDA agrees with the exact result, whereas the LDA fails near the interface, as well as, in the second case, i.e. degenerate case, where again the MLDA is much more accurate.

In conclusion, the MLDA is a better approximation than the usual LDA, since it can better describe the behavior of the electron concentration at the interfaces. Therefore, the MLDA can be seen as a suitable approximation for studying nano-FETs, where non-isotropic effective masses and valley orientation must be in-

cluded. Nevertheless, the MLDA begins to fail when the separation of electron subbands becomes too large due to, for instance, extremely high electric field or strong confinement. When connecting with the Poisson equation we obtain the electron concentration and the electrostatic potential as a self-consistent solution. The latter can be achieved by exploiting a non-linear variational principle, since, from (3.25), we may see that the total charge density becomes a local functional of the potential as explained in detail in the following section.

3.4 The variational principle

In general, an arbitrary electromagnetic field is characterized by a scalar potential $V(\mathbf{r},t)$ and a vector potential $\mathbf{A}(\mathbf{r},t)$ from which the electric field and the magnetic induction may be respectively derived at any space time point $(\mathbf{r},t)$ according to

$$\mathbf{E}(\mathbf{r},t) = -\nabla V(\mathbf{r},t) - \frac{\partial \mathbf{A}(\mathbf{r},t)}{\partial t}, \quad \mathbf{B}(\mathbf{r},t) = \nabla \times \mathbf{A}(\mathbf{r},t) \tag{3.28}$$

From elementary electromagnetism [21, 22], the Lagrangian of the electromagnetic field interacting with a given charge density $\rho(\mathbf{r},t)$ and a current density $\mathbf{J}(\mathbf{r},t)$ is known to be

$$\mathcal{L} = \frac{1}{2}\left(\epsilon|\nabla V|^2 - \frac{1}{\mu}|\nabla \times \mathbf{A}|^2\right) + \mathbf{J}\cdot\mathbf{A} - \rho V \tag{3.29}$$

where $\epsilon(\mu)$ denotes the electric permittivity (magnetic permeability) of the environment. The appropriate action S appears to be a functional of the electromagnetic potentials V and $\mathbf{A}$, obtained as a composed time and volume integral:

$$S[V,\mathbf{A}] = \int_{t_0}^{t_1} \mathrm{d}t \int_{\Omega} \mathrm{d}^3 r\, \mathcal{L}[V(\mathbf{r},t), \mathbf{A}(\mathbf{r},t), \mathbf{r}, t]. \tag{3.30}$$

Here, t_0 and t_1 delimit the time interval during which the electromagnetic field flow is to be examined while Ω is a closed volume in 3D configuration space. For general purposes, one may take Ω to encompass the entire 3D Euclidean space and assert that all potentials become vanishingly small at $\partial\Omega$, the boundary surface of Ω under the assumption that ρ and $\mathbf{J}$ are strictly localized in 3D space. In the context of device modeling however, Ω is usually restricted to the device volume, in which case the lacking information on the potential values outside Ω calls for a proper set of boundary conditions specifying V and $\mathbf{A}$ (and/or their derivatives) on $\partial\Omega$. Making S stationary. i.e. imposing $\delta S = 0$ w.r.t. arbitrary

variations δV and $\delta \mathbf{A}$ that vanish at the integration limits is equivalent to solving the Euler-Lagrange equations leading to the four Maxwell equations

$$\begin{aligned} \nabla \cdot \mathbf{E} &= \frac{\rho}{\epsilon}, \quad \nabla \cdot \mathbf{B} = 0, \\ \nabla \times \mathbf{E} &= \frac{\partial \mathbf{B}}{\partial t}, \quad \nabla \times \mathbf{B} = \mu\left(\mathbf{J} + \epsilon \frac{\partial \mathbf{E}}{\partial t}\right). \end{aligned} \tag{3.31}$$

Since the aim of this chapter merely involves the effect of static (irrotational) electric fields on the charge distribution in singly connected device regions, from hereof we ignore the vector potential and the associated magnetic field to focus exclusively on Poisson's equation

$$\nabla^2 V = -\frac{\rho}{\epsilon} \tag{3.32}$$

where ϵ refers to the static permittivity of either the semiconductor (ϵ_s) or the oxide layer (ϵ_{ox}) characterizing the devices under investigation. Correspondingly, the time integral in the action functional can be removed and the effective action reduces to

$$S[V] = \int_\Omega \mathrm{d}^3 r \left(\frac{1}{2}\epsilon |\nabla V|^2 - \rho V\right). \tag{3.33}$$

If the charge density is externally specified on a mesh $\mathbf{r}_1, \ldots, \mathbf{r}_n$ as $\rho_i \equiv \rho(\mathbf{r}_i)$, $1 \leq i \leq n$, the numerical solution to Poisson's equation may be obtained by discretizing $\nabla V(\mathbf{r})$ in (3.33) and solving

$$\frac{\partial S}{\partial V_i} = 0, \quad 1 \leq i \leq n \tag{3.34}$$

while treating the array $\rho_1, \ldots, \rho_n$ as a set of independent parameters.

3.4.1 Non-linear variational principle for self-consistent solutions

As we have mentioned in the introduction, the potential and charge profiles in a realistic semiconductor device are self-consistently intertwined because, apart from fixed charges arising from ionized donors and acceptors, the concentration of mobile electrons and holes depends on the potential in a complicated way. Therefore, we first modify the action functional (3.33) to include charge density functionals that exhibit a highly non-linear dependence on $V(\mathbf{r})$. As an explicit restriction, we further neglect any non-local behavior of $\rho[V]$, i.e. we assume that the value of ρ at any point $\mathbf{r}$ is determined solely by $V(\mathbf{r})$. This way, we

may generalize the original functional (3.33) in which $\rho(\mathbf{r})$ is a fixed profile, in the following expression:

$$S[V] = \int_\Omega \mathrm{d}^3 r \left(\frac{1}{2}\epsilon |\nabla V|^2 - \int_{V_0}^{V(\mathbf{r})} \mathrm{d}V' \rho[V'] \right) \tag{3.35}$$

and V_0 is an arbitrary reference potential that does not contribute to the variations of S w.r.t. $V(\mathbf{r})$. First, we prove that the function $V(\mathbf{r})$ that makes S stationary is a solution to the nonlinear Poisson equation

$$\epsilon \, \nabla^2 V(\mathbf{r}) = -\rho[\mathbf{r}, V(\mathbf{r})], \tag{3.36}$$

where the local, but nonlinear dependence of ρ on $V(\mathbf{r})$ is in accordance with the constitutive equations that are invoked in the model under study. To this end, we calculate the variation of S caused by an arbitrary variation $\delta V(\mathbf{r})$ of the potential profile, which vanishes at the boundary surface $\partial\Omega$. Secondly, we show that the extremum of S is a genuine minimum and not a saddle point, as will also be reflected in the stability of the numerical minimization algorithm that is built on these findings. The variation of S can be extracted straightforwardly from

$$\delta S = \int_\Omega \mathrm{d}^3 r \left[\frac{1}{2}\epsilon \left(\left| \nabla \big(V(\mathbf{r}) + \delta V(\mathbf{r}) \big) \right|^2 - |\nabla V(\mathbf{r})|^2 \right) - \int_{V(\mathbf{r})}^{V(\mathbf{r})+\delta V(\mathbf{r})} \mathrm{d}V' \rho[V'] \right].$$

Using Gauss's theorem

$$\int_\Omega \mathrm{d}^3 r \, \nabla \cdot \big(\delta V(\mathbf{r}) \nabla V(\mathbf{r}) \big) = \int_{\partial\Omega} \mathrm{d}\mathbf{a} \cdot \nabla V(\mathbf{r}) \delta V(\mathbf{r}) \tag{3.37}$$

with $\mathrm{d}\mathbf{a}$ denoting the vector normal to the surface of an infinitesimal area element. In the latter, the right-hand side equals zero as $\delta V(\mathbf{r})$ vanishes when $\mathbf{r} \in \partial\Omega$. Inserting therefore

$$\int_\Omega \mathrm{d}^3 r \, \nabla \delta V(\mathbf{r}) \cdot \nabla V(\mathbf{r}) = -\int_{\partial\Omega} \mathrm{d}^3 r \, \delta V(\mathbf{r}) \nabla^2 V(\mathbf{r}) \tag{3.38}$$

into (3.37) and expanding $\rho(V')$ in a second-order Taylor series around $V' = V(\mathbf{r})$, we find

$$\delta S = \int_\Omega \mathrm{d}^3 r \left[-\delta V(\mathbf{r}) \left(\epsilon \, |\nabla V(\mathbf{r})|^2 + \rho[V(\mathbf{r})] \right) + \frac{1}{2} \left(\epsilon \, |\nabla \delta V(\mathbf{r})|^2 - \left. \frac{\partial \rho[V']}{\partial V'} \right|_{V'=V(\mathbf{r})} \big(\delta V(\mathbf{r}) \big)^2 . \right) \right] \tag{3.39}$$

Ignoring first the second-order contributions, we observe that putting $\delta S = 0$ for all $\delta V(\mathbf{r})$ that vanish on $\partial\Omega$ requires that $V(\mathbf{r})$ solve (3.36), as expected. Next, substituting the formally exact solution into (3.39), we conclude that

$$\frac{\partial \rho[V]}{\partial V} < 0, \quad \forall V \tag{3.40}$$

is a sufficient condition for the second-order variation to become positive definite, thus ensuring that the extremal value of the action functional is indeed a minimum.

Next we need to find out in which relevant cases we can concretely use the criterion formulated in (3.40), bearing in mind that the charge density inside a semiconductor device generally builds up from mobile electrons and holes as well as fixed dopant charges:

$$\rho(\mathbf{r}) = e\big[p(\mathbf{r}) - n(\mathbf{r}) + N_{\mathrm{D}}(\mathbf{r}) - N_{\mathrm{A}}(\mathbf{r})\big], \tag{3.41}$$

where $e = +1.602\times10^{-19}$ C represents the absolute value of the electron charge. $p(\mathbf{r})$ and $n(\mathbf{r})$ respectively denote the concentrations of the mobile holes and electrons, whereas N_{D} and N_{A} refer to the contributions arising from the ionized donors and acceptors. Considering the latter as fixed charges, not depending on the potential profile, quasi-equilibrium of a non-degenerate semiconductor [23] may be characterized by the classical Boltzmann relations

$$n(\mathbf{r}) = n_i \exp\left(\frac{\mu_n + eV(\mathbf{r})}{k_{\mathrm{B}}T}\right), \quad p(\mathbf{r}) = p_i \exp\left(-\frac{\mu_p + eV(\mathbf{r}) - E_{\mathrm{g}}}{k_{\mathrm{B}}T}\right), \tag{3.42}$$

where n_i is the intrinsic carrier concentration and μ_n and μ_p respectively denote the electron and hole quasi-chemical potentials. Clearly, $\rho(\mathbf{r})$ not only appears to be a local functional of $V(\mathbf{r})$ but also seems to satisfy condition (3.40) as can be seen from

$$\frac{\partial \rho[V]}{\partial V} = -\frac{e\,n_i}{k_{\mathrm{B}}T}\left[\exp\left(\frac{\mu_n + eV(\mathbf{r})}{k_{\mathrm{B}}T}\right) + \exp\left(-\frac{\mu_p + eV(\mathbf{r}) - E_{\mathrm{g}}}{k_{\mathrm{B}}T}\right)\right] < 0. \tag{3.43}$$

Moreover, the integral over V' in (3.35) can be done analytically, leading to

$$S = \int_\Omega \mathrm{d}^3 r \left[\frac{1}{2}\epsilon\big|\nabla V(\mathbf{r})\big|^2 - e\left(N_{\mathrm{D}}^+(\mathbf{r}) - N_{\mathrm{A}}^-(\mathbf{r})\right)V(\mathbf{r}) + n_i k_{\mathrm{B}}T\times \right.$$
$$\left.\left(\exp\left(\frac{\mu_p}{k_{\mathrm{B}}T}\right)\left(\exp\left(-\frac{\mu_n + eV(\mathbf{r})}{k_{\mathrm{B}}T}\right) + \exp\left(-\frac{\mu_p + eV(\mathbf{r}) - E_{\mathrm{g}}}{k_{\mathrm{B}}T}\right)\right)\right)\right] \tag{3.44}$$

which is directly applicable to numerical processing. However, as explained in the following section, it is also possible to extend the variational approach to semiclassical transport that accounts for quantum confinement effects.

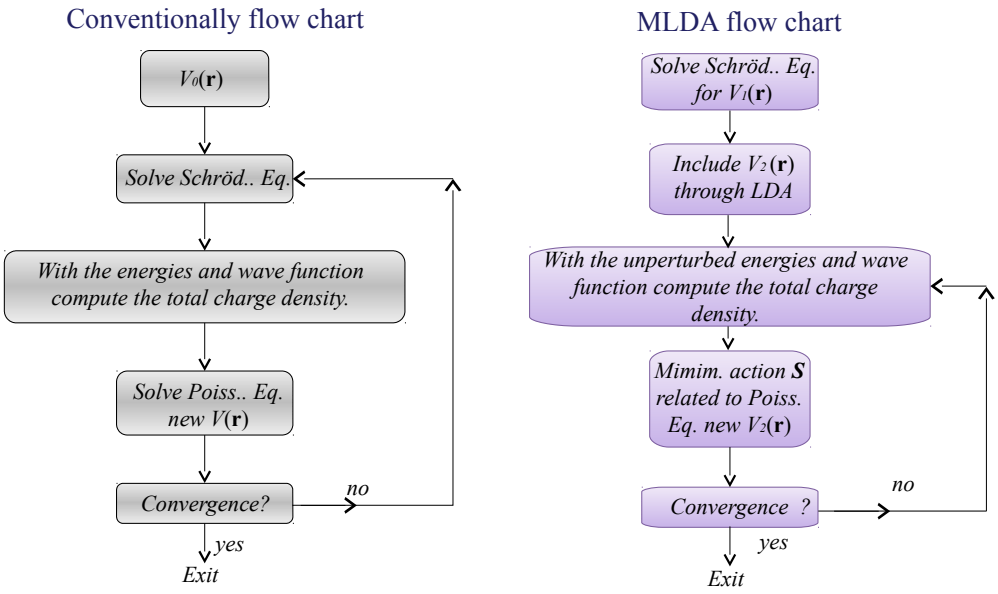

Figure 3.3: Computational algorithm for the self-consistent solution of the Poisson and Schrödinger equations, showing the conventionally flow chart (left) and the MLDA flow chart (right).

3.4.2 Numerical algorithm for the self-consistent solution

Conventionally, the self-consistent solution of the Schrödinger and Poisson equations are obtained iteratively by initially guessing the potential profile. In turn, the eigenvalues and wave functions obtained from the Schrödinger solver and based on this potential profile yield the total charge density. Then, from the solution of Poisson's equation, a new potential profile is obtained and consecutive iteration cycles are carried out until convergence is reached , as summarized on the left flow chart in Fig. 3.3. In general, the procedure followed to obtain a fully self-consistent solution of the Poisson and Schrödinger equations is computationally expensive because of the CPU time taken by the subsequent iterations to reach convergence. As explained above, we can invoke a non-linear variational scheme to avoid the necessity of going back and forth between Poisson and Schrödinger equations as observed on the MLDA flow chart in Fig. 3.3. This can be done since the charge density is a local functional of the potential as a remarkable consequence of the MLDA, giving rise to a non-linear Poisson equation of the form (3.36). Moreover, the minimization of the action (3.35) with respect to the potential leads to a simultaneous solution of the Poisson and Schrödinger equations, as well as the transport equation, for instance, the Boltzmann equation in case of non-equilibrium.

For the purpose of practical evaluation of the action, we define a grid of N nodes of the potential V_i covering the entire device where i contains the indexes of the 2D or 3D grid with $i = 1, ..., N$. Then, we may find

$$S^{(i)}[V_i] = S_E^{(i)}[V_i] + S_{\mathrm{c}}^{(i)}[V_i] + S_{\mathrm{v}}^{(i)}[V_i] + S_{\mathrm{doping}}^{(i)}[V_i] \tag{3.45}$$

as a function of V_i, where

$$S_E^{(i)}[V_i] = \sum_{\langle i,j \rangle} \frac{1}{2} C_{ij} \big(V_j - V_i\big)^2 \tag{3.46}$$

is the zero-th order contribution arising from the first term in (3.35) whereas the coefficients C_{ij}, which depend on the material properties and the geometry of the system, can be considered as capacitances. Also, $\langle j, i \rangle$ means that the summation is carried out on the $j - th$ first-neighbor nodes greater than the $i - th$ node. The other four terms are related to the contributions from the fixed doping concentration

$$S_{\mathrm{doping}}^{(i)}[V_i] = -eV_i(N_{\mathrm{D}} - N_{\mathrm{A}})\Omega_i, \tag{3.47}$$

and the contributions from the electron (c) and hole (v) densities

$$S_{\mathrm{v(c)}}^{(i)}[V_i] = \mp e \int_{\mathbf{r}_i}^{\mathbf{r}_{i+1}} \mathrm{d}^3 r \int_{V_0}^{V_i} \mathrm{d}V' n_{\mathrm{v(c)}}[\mathbf{r}, V'], \tag{3.48}$$

where $\int_{\mathbf{r}_i}^{\mathbf{r}_{i+1}} \mathrm{d}^3 r = \Omega_i$ is the volume of the cell corresponding to the $i - th$ node. Next, the total action is computed as the summation over all contributions $S^{(j)}$, i.e.

$$S = \sum_j S^{(j)}. \tag{3.49}$$

Then, it can be shown by direct evaluation that the equations

$$\frac{\partial S}{\partial V_i} = \sum_j \frac{\partial S^{(j)}}{\partial V_i} = 0, \tag{3.50}$$

which induce the minimization of S, coincide with the discretized non-linear Poisson equation representing the simultaneous solution of Poisson and Schrödinger equation as well as encompassing the non-equilibrium distribution function. Solving the linear parts of these equations for V_i,

$$V_i = G(V_1^{\mathrm{old}}, ..., V_{i-1}^{\mathrm{old}}, V_{i+1}^{\mathrm{old}}, ..., V_N^{\mathrm{old}}), \tag{3.51}$$

where G is a function of the previous values of the potential, by adopting a Gauss-Seidel iteration scheme, we can implement the following computational algorithm, which is summarized on the MLDA flow chart in Fig. 3.3, to minimize the action yielding the full self-consistent solution at once:

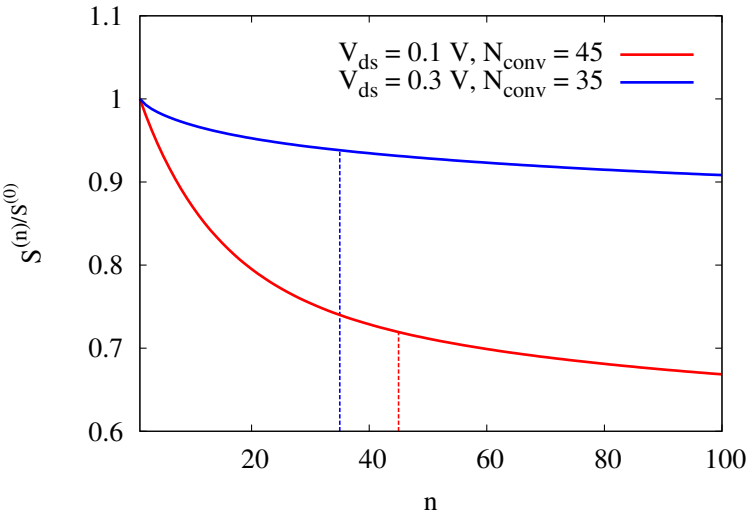

Figure 3.4: Normalized action versus number of iterations for $V_{\rm ds}$ = 0.1 V and $V_{\rm ds}$ = 0.3 V. N_{conv} is the number of iterations required to reach relative convergence for a given tolerance of $\eta = 10^{-3}$.

1. Solve Schrödinger equation for the potential $V_1(\mathbf{r})$.
2. Find the total charge as a local functional of the potential $V_2(\mathbf{r})$ within the framework of the MLDA.
3. Insert an educated guess for the potential profile $V_2(\mathbf{r}_i) = V_i$ into the right-hand side of (3.51) and obtain a new profile from the left-hand side.
4. Iterate step 2 and verify whether the updated action S is lower than the previous one.
5. Terminate the iterations after the n-th iteration when the relative convergence criterion

$$\max |V_i^{(n)} - V_i^{(n-1)}| < \eta \times |V_i^{(n-1)}| \tag{3.52}$$

and the absolute convergence criterion

$$S^{(n)} < S^{(n-1)} < \cdots < S^{(2)} < S^{(1)} \tag{3.53}$$

are simultaneously met for a prescribed tolerance $\eta > 0$.

Finally, in Fig. 3.4. the normalized action is plotted against the number of iterations for a case of interest such as the cylindrical nanowire MOSFET studied in

chapter 5. In order to trace the evolution of the action over subsequent iteration cycles, we have extended the number of iterations far beyond the relative convergence criterion. As a result, both curves of Fig. 3.4. reveal the relatively slow pace of the absolute convergence sequence which monitors the evolution of the action towards its exact minimum. However, the exact minimal action being considerably lower than the value obtained when relative convergence is achieved, should not be a matter of concern. After all, the numerical calculation of the genuine minimum would generally call for quite a large numerical accuracy, say on the level of machine precision, which would substantially exceed moderate tolerances such as 10^{-3} or larger. In other words, the absolute convergence should be rather viewed as an indicator guarding the stability of the numerical solution that could be expected if a new simulation with a smaller tolerance were to be made.

3.5 Conclusion

Summarizing, we have briefly described a modified LDA introduced by Paasch and Übensee in Ref. [11] and a non-linear variational principle to achieve simultaneously the self-consistent solution of Poisson and Schrödinger equations. Since the solution of the non-linear Poisson equation (3.36) is obtained by only minimizing numerically the action (3.36), it is expected that the algorithm presented not only offers a trade-off between quantum mechanical rigor and computational speed, but also accelerates the evaluation of quantum mechanical charge and current density profiles of devices for which the MLDA is a reasonable approximation. Therefore, instead of implementing a full self-consistent procedure for Poisson and Schrödinger equations, we will invoke the non-linear MLDA-based variational method, we have presented above in this chapter, for studying cylindrical nanowire FETs: cylindrical MOSFETs and TFETs. Details are given in chapter 4 and 5, respectively.

4

A simplified quantum mechanical model for nanowire transistors

4.1 Introduction

During the last decades, continuous scaling down of device dimensions has resulted in novel generations of nano-sized electronic devices and nano-structures. Promising candidates are the upcoming post-CMOS (Complementary Metal-Oxide-Semiconductor) devices. Due to the small size of these devices quantum effects become crucial to understand their working principles and research efforts have been launched in order to acquire qualitative and quantitative knowledge for predicting the behavior of these new structures.

Nevertheless, the inclusion of quantum effects into the models used to simulate carrier transport remains a challenge even today. Amongst the formalisms and the related kinetic equations coping with this task, we encounter: the Boltzmann transport equation (BTE) [15, 35], the Wigner transport equation (WTE) [15,36–38], the Pauli master equation [39,40] and the method of non-equilibrium Green's functions (NEGF) [17, 38, 41]. On one hand these techniques have demonstrated a great efficiency and satisfactory results but on the other hand,

*The results of this chapter were published as:
H. Carrillo-Nuñez, Wim Magnus, and F. M. Peeters, J. App. Phys., **108**, 063708 (2010). Also selected for the September 27, 2010 issue of Virtual Journal of Nanoscale Science & Technology.

the numerical simulations require heavy computational efforts as they also involve the self-consistent solution of the Schrödinger and Poisson equations.

In this chapter, we have studied an ultra-thin cylindrical MOSFET depicted in Fig. 4.1. The structure consists of a semiconductor nanowire which is covered by an oxide layer whereas a gate contact overlays the p-doped channel region, the latter being sandwiched between heavily n-doped source and drain regions. This device has been the subject of various theoretical [41, 42] studies and is considered a promising candidate to replace the conventional planar MOSFET [43]. The purpose of this work is to introduce a quantum mechanical transport model consisting of a simplified Poisson-Schrödinger solver and a module to compute the current density, all within the framework of the MLDA [11] which we have extended to the 1D ballistic BTE in order to calculate self-consistently the carrier distribution and the potential profile felt by the carriers as well as the current flowing through the conduction channel inside the nanowire. Unlike the previously mentioned formalisms, we have implemented the non-linear MLDA-based variational principle in order to avoid the full self-consistent solution of the Schrödinger and Poisson equations. For that purpose, we have defined an action functional the minimization of which with respect to the potential yields the self-consistent solution at once as mentioned in the previous chapter. In order to present our approach, we have introduced the simplified Poisson-Schrödinger solver and discussed its numerical implementation in detail. Then, an expression for the current density is derived using a distribution function obtained from the analytical solution of the 1D ballistic BTE for the steady state. The latter relies on the method of characteristic curve as is briefly explained in the appendix A. Finally, a few simulation results are shown and discussed.

4.2 Simplified quantum mechanical transport model

4.2.1 Self-consistent Poisson-Schrödinger solver

A self-consistent solution of the Schrödinger and Poisson equations involves the computation of the hole and electron concentrations as well as the potential profile $U(\mathbf{r})$ obeying Poisson's equation. Considering the wire a perfect cylinder and adopting the effective-mass approximation, we may conveniently express the one-electron Hamiltonian in terms of cylindrical coordinates (r, ϕ, z) as

$$\hat{H} = -\frac{\hbar^2}{2m_{\alpha\perp}}\left(\frac{\partial^2}{\partial r^2} + \frac{1}{r}\frac{\partial}{\partial r} + \frac{1}{r^2}\frac{\partial^2}{\partial \phi^2}\right) - \frac{\hbar^2}{2m_{\alpha z}}\frac{\partial^2}{\partial z^2} + U(r, z). \tag{4.1}$$

α is a conduction band valley index whereas $m_{\alpha\perp}$ and $m_{\alpha z}$ respectively denote the effective mass in the planar cross section of the wire and the longitudinal

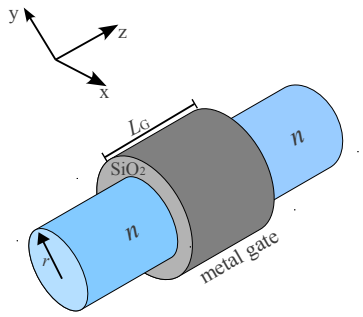

Figure 4.1: Schematic 3D picture of the cylindrical MOSFET

effective mass in the transport direction. The potential energy profile $U(r,z)$ generally consists of the electrostatic potential energy $U_e(r,z)$ and the abrupt energy barrier $U_B(r,z) = U_{\rm B}\,\Theta(r > R)$ at the semiconductor/oxide interface $r = R$. Taking the barrier height $U_{\rm B}$ infinitely high for the sake of simplicity, we assume that all electrons are confined to the interior of the nanowire. $U_e(r,z)$ is related to the electrostatic potential through $U_e(r,z) = -eV(r,z)$ which is obtained by solving Poisson's equation

$$\nabla^2 V(r,z) = -\frac{1}{\epsilon_0 \epsilon_i}\rho(r,z), \quad i = 1,2, \tag{4.2}$$

where ϵ_1 and ϵ_2 are the dielectric constants of the semiconductor and the oxide layer, respectively. The total charge density $\rho(r,z)$ results from the mobile holes and electrons as well as the ionized dopants, as will be discussed below.

In the simple case of an homogeneous, unbiased wire without junctions, electrons do not feel any potential inside the wire and can move freely in the z-direction, i.e. $U_1(r,z) = 0$, while being subjected to the boundary condition that their wave functions vanish at the interface $r = R$, i.e. $U_1(R,z) = \infty$. In that case the eigensolutions $\psi_{\alpha ml}(k;r,\phi,z)$ and the corresponding energy eigenvalues $E_{\alpha ml}(k)$ of (4.1) can be expressed analytically as follows:

$$\begin{aligned} E_{\alpha ml}(k) &= \frac{\hbar^2 k^2}{2m_{\alpha z}} + \frac{\hbar^2 x_{ml}^2}{2m_{\alpha\perp}R^2}, \quad m = 0, \pm1, \pm2, \ldots; \quad l = 1,2,\ldots \\ \psi_{\alpha ml}(k;r,\phi,z) &= \frac{J_m\left(\dfrac{x_{ml}r}{R}\right)\mathrm{e}^{\mathrm{i}m\phi}\mathrm{e}^{\mathrm{i}kz}}{\sqrt{\pi R^2 L}\,|J_{m+1}(x_{ml})|}, \end{aligned} \tag{4.3}$$

where L is the wire length and x_{ml} is the $l-$th zero of the m-th Bessel function $J_m(x)$. In (4.3), the wave numbers are defined relative to the vector $\mathbf{k}_{\mathbf{0}\alpha}$

connecting the Γ point with the minimum of the α-th conduction band. Hence, the phase factor $\exp(\mathrm{i}k_{0\alpha z}z)$ that determines the dependence of the wave functions on the valley index α trivially reduces to 1. Correspondingly, within the Hartree approximation, the electron concentration of the electron gas in thermal equilibrium reads

$$n(r,\phi,z) = n(r,z) = 2\frac{L}{2\pi}\sum_{\alpha}\sum_{m,l}\int_{-\infty}^{\infty}\mathrm{d}k\,|\psi_{\alpha ml}(k;r,\phi,z)|^2\,F(E_{\alpha ml}(k),E_{\mathrm{F}}) \tag{4.4}$$

$$= \sum_{m=0}^{\infty}\sum_{l=1}^{\infty}C_{ml}J_m^2\Big(\frac{x_{ml}r}{R}\Big)\sum_{\alpha}\int_{-\infty}^{\infty}\mathrm{d}k\,F(E_{\alpha ml}(k),E_{\mathrm{F}}), \tag{4.5}$$

where $F(E,E_{\mathrm{F}}) = [1+\exp\big(\beta(E-E_{\mathrm{F}})\big)]^{-1}$ is the Fermi-Dirac distribution function, E_{F} the Fermi energy, $\beta = 1/k_{\mathrm{B}}T$ and the coefficients C_{ml} are given by

$$C_{ml} = \frac{2-\delta_{m0}}{\pi^2R^2J_{m+1}^2(x_{ml})}. \tag{4.6}$$

The prefactor 2 appearing in (4.4) accounts for spin degeneracy while angular momentum degeneracy is covered by the factor $2-\delta_{m0}$ in (4.6).
However, in case of a gated wire consisting of an n^+–p^-–n^+ structure and being biased by both a gate voltage V_{G} and a drain voltage V_{ds}, a non-uniform potential energy profile $U_2(r,z) = U_e(r,z)$ emerges inside the nanowire whereas the Fermi-Dirac function needs to be replaced by an appropriate non-equilibrium distribution function. The extraction of the latter from the 1D ballistic BTE as well as its extension to the 3D structure of the nanowire are detailed in Appendix A. Adopting the MLDA [11] and assuming the variation of $U_e(r,z)$ in both the r- and z-directions to be sufficiently small on the scale of the Fermi wave-length, we simply add $U_e(r,z) = -eV(r,z)$ to the unperturbed one-electron eigenenergies $E_{\alpha ml}(k)$ thereby keeping the wave functions $\psi_{\alpha ml}(k;r,\phi,z)$ unaltered. As a result, the electron concentration inside the biased wire reads

$$n(r,z) = \sum_{m=0}^{\infty}\sum_{l=1}^{\infty}C_{ml}J_m^2\Big(\frac{x_{ml}r}{R}\Big)\sum_{\alpha}\int_{-\infty}^{\infty}\mathrm{d}k\,f_{\mathrm{B}}(E_{\alpha ml}(k)-eV(r,z)), \tag{4.7}$$

where $f_{\mathrm{B}}(E)$ is the ballistic electron distribution function for the steady state. As explained in appendix A, the derivation relies on the assumption that, for a given coordinate $r \leqslant R$, the potential energy attains a unique maximum $U_{\mathrm{M}}(r)$ at some point $z_{\mathrm{M}}(r)$, allowing for a "critical" value of the classical momentum

$$p_{\mathrm{M}}(r,z) = \sqrt{2m_{\alpha z}\big(U_{\mathrm{M}}(r)-U_e(r,z)\big)}. \tag{4.8}$$

Tracing the classical electron trajectories back to the infinite past, we arrive at

$$f_{\mathrm{B}}(E) = F(E, \mu(r, z, \hbar k)), \tag{4.9}$$

where the chemical potential $\mu(r, z, \hbar k)$ can conveniently be expressed in terms of the logical step function $\Theta(x)$:

$$\mu(r, z, p) = E_{\mathrm{F}} - eV_{\mathrm{ds}}\Big[\Theta\big(p \leqslant -p_{\mathrm{M}}(r, z)\big)\Theta\big(z \leqslant z_{\mathrm{M}}(r)\big) + \Theta\big(p \leqslant p_{\mathrm{M}}(r, z)\big)\Theta\big(z \geqslant z_{\mathrm{M}}(r)\big)\Big] \tag{4.10}$$

Here, we consider only $n-$channel wires where, due to the presence of a positive gate voltage V_{G} the holes will be repelled towards the central region of the wire where no abrupt barriers in the radial direction are expected to appear. Consequently, it is assumed that the hole concentration is adequately represented by the classical expression based on Boltzmann statistics,

$$p(r, z) = N_{\mathrm{V}} \mathrm{e}^{-\beta(eV(r,z)+E_{\mathrm{g}}+E_{\mathrm{F}})}, \tag{4.11}$$

involving the band gap E_{g} and the effective valence band concentration N_{V}, while the Fermi energy is determined by requiring local charge neutrality in the bulk part of the source contact. Finally, from (4.7)-(4.11) one can infer that the total charge density,

$$\rho\big[r, V(r, z)\big] = e\Big(p\big[r, V(r, z)\big] - n\big[r, V(r, z)\big] + N_{\mathrm{D}}^{+}\big[r, V(r, z)\big] - N_{\mathrm{A}}^{-}\big[r, V(r, z)\big]\Big) \tag{4.12}$$

is depending only on the *local* value of the electrostatic potential $V(r, z)$. N_{D}^{+} and N_{A}^{-} are the ionized donor(source/drain) and acceptor(channel) concentrations, respectively.

On the one hand, the local relations between the potential and carrier densities in (4.7)-(4.12) are classical, on the other hand the electron concentration in (4.7) offers a trade-off between quantum mechanical rigor and computational speed ignoring quantum effects such as reflection and tunneling in z-direction. This approach, that we have adapted to the case of a nanowire, was introduced by Paasch and Übensee [11] to study planar structures and quantum wells thereby providing a quantum mechanical treatment of all abrupt barriers, such as the semiconductor/insulator barrier, while retaining a classical description for the smoother parts of the potential inside the semiconductor.

Since the full self-consistent solution of the Poisson and Schrödinger equations is computationally expensive to reach convergence, we will implement the non-linear MLDA based variational principle. In order to do so, the classical Boltzmann electron distribution for electrons is replaced by the non-equilibrium distribution $f_{\mathrm{B}}(r,z)$, solving the ballistic Boltzmann equation and accounting for lateral size quantization within the framework of the MLDA. The explicit form of $f_{\mathrm{B}}(r,z)$ is derived in Appendix A, leading to the set of equations (A.8)-(A.9). In cylindrical coordinates, the action functional in (3.35) reads as:

$$S = \int_{\Omega} \mathrm{d}^3 r \left(\frac{1}{2}\epsilon \left[\left(\frac{\partial V(r,z)}{\partial r} \right)^2 + \left(\frac{\partial V(r,z)}{\partial z} \right)^2 \right] - \int_{V_0}^{V(r,z)} \mathrm{d}V' \rho[r,V'] \right). \tag{4.13}$$

Ω and ϵ denote the wire volume (including both the semiconductor area and oxide regions) and the dielectric constant respectively, and again V_0 denotes an arbitrary reference potential which can be safely absorbed in the offset of the action functional. As already known, the minimization of the action with respect to the potential leads to a simultaneous solution of the Poisson, Schrödinger and Boltzmann transport equations within the framework of the MLDA. Moreover, it can be shown that the extreme value corresponding to $\delta S = 0$ is an absolute minimum since the condition $\partial\rho/\partial V < 0$ is obeyed within the present case for all possibles values of the dummy potential V, as may be seen by calculating explicitly the derivative of $\rho[r, V(r,z)]$. In practice, the integration over V' in (4.13) can be carried out analytically while the minimization of the action functional needs to be done numerically. The latter can be used as an absolute criterion of convergence, e. g. in a Gauss-Seidel iteration scheme [44].

The action S in (4.13) essentially contains five terms, $S = S_E + S_n + S_p + S_{\mathrm{doping}}$. S_E is the contribution of the first term in the second part of (4.13). S_{doping} is the contribution arising from the fixed donor and acceptor densities

$$S_{\mathrm{doping}}[V] = -e \int_{\Omega} \mathrm{d}^3 r \left[N_{\mathrm{D}}^{+}(r,z) - N_{\mathrm{A}}^{-}(r,z) \right] V(r,z). \tag{4.14}$$

Similarly, the contribution from the holes which is taken from (4.11) can be expressed as

$$S_p[V] = 2\pi e\, k_{\mathrm{B}} T\, N_{\mathrm{V}} \exp\left(-\frac{E_{\mathrm{g}} + E_{\mathrm{F}}}{k_{\mathrm{B}} T} \right) \int_0^R \mathrm{d}r \int_0^L \mathrm{d}z \, \exp\left(-\frac{eV(r,z)}{k_{\mathrm{B}} T} \right), \tag{4.15}$$

while integrating $n[r, z, V']$ over V', we obtain the electron contribution S_n,

$$S_n[V] = \frac{1}{\beta}\sum_{m=0}^{\infty}\sum_{l=1}^{\infty} C_{ml}\int_0^R \mathrm{d}r\, r J_m^2\Big(\frac{x_{ml}r}{R}\Big)\int_0^L \mathrm{d}z \\ \times \sum_{\alpha}\int_{-\infty}^{\infty}\mathrm{d}k \ln\left[1+\mathrm{e}^{\beta\left(\mu(r,z,\hbar k)-E_{\alpha ml}(k)+eV(r,z)\right)}\right], \quad (4.16)$$

where the contribution related to the constant V_0 has been omitted.

In order to evaluate the action, we define a 2D-grid of (r_i, z_j) points with $0 \leqslant i \leqslant N_r$ and $0 \leqslant j \leqslant N_z$. Providing an educated initial guess for the potential $V(r_i, z_j)$, we extract the charge density from the set of equations (4.7) to (4.12). Substituting the latter into the discretized Poisson equation (3.51) we calculate a new potential using a Gauss-Seidel iteration scheme until the criterions of convergence (3.52) and (3.53) are reached.

It is worth to remark that the non-linear variational principle presented here avoids the necessity of solving Schrödinger's equation in each iteration cycle, while the numerical solution of Poisson's equation is directly integrated into the constitutive equations leading to the electron and hole concentrations.

4.3 Ballistic current in a Si nanowire transistor

Once the potential energy profile $U_e(r, z)$ is known, the ballistic electron current density can be obtained by averaging the group velocities $p/m_{\alpha z}$ with the distribution function given by equations (4.9) – (4.10). Bearing in mind that only electrons surmounting the barrier maximum $U_{\mathrm{M}}(r)$ or, equivalently carrying momenta $|p| > p_{\mathrm{M}}(r, z)$ can contribute to the current, we may write the current density as

$$J(r,z) = \frac{e}{2\pi\hbar}\sum_{m=0}^{\infty}\sum_{l=1}^{\infty} C_{ml}J_m^2\Big(\frac{x_{ml}r}{R}\Big) \\ \times \sum_{\alpha}\int_{p_{\mathrm{M}}(r,z)}^{\infty}\mathrm{d}p\,\frac{p}{m_{\alpha z}}\left[F\left(\frac{p^2}{2m_{\alpha z}}+U_{\alpha ml}(r,z), E_{\mathrm{F}}\right)\right. \\ \left. - F\left(\frac{p^2}{2m_{\alpha z}}+U_{\alpha ml}(r,z), E_{\mathrm{F}}-eV_{\mathrm{ds}}\right)\right], \quad (4.17)$$

where $U_{\alpha ml}(r, z) = W_{\alpha ml}+U_e(r, z)$ and $W_{\alpha ml}$ are the flat-band subband energies given by

$$W_{\alpha ml} = \frac{\hbar^2 x_{ml}^2}{2m_{\alpha\perp}R^2}. \quad (4.18)$$

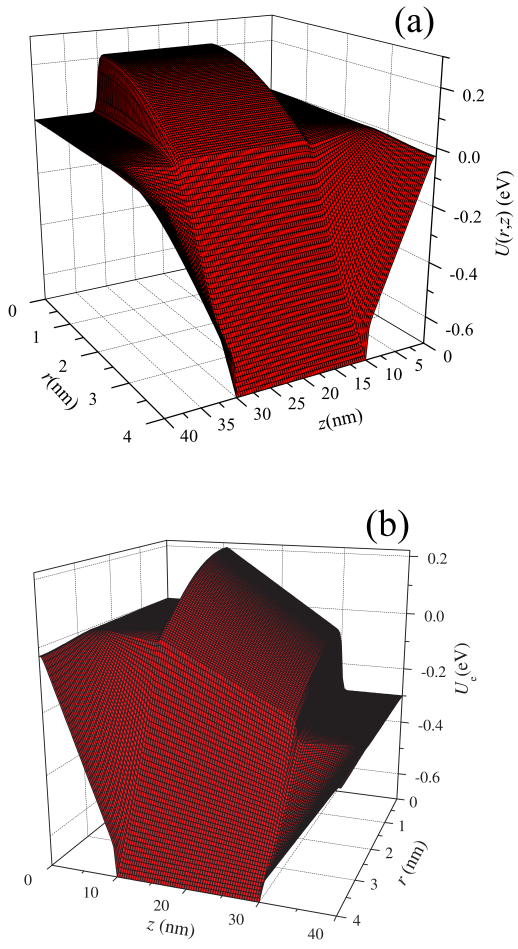

Figure 4.2: Typical electrostatic potential in the cylindrical MOSFET with $L_{\rm CH} = 20$ nm: (a) $V_{\rm ds} = 0$ V and (b) $V_{\rm ds}$ = 0.3 V..

Taking $E = p^2/(2m_{\alpha z}) + U_{\alpha ml}(r,z)$ as an integration variable, we further obtain

$$J(r,z) = \frac{e}{2\pi\hbar}\sum_{m=0}^{\infty}\sum_{l=1}^{\infty} C_{ml} J_m^2\Big(\frac{x_{ml} r}{R}\Big) \times \sum_{\alpha}\int_{U_{\rm M}(r)+W_{\alpha ml}}^{\infty} {\rm d}E\,\Big[F(E,E_{\rm F}) - F(E,E_{\rm F}-eV_{\rm ds})\Big], \quad (4.19)$$

which explicitly shows that $J(r)$ is independent of z, in accordance with the requirement that the steady-state current density be solenoidal. Performing the

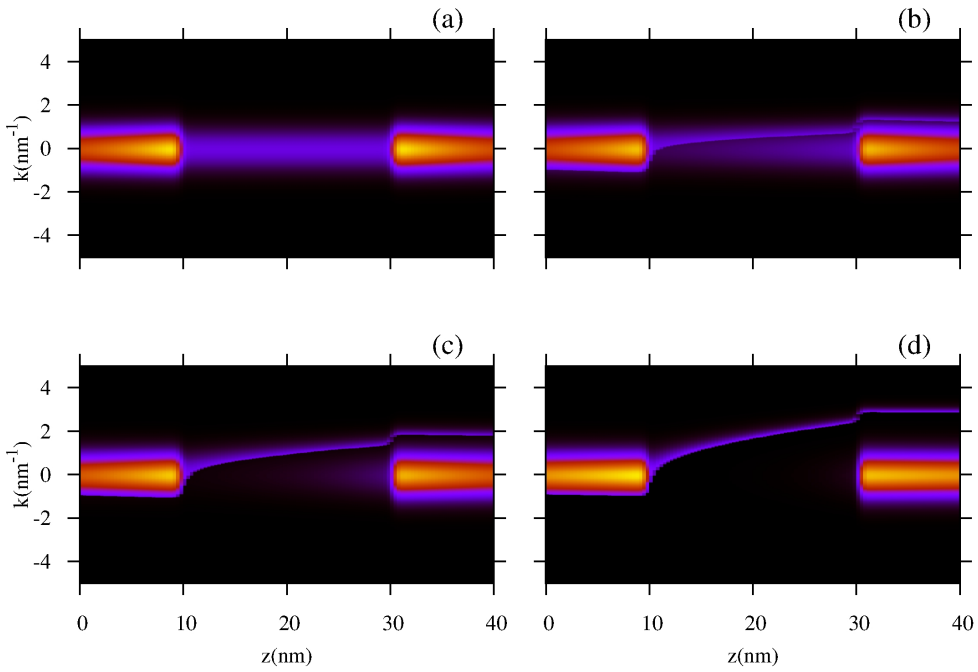

Figure 4.3: Contour plots of the Boltzmann distribution function $f_{\mathrm{B}}(z, \hbar k)$ for the lowest subband ($m = 0, l = 1$) at r =2.2 nm. (a) $V_{\mathrm{ds}} = 0.0$ V, (b) $V_{\mathrm{ds}} = 0.03$ V, (c) $V_{\mathrm{ds}} = 0.1$ V and (d) $V_{\mathrm{ds}} = 0.3$ V.

integral over E analytically, we find

$$J(r) = \frac{e}{2\pi\hbar\beta} \sum_{m=0}^{\infty} \sum_{l=1}^{\infty} C_{ml} J_m^2\left(\frac{x_{ml} r}{R}\right) \sum_{\alpha} \ln\left[\frac{1 + \mathrm{e}^{\beta(E_{\mathrm{F}} - U_{\mathrm{M}}(r) - W_{\alpha ml})}}{1 + \mathrm{e}^{\beta(E_{\mathrm{F}} - U_{\mathrm{M}}(r) - W_{\alpha ml} - eV_{\mathrm{ds}})}}\right]. \tag{4.20}$$

The total current passing through the cross-section of the nanowire can be computed by integrating $J(r)$ over the wire cross section. It can be shown that at low temperatures ($\beta \to \infty$), when only the lowest subband is occupied by electrons, and for low drain voltages ($eV_{\mathrm{ds}} \ll E_F$) the current obtained by integrating (4.20) reduces to the Landauer-Büttiker formula [17] with full transmission.

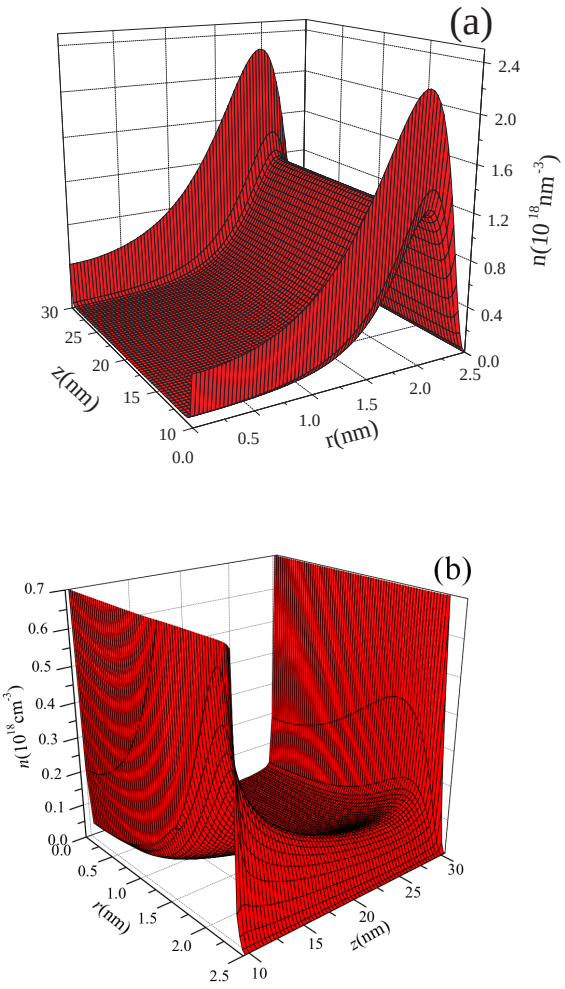

Figure 4.4: 3D electron concentration at (a) $V_{\rm ds}$ = 0.0 V and (b) $V_{\rm ds}$ = 0.3 V with $L_{\rm CH} =$ 20 nm.

4.4 Simulations

For the numerical simulation of a cylindrical MOSFET, we have taken the longitudinal and transverse electron masses, occurring in $m_{\alpha\perp}$ and $m_{\alpha z}$, to be $m_{\rm trans}$ = 0.19 m_0 and $m_{\rm long}$ = 0.98 m_0 respectively, and we have adopted the following values of the device parameters: the nanowire radius and the thickness of the SiO_2 layer are taken to be $R = 2.5$ nm and 1.5nm respectively; the dielectric constant of the silicon $\epsilon_1 = 11.7$ and oxide layer $\epsilon_2 = 3.9$; the channel length $L_{\rm CH}$ equals 20 nm, while the length of the homogeneously n^+-doped source

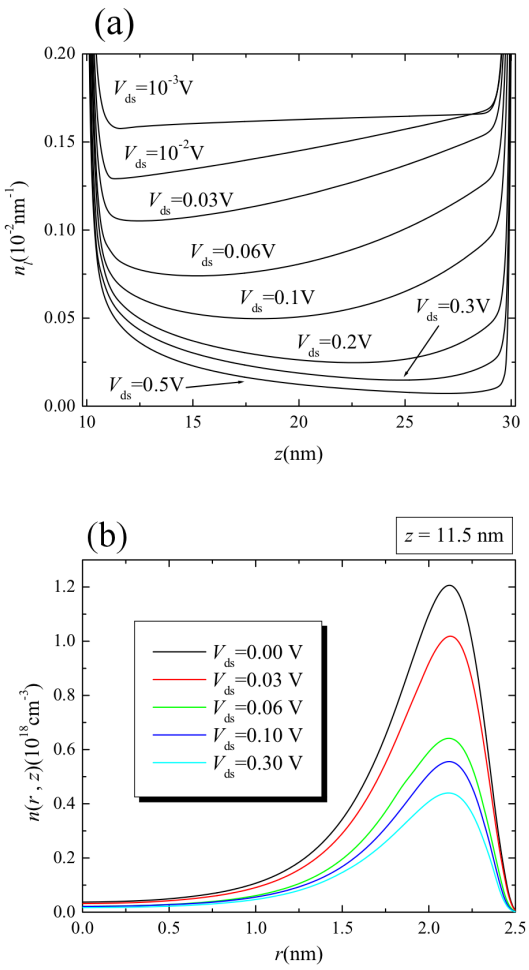

Figure 4.5: (a) Linear electron concentration and (b) electron concentration at $z = 11.5$*nm for various* $V_{\rm ds}$ *with* $L_{\rm CH} = 20$ *nm.*

and drain regions is fixed to 10 nm. The donor concentration of both regions is $N_{\rm D} = 10^{20}$ cm^{-3} whereas the p-doped channel has an acceptor concentration $N_{\rm A} = 10^{18}$ cm^{-3}. The temperature $T = 300$ K and the current-voltage characteristics shown below are calculated for the gate voltages $V_{\rm G} = 0.5$ V, 0.6 V and 0.7 V, the drain voltage $V_{\rm ds}$ ranging between 0 and 0.7 V. The action functional (4.13) that was minimized numerically with respect to $V(r, z)$ (see Fig. 3.4), has been computed as the sum of all contributions arising from $N_r \times N_z$ rectangular grid cells, with N_r = N_z = 120.

Fig. 4.2 depicts typical electrostatic potential profiles $U_e(r, z)$ for a wire with a channel length $L_{\rm CH}$ = 20 nm at drain voltages (a) $V_{\rm ds} = 0$ and (b) $V_{\rm ds} = 0.3$

V, clearly revealing the potential barriers at the p-n junctions. $U_e(r,z)$ reaches its maximum at the central axis (r = 0) in both cases, while, along the channel, the potential wells confining the inversion layer electrons in the radial direction, is located near the Si/SiO_2 interface at $r = R$. For $V_{\rm ds} = 0$ V, the potential in Fig. 4.2(a) is a symmetric barrier at $L/2$, since the system is in equilibrium, whereas at $V_{\rm ds} = 0.3$ V, in Fig. 4.2(b), we can see the effects of an applied bias leading to non-equilibrium, as observed in Fig. 4.3, where it is plotted the contour plots of the distribution function $f_{\rm B}(r,z,\hbar k)$ for the lowest subband ($m = 0, l = 1$) at $r = 2.2$ nm for different values of the applied bias $V_{\rm ds}$. As expected, the carriers injected from both source and drain regions are equally occupied the states in the channel region in case of $V_{\rm ds} = 0.0$ in Fig.4.3(a). For $V_{\rm ds} \gtrsim 0$ V, in the ballistic limit, electrons injected from the source, with $p \geq p_M(z)$, travel without scattering in the inversion layer and their velocities increase along the channel region. This effect is clearly visualized by the narrow "ballistic jet" appearing in the distribution function contour plots across the channel region, as shown in figs. 4.3((b)-(d)).

Figs. 4.4((a),(b)) are the respectively electron 3D concentrations along the channel for the potential profiles in Fig. 4.2 computed within the framework of MLDA. The electron concentrations are found to pile up pronouncedly in front of SiO_2 interface while vanishing completely at $r = R$. The linear electron concentration in the channel, $n_l(z) = \int_0^R {\rm d}r\, r\, n(r,z)$, and the electron concentration in the radial direction at some point near the channel/drain interface, i.e. $z = 11.5$ nm, are plotted in Fig. 4.5((a),(b)) for different values of the drain voltage. Note that the linear electron concentration is higher than at the channel/drain interface for low drain voltage $V_{\rm ds} \lesssim 0.1$ V, while for $V_{\rm ds} \gtrsim 0.1$ V, the opposite is true. This is because no carriers are being injected from the drain to the source region as is confirmed by the contour plots in figs. 4.3(c) and 4.3(d), for $V_{\rm ds} = 0.1$ V and $V_{\rm ds} = 0.3$ V, respectively. Note that for low voltages, electrons originating from the drain predominantly occupy the states in the channel region, while for higher voltages their concentration significantly decreases and the corresponding part of the distribution function tends to zero.

Fig. 4.6 depicts the 3D current density within the MLDA computed for $V_{\rm G} = 0.7$ V, as function of r and $V_{\rm ds}$. Note that the current density at the center of the nanowire takes considerably lower values than in the inversion layer where most of the electrons are located while, due to the confinement, the current density is bound to vanish at the Si/SiO_2 interface. In Fig. 4.7(a), the I-$V_{\rm ds}$ characteristics are plotted for different gate voltages $V_{\rm G}$ and channel length $L_{\rm CH} = 20$ nm. At low values of $V_{\rm ds}$, the current depends linearly on $V_{\rm ds}$, while a kink occurring at $V_{\rm ds} = 0.1$V initiates the saturation regime. The larger the applied gate voltage $V_{\rm G}$, the lower is the increment of the current in the saturation region and the higher are the values of the total current. Also, our simulations showed that

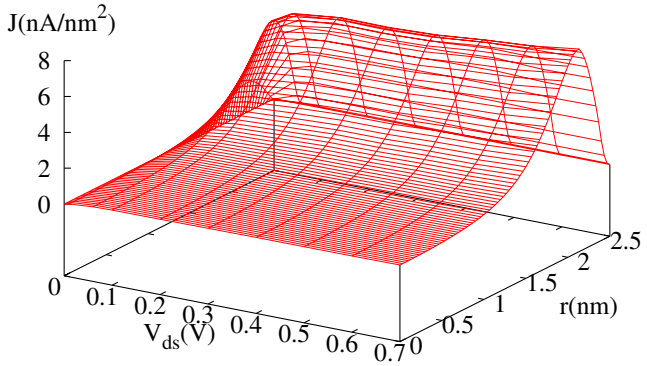

Figure 4.6: 3D current density as a function of r and $V_{\rm ds}$ at $V_{\rm G}$=0.7 V.

when the channel length increases, the slope of the I-$V_{\rm ds}$ curves in the saturation regime decreases. The first effect emerges from the enhanced gate control as the gate voltage increases. The second one reflects drain-induced barrier lowering (DIBL) of the p–n junction barrier, typically occurring for decreasing channel lengths [45]. For the sake of completeness, we have compared in Fig. 4.7(b), the I-$V_{\rm G}$ characteristics obtained by implementing our approach and similar characteristics reported previously by Wang *et-al* in Ref. [41]. As can be observed, both curves are in qualitative agreement, while the main quantitative differences can be explained by noticing that our approach presently ignores both reflection and tunneling events as well as the metal gate /semiconductor work function difference, amounting to approximately 0.25 eV.

Finally, we believe that the present method can be generalized also to tackle transport in nanostructures where tunneling through longitudinal barriers inevitably becomes a real issue. A possible extension can be launched by adopting the picture proposed by Barker and Murray [46] and introducing an appropriate class of classical potentials. Varying slightly around the real potential profile, a subset of these classical potentials have a barrier maximum below the real maximum such that electrons surmounting the corresponding maxima along classical paths are found to emulate tunneling through the real potential barrier. Combining the related Boltzmann distribution functions in a coherent superposition eventually leads to a Wigner function that correctly incorporates barrier tunneling.

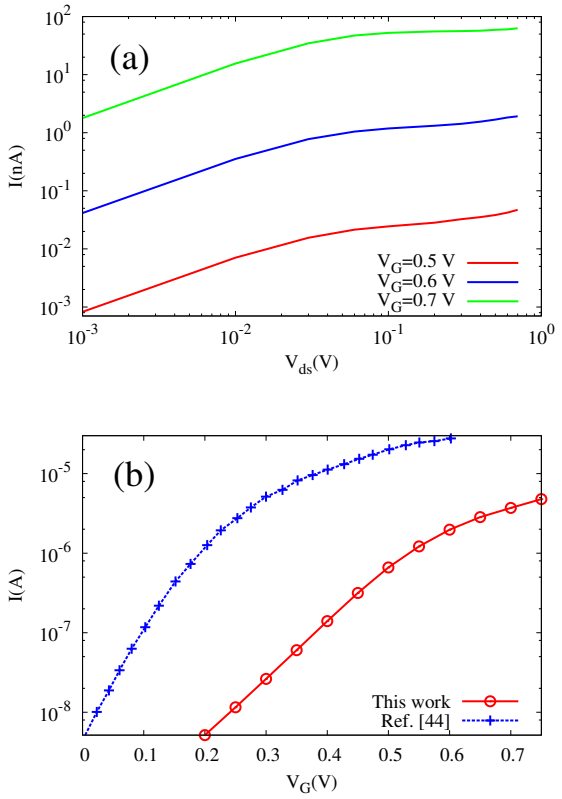

Figure 4.7: (a) $I - V_{\rm ds}$ and (b) I-$V_{\rm G}$ characteristics for a intrinsic nanowire of silicon. The device parameters and doping concentration are obtained from Ref. [41] as: R=1.5nm, $L_{\rm CH}$=10nm, 8nm for the source and drain length and $N_{\rm D} = 2 \times 10^{20} cm^{-3}$.

4.5 Conclusions

Summarizing this chapter, we have presented a simplified quantum mechanical model for the electron distribution and current density of a nanowire transistor, operated in the ballistic regime. A Poisson-Schrödinger solver was developed by exploiting the non-linear MLDA-based variational principle introduced previously in chapter 3 to evaluate the charge density profiles of cylindrical MOSFET. We expect that our approach could be applied to investigate transport in more complicated device structures and devices for which the MLDA is an acceptable approximation, such as the double-gate MOSFET [37] or a cylindrical TFET as we will see in the next chapter. To end, we have to keep in mind that the non-linear variational principle used to integrate Poisson's and Schrödinger's equations as well as the constitutive equations that provides the charge density profile,

is a generalization of the variational principle introduced earlier in Ref. [23] and exploits the numerical minimization of the corresponding action functional as an absolute convergence criterion.

5

Electron low-field conductivity in gated silicon nanowires

5.1 Introduction

Novel generations of nano-sized electronic devices and nano-structures, such as nanowire-silicon-based are expected to bring new transport characteristic due to quantum effects relevant in the nanometer scale. Using the tight-binding formalism (TB), based on the atomistic nature of the material [47], we have found that, in materials like silicon, the effective-mass-approximation may be questionable in wires with few nanometer body thickness; therefore, for electronic transport simulations nonparabolic corrections must be taken into account. Implementing an advanced method such as TB to compute the nanowire band structure, precision is gained, the simulation time may increase significantly. In order to retain the accuracy of the atomistic simulations but to avoid the time consuming, we will implement an analytical model to investigate the working principles of these devices [48–51], such as the gated thin cylindrical nanowire depicted in fig 5.1 with infinitely channel length. The most common one employed is the Kane's model [49–52]. The latter explicitly depends on a parameter containing information about the nonparabolicity of the conduction band and its simplicity has made it very useful for simulations to investigate effects of nonparabolicity in the transport properties of nanodevices, however, an appropriate value of a nonparabolic parameter α needs to be known.

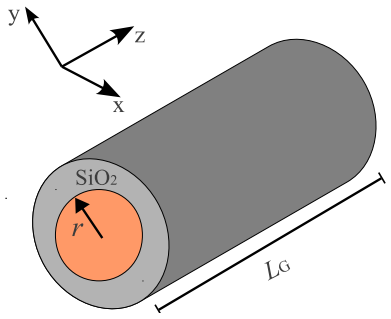

Figure 5.1: Gated thin cylindrical nanowire

An important electronic transport characteristic in device engineering that has been tackled lately [48,53] is the low-field mobility. In Ref. [53] the low-field mobility was computed only in case of phonon scattering within the effective mass approximation, whereas in Ref. [48] nonparabolic effects were included in the calculations of the low-field mobility for relatively thin nanowires introducing a formalism for surface roughness scattering in cylindrical nanowires. Recently, in Ref. [54], the phonon-limited electron mobility in rectangular silicon nanowire MOSFET has been studied within the effective mass approximation (EMA). In this paper, corner effects based on spatially resolved mobility analysis were investigated. Nevertheless, non of the latter works has incorporated an appropriate band structure based on ab-initio calculations or TB formalism. In this work, the nanowire Si band-structure was computed via TB [47] code and the nonparabolic parameter is obtained by a direct comparison with Kane's model.

As we have done it in the previous chapter, we will implement the non-linear MLDA-based variational method to solve Schrödinger and Poisson equations self- consistently only in the radial direction taking the nonparabolic correction for the eigenvalues of the energies. Once, the potential is know, we have calculated the momentum relaxation time for both, acoustic phonon and surface roughness scattering in the framework of MLDA, allowing us to obtain alternatively, the spatial low-field mobility and its corresponding low-field conductivity within MLDA of a thin cylindrical silicon gated nanowire, i.e. Si body radius less than 2.5 nm, with channel grown along the [100] direction . Also, we briefly present the main expressions for the phonon and surface roughness scattering formalism, as well as, their corresponding expressions within the MLDA. Results and conclusion are given at the end of the chapter.

5.2 Kane's model: self-consistent calculations with nonparabolic corrections

Adopting the Kane's model for electrons in a nonparabolic conduction band, we may conveniently express the Schrödinger equation as [52]

$$\left(-\frac{\hbar^2}{2m_{\lambda z}}\frac{\partial^2}{\partial z^2}+H_{\lambda;r\phi}\right)\Psi_\lambda(k;\mathbf{r},z)=\left[E+\alpha\left(E-U(\mathbf{r})\right)^2\right]\Psi_\lambda(k;\mathbf{r},z). \quad (5.1)$$

where α is referred to as the nonparabolic parameter while λ is the valley index. Ψ is the wave function of the electrons and $U(\mathbf{r})$ the potential energy. For an all-round biased gated cylindrical nanowire sufficiently long, the $z-$dependence of the total potential $U(\mathbf{r})$ can be neglected in the low driving field limit. Therefore, we could consider only a varying potential in the radial direction, i.e. $U(\mathbf{r})=U(r)$, with the one-electron Hamiltonian within the effective mass approximation expressed as

$$H_{\lambda;r\phi}=-\frac{\hbar^2}{2m_{\lambda\perp}r}\frac{\partial}{\partial r}r\frac{\partial}{\partial r}-\frac{\hbar^2}{2m_{\lambda\perp}r^2}\frac{\partial^2}{\partial\phi^2}+U(r) \quad (5.2)$$

where $m_{\lambda\perp}=(2m_{\lambda x}m_{\lambda y})/(m_{\lambda x}+m_{\lambda y})$ and $m_{\lambda z}$ are the parabolic bulk effective mass in the planar cross-section of the nanowire and the longitudinal mass in the $z-$direction, respectively. The radial potential energy, $U(r)=-eV(r)+U_{\rm B}\Theta(r-R)$, is the contribution of the electrostatic potential energy obtained from the Poisson's equation

$$\nabla^2V(r)=-\frac{e}{\epsilon_0\epsilon_i}\rho(r)\quad i=1,2, \quad (5.3)$$

whereas $U_{\rm B}$ denotes silicon/oxide barrier potential energy at $r=R$. $\Theta(x)$ is the step function. ϵ_1 and ϵ_2 are the dielectric constants of the silicon and the oxide layer, respectively.

In order to solve the set of coupled equations (5.1)-(5.3) self-consistently, we invoke the non-linear MLDA-based variational scheme. In analogy with the previous chapter, we have to compute first the electron concentration for the simple case of an homogeneous unbiased wire, in which, electrons do not feel any potential inside the silicon region of the nanowire, i.e. $U_1(r<R)=0$. However, we have assumed their corresponding wave functions vanish at the interface, $r=R$, since the potential barrier, $U_1(R)=U_{\rm B}$, is taken to be infinitely high. The eigenvalues obtained from the solution of (5.1), where $U(r)=U_1(r)$, are the Bessel function given by (4.3), whereas the nonparabolic eigenvalues for

a perfect wire are expressed as

$$E^{\mathrm{NP}}_{\lambda ml}(k) = \frac{1}{2\alpha}\left[\sqrt{1+4\alpha\left(\frac{\hbar^2 k^2}{2m_{\lambda z}}+W_{\lambda ml}\right)}-1\right]; \quad W_{\lambda ml} = \frac{\hbar^2 x^2_{ml}}{2m_{\lambda\perp}R^2} \tag{5.4}$$

where $W_{\lambda ml}$ are the parabolic subband energy eigenvalues obtained by solving the corresponding Schrödinger equation for the parabolic Hamiltonian in (5.2). Then, the electron concentration for unbiased wire can be read as

$$n(r) = \sum_{m=0}^{\infty}\sum_{l=1}^{\infty} C_{ml} J^2_m\Big(\frac{x_{ml}r}{R}\Big)\int_{-\infty}^{\infty}\mathrm{d}k\, F(E^{\mathrm{NP}}_{\lambda ml}(k), E_{\mathrm{F}}), \tag{5.5}$$

Invoking the MLDA, the variation of the potential, $U_2(r) = -eV(r)$, is assumed weak and can be added to the unperturbed nonparabolic eigenvalues $E^{\mathrm{NP}}_{\lambda ml}(k)$, however, the wave functions are kept unaltered [48, 55]. Finally, the electron concentration within the MLDA taking into account the nonparabolic correction is given by

$$n[r, V(r)] = \sum_{m=0}^{\infty}\sum_{l=1}^{\infty} C_{ml} J^2_m\Big(\frac{x_{ml}r}{R}\Big)\int_{-\infty}^{\infty}\mathrm{d}k\, F(E^{\mathrm{NP}}_{\lambda ml}(k) - eV(r), E_{\mathrm{F}}) \tag{5.6}$$

where $F(E, E_{\mathrm{F}}) = [1+\exp\big((E-E_{\mathrm{F}})/k_{\mathrm{B}}T\big)]^{-1}$ is the Fermi-Dirac distribution function, E_{F} the Fermi energy, k_{B} the Boltzmann constant. Since the electron concentration depends on $V(r)$ locally, the total charge density in (5.3) is a local functional of the potential, i.e. $\rho[r, V(r)]$. Then, we may implement the nonlinear variational principle introduce earlier in chapters 3 and 4 to solve self-consistently (5.1), (5.3) and (5.6).

5.3 Surface roughness and intravalley phonon scatterings within the MLDA

Within the Ando's model, the surface roughness at the interface of a cylindrical wire can be represented by a small fluctuation $\Delta_{\phi z}$ around the the ideal surface $r = R$. The latter is conveniently expanded in a Fourier series

$$\Delta_{\phi z} = \sum_{m,k}\tilde{\Delta}_{mk} e^{i(m\phi+kz)}, \tag{5.7}$$

where m is an integer ranging from $-\infty$ to ∞, k is the axial wave-vector along the z-direction incrementing in steps of $2\pi/L_{\mathrm{W}}$. From now on, we will assume

that the autocorrelation function of the surface roughness is described by an exponential distribution characterized by an rms value Δ and a correlation length Λ [48]:

$$\langle \Delta_{\phi z} \Delta_{00} \rangle = \Delta^2 \ \exp\left(-\frac{\sqrt{2}}{\Lambda} \sqrt{R^2\phi^2 + z^2} \right), \tag{5.8}$$

with $\langle \cdots \rangle$ representing the ensemble average. The autocorrelation function (5.8) is an empirical expression, and could be improved if we could have more information on the surface roughness experiments. Taking the Fourier transform of autocorrelation function (5.8), we can find its corresponding power spectrum density [48]:

$$\left\langle |\Delta_{mk}|^2 \right\rangle = \frac{\pi \Delta^2 \Lambda^2}{2\pi RL} \left[1 + \frac{\Lambda^2}{2} \left(\frac{m^2}{R^2} + k^2 \right) \right]^{-3/2}. \tag{5.9}$$

It is expected that the surface roughness modifies the barrier potential of the ideal nanowire and causes a perturbation identified as the scattering potential with matrix elements [48]

$$\langle \lambda' m' l' k' | U^{\text{SR}} | m l k \lambda \rangle = U^{\text{SR}}_{\lambda' m' l' k', \lambda m l k} = \tilde{\Delta}_{m'-m, k-k'} \sqrt{\Gamma_{\lambda m l} \Gamma_{\lambda' m' l'}}. \tag{5.10}$$

The Γ's coefficients are the responsible for the intra-subband scattering defined as:

$$\Gamma_{\lambda m l} = -\frac{\partial T^{(0)}_{\lambda m l}}{\partial R} + e \left\langle \frac{r}{R} \frac{\partial V(r)}{\partial r} \right\rangle^{(0)}_{\lambda m l} \tag{5.11}$$

where $\langle \cdots \rangle^{(0)}_{\lambda m l}$ denotes the expectation value related to full self-consistent unperturbed wave functions, whereas $T^{(0)}_{\lambda m l} = \langle T \rangle^{(0)}_{\lambda m l}$ is the expectation value of the kinetic energy in the confinement direction. In the latter, the first term represents the fluctuation of the kinetic energy due to the radius fluctuation, while the second depends on the average of electric field [48]. The Γ's coefficients appear in the expression for surface roughness momentum relaxation time $\tau^{\text{SR}}_{\nu}(E)$ for a given state $|mlk\rangle$

$$\frac{1}{\tau^{\text{SR}}_{\lambda m l}(E)} = \frac{\pi L}{\hbar} \Gamma_{\lambda m l} \sum_{\lambda' m' l'} \Gamma_{\lambda' m' l'} A_{\lambda' m' l'}(E) \left[\left\langle |\Delta_{m-m', q_1}|^2 \right\rangle + \left\langle |\Delta_{m-m', q_2}|^2 \right\rangle \right], \tag{5.12}$$

obtained from Fermi's Golden Rule, with $q_{1,2} = k(E) \pm k'(E)$ and k is given in term of the energy E as

$$k(E) = \sqrt{\frac{2 m_{\lambda z}}{\hbar^2} (E - W_{\lambda m l} + \alpha E^2)}. \tag{5.13}$$

In case of electron scattering with acoustic phonons, the momentum relaxation time is [53]

$$\frac{1}{\tau^{\mathrm{AC}}_{\lambda ml}(E)} = \frac{\pi \Xi^2 k_{\mathrm{B}} T}{\rho_{\mathrm{Si}} \hbar v_{\mathrm{S}}^2} \sum_{\lambda m' l'} A_{\lambda m' l'}(E) F_{\lambda ml, \lambda m' l'}, \tag{5.14}$$

where ρ_{Si} is the density of the silicon, v_{S} is the sound velocity, Ξ is the deformation potential, whereas $A_{\lambda ml}(E)$ is the one-dimensional (1D) density of states (DOS) and $F_{\lambda ml, \lambda m' l'}$ is the usual form factor

$$F_{\nu,\nu'} = \frac{1}{2\pi} \int_0^\infty dr r F^2_{\lambda ml}(r) F^2_{\lambda m' l'}(r). \tag{5.15}$$

Within the framework of the MLDA, the second term in the right hand side of (5.11) is neglected since we are assuming a slow varying potential. Then, (5.11) is mainly reduced to the fluctuation of the unperturbed kinetic energy

$$\Gamma_{\lambda ml} = (1 + 4\alpha W_{\lambda ml})^{-1/2} \frac{2}{R} W_{\lambda ml}, \tag{5.16}$$

whereas the DOS must be replaced by the nonparabolic LDOS within the scope of the MLDA, i.e. $A_{\lambda ml}(E) \to A_{\lambda ml}(r; E)$

$$A_{\lambda ml}(r; E) = \sqrt{\frac{m_{\lambda z}}{8\pi^2 \hbar^2}} \frac{1 + 2\alpha(E + eV(r))}{\sqrt{E + eV(r) - W_{\lambda ml} + \alpha(E + eV(r))^2}}. \tag{5.17}$$

Consequently, the surface roughness momentum relaxation time can be re-written as

$$\frac{1}{\tau^{\mathrm{SR}}_{\lambda ml}(r; E)} = \frac{\pi L}{\hbar} \Gamma_{\lambda ml} \sum_{\lambda m' l'} \Gamma_{\lambda m' l'} A_{\lambda m' l'}(r; E) \times \left[\left\langle \left| \Delta_{m-m', q_1(r)} \right|^2 \right\rangle + \left\langle \left| \Delta_{m-m', q_2(r)} \right|^2 \right\rangle \right], \tag{5.18}$$

where $q_{1,2}(r) = k(r; E) \pm k'(r; E)$ and the wave vector k depends on r within the MLDA as follows

$$k(r; E) = \sqrt{\frac{2m_{\lambda z}}{\hbar^2} \left(E + eV(r) - W_{\lambda ml} + \alpha(E + eV(r))^2 \right)}, \tag{5.19}$$

whereas the acoustic phonon momentum relaxation time is expressed as

$$\frac{1}{\tau^{\mathrm{AC}}_{\lambda ml}(r; E)} = \frac{\pi \Xi^2 k_{\mathrm{B}} T}{\rho_{\mathrm{Si}} \hbar v_{\mathrm{S}}^2} \sum_{\lambda m' l'} A_{\lambda m' l'}(r; E) F_{\lambda ml, \lambda m' l'}, \tag{5.20}$$

within the MLDA. In the latter, the form factor is given in terms of Bessel functions

$$F_{\lambda ml,\lambda m'l'} = \frac{2\pi}{\pi^2 R^4 J^2_{m+1}(x_{ml}) J^2_{m'+1}(x_{m'l'})} \int_0^R \mathrm{d}r\, r J^2_m \left(\frac{x_{ml} r}{R}\right) J^2_{m'} \left(\frac{x_{m'l'} r}{R}\right). \tag{5.21}$$

Note that the relaxation times are now also a function of the radial coordinate. This means that electrons will have different relaxation times at different values of r.

Once the the momentum relaxation time is known, the low-field mobility within the MLDA can be obtained from the Kubo-Greenwood formula for 1D transport [48]

$$\mu(r) = \frac{2e}{\pi n_{1\mathrm{D}} \hbar} \sum_{\lambda ml} \int_{E^{\mathrm{NP}}_{\lambda ml}(0) - eV(r)}^{\infty} \frac{dE}{4k_{\mathrm{B}}T} \frac{\tau_{\lambda ml}(r;E) v_{\lambda ml}(r;E)}{\cosh^2[(E - E_{\mathrm{F}})/2k_{\mathrm{B}}T]} \tag{5.22}$$

where $n_{1\mathrm{D}}$ is the total number of electron per unit length and $\tau_{\lambda ml}(r;E)$ denotes the total momentum relaxation time computed according to Malthiessen's rule

$$\frac{1}{\tau_{\lambda ml}} = \frac{1}{\tau^{\mathrm{SR}}_{\lambda ml}} + \frac{1}{\tau^{\mathrm{AC}}_{\lambda ml}}. \tag{5.23}$$

Also the group velocity $v_{\lambda ml}(r;E)$ must be a function of r since is related to the LDOS within the MLDA as

$$v_{\lambda ml}(r;E) = \hbar^{-1} A^{-1}_{\lambda m'l'}(r;E). \tag{5.24}$$

It is worth to mention that nonparabolic corrections in (5.16)-(5.24) have been taken into account within the framework of the MLDA.

5.4 Low-field conductivity within MLDA

The response to an uniform low electric field $\mathbf{E}$ is a current density $\mathbf{J}$ that is linearly related to the applied external field,

$$J = \sigma_{\mathrm{av}}\, E, \tag{5.25}$$

where the electric field has been applied only in the $z-$direction, i.e. $\mathbf{E} = E\mathbf{e_z}$. In case of a nanowire, the constant of proportionality, i.e. the average conductivity σ_{av}, has been defined as

$$\sigma_{\mathrm{av}} = \frac{2\,e}{R^2} \int_0^R \mathrm{d}r\, r\, n(r)\, \mu(r) = \frac{2}{R^2} \int_0^R \mathrm{d}r\, r\, \sigma(r). \tag{5.26}$$

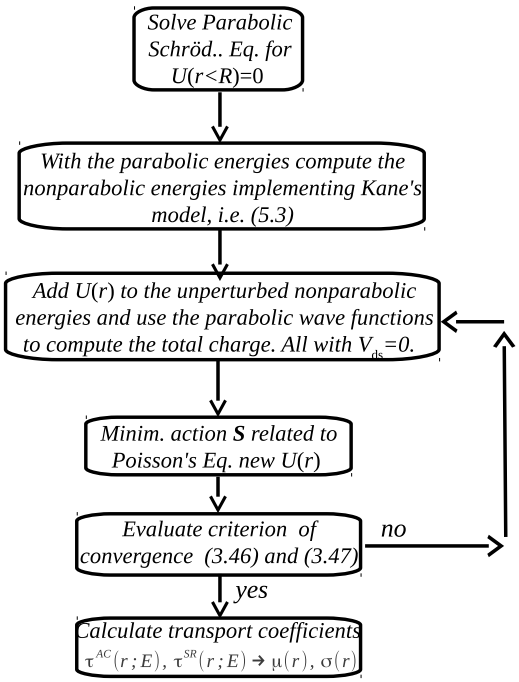

Figure 5.2: Flow chart of the simulation.

Since the electron concentration $n(r)$ and the mobility $\mu(r)$ depends on the potential $V(r)$, we can define $\sigma(r)$ as the low-field conductivity in the framework of the MLDA. Note that in the case of the full self-consistent solution σ does not depend on r, then from (5.26) it is found that $\sigma_{\rm av} = \sigma$, as expected.

5.5 Simulations

In order to present some simulations of low-field mobility and conductivity of a thin cylindrical gated silicon nanowire, we have used the following device parameters: the radius R ranges from 1 to 2.5 nm; the oxide thickness is taken to be 1 nm; the dielectric constant of the silicon and the oxide layer are ϵ_1 =11.8 and ϵ_2 =3.9, respectively; the doping density of the p-type silicon wire is 10^{16} cm^{-3}. The surface roughness parameters Δ and Λ for our calculations are 0.4 and 1.3 nm, respectively. The temperature is 300 K. In case of intravalley acoustic phonon scattering, we have used the deformation potential Ξ =12 eV [53]. Taking the transport direction to be [100], from the TB calculations for a silicon nanowire, it is found that the band structure presents four unprimed valleys, Δ_4, at the Γ point and two primed valleys, Δ_2, located at $k = \pm 0.336\pi/a_0$

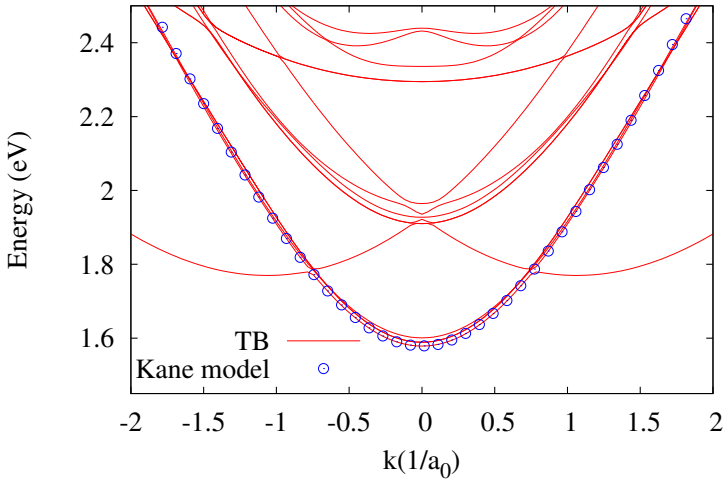

Figure 5.3: TB bandstructure for a cylindrical nanowire grown along the $\langle 100 \rangle$ *direction with* $R = 1nm$ *compares with the Kane's model (5.4). The length of the wire unit cell is* $a_0 = 0.53nm$.

[47], as observed in fig 5.3. Since the bottom of the band-edge of the Δ_2 valleys is higher than the ones corresponding to the Δ_4 valleys, for sake of simplicity, the influence of the Δ_2 valleys will not be considered in this work as well as the splitting of the four Δ_4 valleys, however, the 4-fold degeneracy has been taken into account. Therefore, the Kane's model is solely applied to the Δ_4 valleys whereas the parabolic Schrödinger equation (5.2) has been solved for the two doubly degenerate Δ_4 valleys, with effective masses $(m_{\text{trans}}, m_{\text{long}}, m_{\text{trans}})$, $(m_{\text{long}}, m_{\text{trans}}, m_{\text{trans}})$, $m_{\text{trans}} = 0.19\, m_0$ and $m_{\text{long}} = 0.91\, m_0$ being the transverse and longitudinal effective-masses respectively.

$R(nm)$	$E_0^{\text{TB}}(eV)$	$\alpha(1/eV)$
1.0	1.578	0.850
1.5	1.375	0.876
2.0	1.276	0.791
2.5	1.226	0.509

Table 5.1: The nonparabolic coefficients used in the analytical model.

In order to compute the nonparabolic coefficients, we have assumed a perfect cylindrical nanowire with an infinite potential barrier at the silicon/oxide interface. Then, taking only the lowest subband, $E_{01}^{\text{NP}}(0) = E^{\text{TB}}(0) - E_{\text{g}}$ in (5.4), we

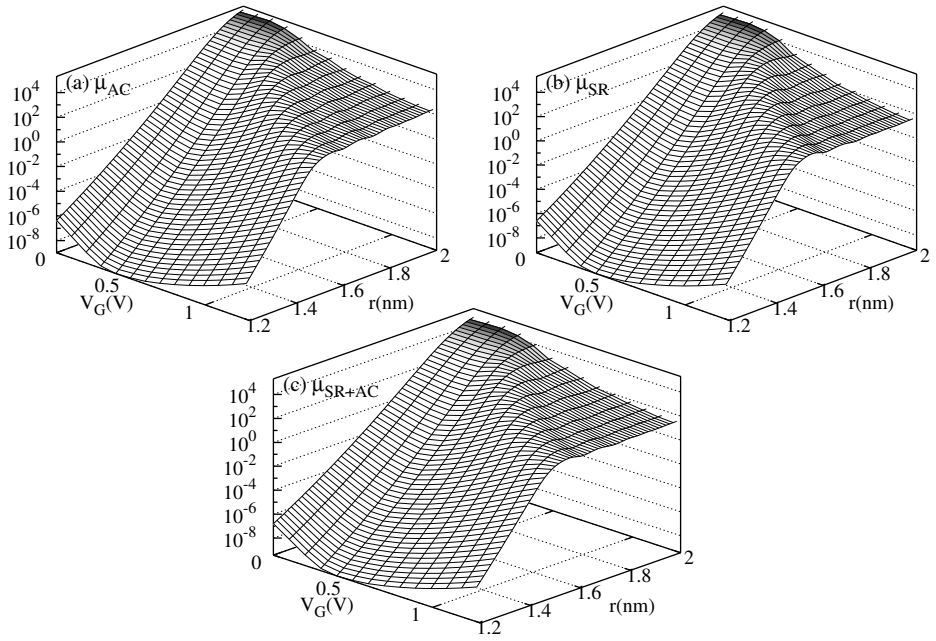

Figure 5.4: Low-field mobility calculated as function of $V_{\rm G}$ and r. The nanowire radius is R =2.0 nm. The low-field mobility is given in units of cm^2/Vs.

may find the following expression

$$\left(E_0^{\rm TB} - E_{\rm g}\right)\left[1 + \alpha\left(E_0^{\rm TB} - E_{\rm g}\right)\right] = W_{01}, \tag{5.27}$$

from which the nonparabolic coefficients α can be computed. $E_{\rm g}$ is the bulk silicon band-gap. In table 5.1, we have summarized the nonparabolic coefficients for different nanowire radii and their corresponding $E_0^{\rm TB}$. Also, in fig 5.3, it is plotted the TB bandstructure of a cylindrical nanowire with 1nm radius as well as the analytical bandstructure obtained from the Kane's model for the lowest Δ_4 valley with $\alpha = 0.850\ {\rm eV}^{-1}$.

Using the nonparabolic coefficients summarized in table 5.1, the low-field mobility and low-field conductivity have been calculated within the MLDA, however, we have first implemented the non-linear MLDA-based variational method to reach the self-consistency of Poisson and Schrödinger equations following the flow chart in Fig. 5.2 for our simulations. Then, once the potential is known, the momentum relaxation times $\tau^{\rm SR}(r;E)$ and $\tau^{\rm AC}(r;E)$ and, therefore, the low-field mobility $\mu(r)$ can be calculated within the framework of the MLDA. In Fig. 5.4, we have plotted the, acoustic (AC), surface roughness (SR) and total (SR+AC) low-field mobility as function of r for different $V_{\rm G}$. We may see that the mobility is very low near the center of the nanowire at low gate

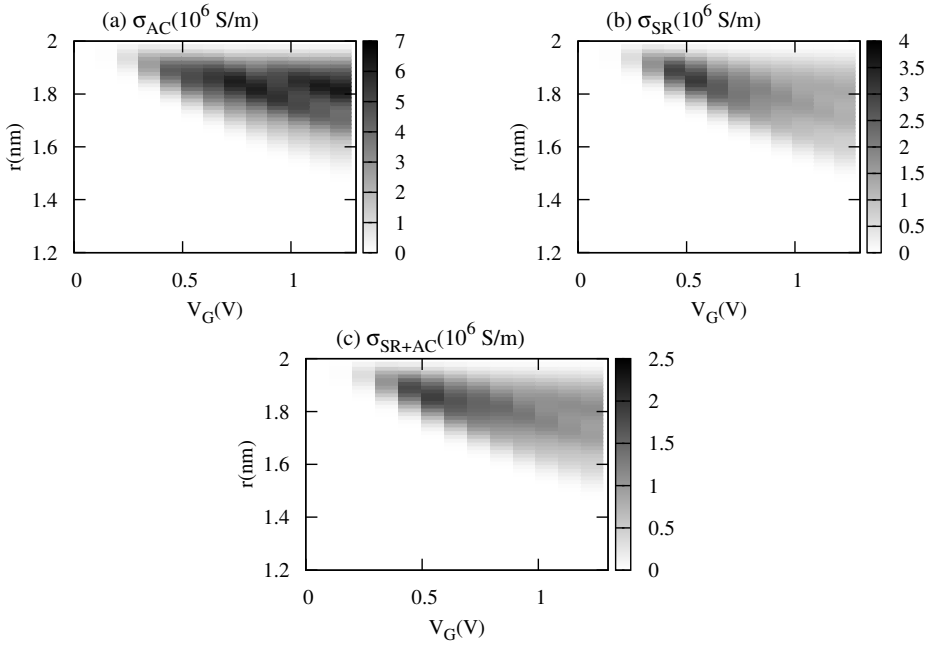

Figure 5.5: 3D low-field conductivity as function of $V_{\rm G}$ and r. The wire radius is R =2.0 nm.

voltage, i.e $V_{\rm G} \leq 0.5$V, whereas for higher gate voltages, the mobility starts increasing. Near the interface, for low gate voltages, the mobility remains almost constant, whereas, for high values of $V_{\rm G}$, the mobility deteriorates and reaches a saturation region. Both the AC-limited and SR-limited mobilities decrease since most of electrons are located near the interface region enhancing the AC and SR scattering. Comparing both the SR-limited and AC-limited mobilities, it is observed that the AC-limited mobility exceeds the SR-limited mobility. Also, notice that the low-field mobility does not vanish at $r = R$, because the electrons have velocity different from zero, nevertheless, their contribution to the low-field conductivity vanishes in case of a perfect nanowire as we may observe in Fig. 5.5, where it is plotted the contour of the low-field conductivity as function of r and $V_{\rm G}$. It is found that the low-field conductivity is much lower near the center of the nanowire than the conductivity near the interface, where the low-field conductivity stars increasing for low values of $V_{\rm G}$. However, in the case of SR scattering, the low-field conductivity decreases for high values of $V_{\rm G}$, contrary to the case of AC scattering, where its corresponding low-field conductivity keeps increasing. In both low-field mobility and low-field conductivity, we can observe oscillations at high $V_{\rm G}$ due to the contribution of electrons in the higher

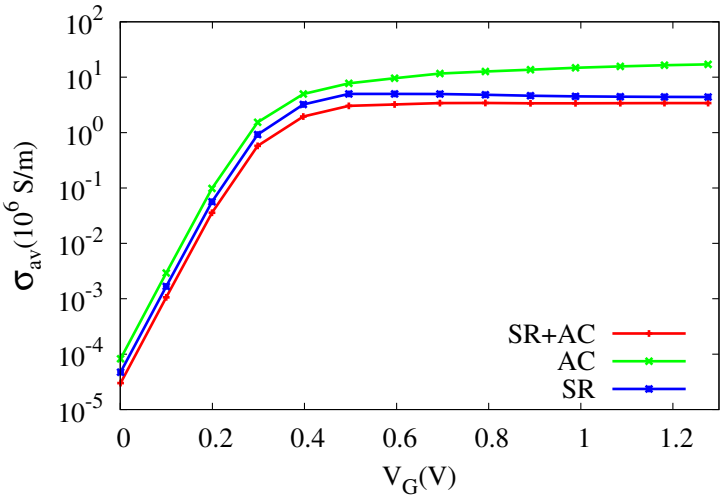

Figure 5.6: Low-field conductivity calculated as function of $V_{\rm G}$ for a nanowire with radius R =2.0 nm.

subbands.

In Fig. 5.6, it is plotted the low-field conductivity as a function of $V_{\rm G}$ and $R = 2$nm. We can observe that the low-field conductivity has an exponential behavior for low gate voltages and starts saturating at $V_{\rm G} \geq 0.4$V for both AC-limited and SR-limited conductivity. In case of the SR scattering, due to the high number of electrons near the interface, the conductivity is depressed for high values of $V_{\rm G}$ presenting a negative transconductance, i.e. $\partial\sigma_{\rm av}/\partial V_{\rm G} < 0$, whereas the SR+AC-limited conductivity saturates and remains constant. However, due to confinement it is mainly dominated by the SR-limited conductivity.

For sake of completeness, in Fig. 5.7, we have plotted the low-field conductivity for different nanowires radius, $R = 1$nm, 1.5nm, 2nm and 2.5nm. As we can see, for all values of R, the AC-limited conductivity exceeds the SR-limited conductivity. It is interesting that for thinner nanowires the low-field conductivity starts taking appreciable values at high values of $V_{\rm G}$, as observed in case of $R = 1$ nm where the gate voltage is $V_{\rm G} \approx 0.58$V. This is mainly due to the strong confinement in thin wires since their corresponding bandstructures present band gap energies higher than the gap found in case of bulk. Also, on the one hand, the AC-limited and SR-limited conductivity for thin nanowires are lower than the corresponding for thicker wires, whereas for higher values of $V_{\rm G}$, both low-field conductivities, saturate and reach approximately the same value as their counterpart for thicker wires. On the other hand, at low values of $V_{\rm G}$ the low-field conductivity is much lower in thinner than thicker nanowires.

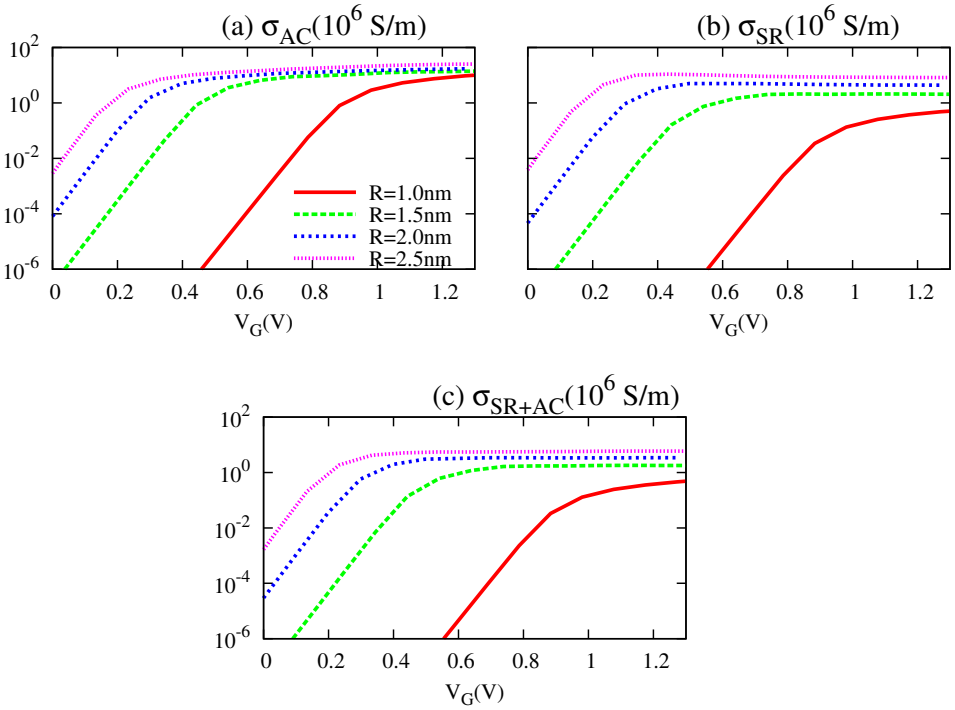

Figure 5.7: Low-field conductivity calculated as function of V_{G} for different nanowires radii.

This is because, in thick nanowires, the one-electron subbands are lower than in thinner nanowires. Therefore, more electrons can contribute easily to the low-field conductivity. However, the low-field conductivity is also depressed at high V_{G} in case of thick nanowires. If compare Fig. 5.7(b) and Fig. 5.7(c), it can be observed that the SR+AC-limited conductivity is mainly dominated by the SR-limited conductivity in case of thinner nanowires.

5.6 Conclusions

In conclusion, we have studied the low-field mobility and low-field conductivity for thin cylindrical nanowires within the framework of MLDA. The nonparabolic Kane's equation and Poisson's equation have been solved self-consistently by implementing the non-linear MLDA-based variational method. The nonparabolic coefficients were computed by a direct comparison with TB formalism, whereas, the Kubo-Greenwood formula for the mobility and the scattering relaxation times have been expressed within the framework of the MLDA. We have found that

the low-field conductivity for thinner nanowires is mainly dominated by the SR-limited conductivity. Also, the larger is the nanowire higher is the conductivity. However, the low-field conductivity saturates approximately at the same value. In case of thicker nanowires, it is observed negative transconductance in the high bias regime caused by the SR scattering. Nevertheless, the SR+AC-limited conductivity remains almost constant in the saturation regime.

6

Phonon-assisted Zener tunneling in a $p-n$ diode silicon nanowire

6.1 Introduction

Based on the Zener tunneling or band-to-band tunneling (BTBT) mechanism, the tunnel field-effect transistor (TFET) is considered a serious candidate to conquer various performance problems encountered by the latest generations of nanometer-sized metal-oxide-semiconductor field-effect transistors (MOSFETs) [56–60]. As the electrostatic control of the latter is found to be optimal for a cylindrical wire with a channel covered by an all-round gate, it's tempting to investigate the behavior of a TFET with the same geometry. As a first step, in this paper, we study BTBT tunneling in a reverse biased p–n diode that takes the form of a Si nanowire, a device structure which nowadays is particularly accessible by modern fabrication techniques.

In general, electronic conduction in semiconductors is negatively affected by elastic and inelastic scattering mechanisms such as electron – phonon scattering, leading to various intraband transitions that are known to degrade substantially the drive current [17, 37–39, 61]. On the other hand, Zener tunneling, considered as a conduction mechanism, heavily relies on interband transitions which, how-

*The results of this chapter were published as:
H. Carrillo-Nuñez, Wim Magnus, William G. Vandenberghe, Bart Sorée and F. M. Peeters, Solid Stat. Elec., http://dx.doi.org/10.1016/j.sse.2012.09.004, September, 2012 .

ever, may be seriously suppressed in semiconductors with an indirect bandgap, e.g. (bulk) Si. Indeed, in the latter case, the probability of a BTBT event transferring an electron from the top of the valence band (Γ-point) to the bottom of the conduction band (X-point) is negligible [62] unless the "missing" wave vector connecting Γ and X is made available. The latter can be provided by short-wavelength phonons that scatter with the transferring electrons and therefore phonon-assisted tunneling needs to be integrated into the calculation of the tunneling current. This was realized recently [9, 10] for planar devices where the large electric fields were incorporated directly in the one-particle Schrödinger equation, while the electron-phonon interaction was included perturbatively up to second-order. Here, we will extend the previous formalism to cylindrical wire geometries. The proposed nanowires are not surrounded by gates and, as such, cannot be expected to exhibit any transistor action, as a real TFET would do. However, as the present chapter focuses on the perspective of longitudinal BTBT as a vehicle for establishing tunneling drive currents, only z-dependent electric fields are accounted for. BTBT transitions triggered by strong, radial electric fields in gated wires, also referred to as "line tunneling" [9] will be examined elsewhere. The chapter is organized as follows. In section 6.2 we construct a self-consistent solution of Poisson's equation and the Schrödinger equation for electrons in both the conduction and valence band. Next, we use the resulting wave functions and energies compatible with the potential profile to modify the former expression of the tunneling current [9, 10] in accordance with the cyclindrical geometry. Numerical results are presented and discussed in section 6.3, and the chapter is concluded in section 6.4.

6.2 Phonon-assisted tunneling current

We consider a cylindrical $p-n$ junction taking the shape of a half p-doped and half n-doped Si nanowire connected to a (reverse) bias voltage $V_{\rm pn}$, as depicted in Fig. 6.1. The Zener tunneling current is computed as the sum of the contributions arising from all electron transitions between different valence and conduction subbands that are due to carrier confinement in the radial direction of the nanowire. The Schrödinger equations for electrons in the different subbands for both the valence and conduction band need to be solved self-consistently together with Poisson's equation in order to determine the spatial distribution of the mobile carriers and the potential profile felt by the carriers. The latter satisfies the boundary condition from the bias voltage $V_{\rm pn}$. Considering a [100]-oriented perfect cylindrical wire and adopting the effective-mass approximation, we may conveniently express the Hamiltonian for electrons in the valence (conduction)

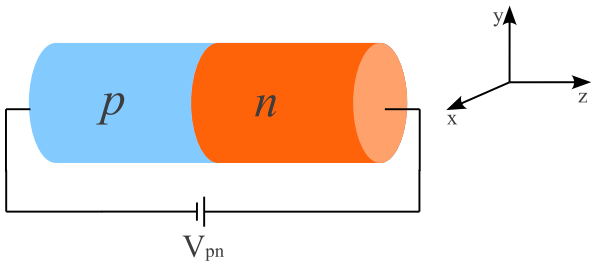

Figure 6.1: $p-n$ diode in a cylindrical Si nanowire.

band in terms of cylindrical coordinates as

$$H_{\mathrm{v(c)}\alpha} = \pm\frac{\hbar^2}{2m_{\mathrm{v(c)}\alpha\perp}}\left(\frac{\partial^2}{\partial r^2}+\frac{1}{r}\frac{\partial}{\partial r}+\frac{1}{r^2}\frac{\partial^2}{\partial\phi^2}\right)\pm\frac{\hbar^2}{2m_{\mathrm{v(c)}\alpha z}}\frac{\partial^2}{\partial z^2}+U(\mathbf{r}),$$

where the corresponding Schrödinger equations read

$$\left(E_{0\mathrm{v(c)}}+H_{\mathrm{v(c)}\alpha}\right)\Psi_{\mathrm{v(c)}\alpha}(\mathbf{r})=E_{\mathrm{v(c)}\alpha}\Psi_{\mathrm{v(c)}\alpha}(\mathbf{r}), \tag{6.1}$$

and the valence (conduction) band edges are denoted by $E_{0\mathrm{v(c)}}$, the band edge difference being equal to the bandgap $E_{0\mathrm{c}}-E_{0\mathrm{v}}=E_{\mathrm{g}}$. α is a valley index labeling various valleys within the conduction and valence bands, whereas $m_{\mathrm{v(c)}\perp\alpha}=2m_{\mathrm{v(c)}x\alpha}m_{\mathrm{v(c)}y\alpha}/(m_{\mathrm{v(c)}x\alpha}+m_{\mathrm{v(c)}y\alpha})$ and $m_{\mathrm{v(c)}z\alpha}$, respectively denote the effective mass in the planar cross section of the wire and the longitudinal effective mass in the transport direction. As detailed in Ref. [63], the effective masses $m_{\mathrm{v(c)}\perp\alpha}$ and $m_{\mathrm{v(c)}z\alpha}$ explicitly reflect the anisotropy of the conduction and valence band valleys of a [100] Si nanowire. For the sake of completeness, it should be noted that the axial symmetry of the Hamiltonian used in Eq. (6.1) is only approximate. Indeed, depending on the orientation of the conduction band valleys, the x and y components of the effective mass tensor, may differ and give rise to angular terms proportional to $\cos 2\phi$ and $\sin 2\phi$ when the kinetic energy operator is expressed in cylindrical coordinates. Ignoring these terms in a zeroth order approximation, one may in principle scrutinize its validity by calculating the second-order corrections to the unperturbed subband energies, as the first-order contributions vanish for symmetry reasons. On the other hand, adopting scalar effective masses for the valence band valleys, we note that both $m_{\mathrm{v}\alpha\perp}$ and $m_{\mathrm{v}\alpha z}$ coincide with these single, scalar masses. From the solution of the 3D Schrödinger equation, each energy eigenvalue $E_{\mathrm{v(c)}\alpha}$ and its corresponding wave function $\Psi_{\mathrm{v(c)}\alpha}(r,\phi,z)$ can be obtained. The potential energy $U(\mathbf{r})$ is composed of an electrostatic potential energy and an abrupt barrier at the semiconductor/oxide interface ($r=R$). As the latter is approximately taken to be infinite, it retains all carriers inside the nanowire thereby enforcing all wave functions to vanish at

$r = R$. Hence, the electron concentration emerging as a weighed sum over all squared wave functions is as well bound to vanish at $r = R$. In turn, the electrostatic potential solving Poisson's equation, given the electron concentration, will in principle depend on the radial coordinate r. However, in view of the large doping levels required to produce a huge electric field in the z-direction (within the junction area), the Debye length is significantly smaller than the wire radius for radii exceeding, say 2 nm. For extremely thin wires, this argument fails, but so would the effective mass approximation. Consequently, the electron concentration is uniform in the radial direction and, hence, the radial component of the electric field is negligible except in a very narrow region near $r = R$ the contribution of which to the current density would be negligible anyway. In this light, we may safely ignore the radial dependence of the electric field and the electrostatic potential and stick to a 1D Poisson equation relating the potential energy $U(z)$ to the total charge density $\rho(z)$. As a consequence, the 3D Schrödinger equation can be reduced to a 1D equation,

$$\left(E_{0\mathrm{v(c)}} \pm \frac{\hbar^2}{2m_{\mathrm{v(c)}\alpha z}}\frac{\partial^2}{\partial z^2} + U(z)\right)\chi_{\mathrm{v(c)}\alpha ml;k}(z) = \left(E_{\mathrm{v(c)}\alpha} - W_{\mathrm{v(c)}\alpha ml}\right)\chi_{\mathrm{v(c)}\alpha ml;k}(z). \quad (6.2)$$

The subband eigenfunctions and their corresponding eigenvalues $W_{\mathrm{v(c)}\alpha ml}$ describing the subbands in the radial and azimuthal directions can be expressed as

$$\begin{aligned} R_{ml}(r,\phi) &= \frac{J_m\left(\frac{x_{ml}r}{R}\right)\mathrm{e}^{\mathrm{i}m\phi}}{\sqrt{\pi R^2}|J_{m+1}(x_{ml})|}, \\ W_{\mathrm{v(c)}\alpha ml} &= \mp\frac{\hbar^2 x_{ml}^2}{2m_{\mathrm{v(c)}\alpha\perp}R^2}, \end{aligned} \quad (6.3)$$

where x_{ml} is the lth zero of the mth Bessel function $J_m(x)$. In the transport direction, the Schrödinger equation in Eq.(6.2) is evaluated numerically for each subband labeled by the azimuthal and radial quantum numbers m and l, and for each longitudinal quantum number k.

The valence (conduction) band spectral function can be found from its defin-

ing expression based on the electron wave functions [10],

$$\begin{aligned} A_{\mathrm{v(c)}}(\mathbf{r},\mathbf{r}';E) &= 2\pi \sum_{\alpha,m,l} R_{ml}(r,\phi) R^{*}_{ml}(r',\phi') \\ &\times \sum_{k} \chi_{\mathrm{v(c)}\alpha ml;k}(z)\delta(E - E_{\mathrm{v(c)}\alpha ml;k})\chi^{*}_{\mathrm{v(c)}\alpha ml;k}(z') \\ &= \sum_{\alpha,m,l} R_{ml}(r,\phi) R^{*}_{ml}(r',\phi') A_{\mathrm{v(c)}\alpha ml}(z,z';E). \end{aligned} \tag{6.4}$$

Putting $z = z'$ in the latter, we compute the net charge density from

$$\begin{aligned} \rho(z) = eN_{\mathrm{D}}(z) - eN_{\mathrm{A}}(z) &+ \frac{2e}{\pi R^2}\int \frac{\mathrm{d}E}{2\pi}\left[(1 - f_{\mathrm{v}}(E)) \sum_{\alpha,m,l} A_{\mathrm{v}\alpha ml}(z,z;E)\right. \\ &- \left. f_{\mathrm{c}}(E) \sum_{\alpha,m,l} A_{\mathrm{c}\alpha ml}(z,z;E)\right] \end{aligned} \tag{6.5}$$

where $N_{\mathrm{D(A)}}$ is the donor (acceptor) doping concentration, whereas f_{v} and f_{c} respectively denote the Fermi-Dirac functions for the valence and conduction bands. Their corresponding chemical potentials are fixed by imposing charge neutrality in the source and drain regions.

Once the Schrödinger and Poisson equations are solved self-consistently, the phonon-assisted current density may be computed from [10]

$$\begin{aligned} J = -\frac{2e}{\pi R^2 \hbar}\int \frac{\mathrm{d}E}{2\pi}\Bigg[&\Bigg(f_{\mathrm{v}}(E)(1 - f_{\mathrm{c}}(E - \hbar\omega_{\mathbf{k}_0}))(\nu(\hbar\omega_{\mathbf{k}_0}) + 1) \\ &- f_{\mathrm{c}}(E - \hbar\omega_{\mathbf{k}_0})(1 - f_{\mathrm{v}}(E))\nu(\hbar\omega_{\mathbf{k}_0})\Bigg) T^{\mathrm{em}}_{\mathrm{v}}(E) \\ &+ \Bigg(f_{\mathrm{v}}(E)(1 - f_{\mathrm{c}}(E + \hbar\omega_{\mathbf{k}_0}))\nu(\hbar\omega_{\mathbf{k}_0}) \\ &- f_{\mathrm{c}}(E + \hbar\omega_{\mathbf{k}_0})(1 - f_{\mathrm{v}}(E))(\nu(\hbar\omega_{\mathbf{k}_0}) + 1)\Bigg) T^{\mathrm{abs}}_{\mathrm{v}}(E)\Bigg] \end{aligned} \tag{6.6}$$

with the tunneling probability given by

$$\begin{aligned} T_{\mathrm{v}}^{\mathrm{abs,em}}(E) &= \Omega|M'_{\mathbf{k}_0}|^2 \sum_{\alpha,\alpha'} \sum_{ml,m'l'} F_{ml,m'l'} \\ &\quad \times \int \mathrm{d}z A_{\mathrm{v}\alpha' m'l'}(z,z;E) A_{\mathrm{c}\alpha ml}(z,z;E \pm \hbar\omega_{\mathbf{k}_0}) \\ &= \sum_{\alpha,\alpha'} \sum_{ml,m'l'} T^{\mathrm{abs,em}}_{\mathrm{v};\alpha ml,\alpha' m'l'}(E) \end{aligned} \tag{6.7}$$

where the electron-phonon interaction is measured by $\Omega|M'_{\mathbf{k}_0}|^2$, $\Omega = \pi R^2 L_{\mathrm{W}}$ stands for the wire volume, and $\hbar\omega_{\mathbf{k}_0}$ is the phonon energy that is required for the transition between the valence band and the conduction band valley. $\nu(E)$ is the Bose-Einstein distribution function, while $F_{ml,m'l'}$ denotes the form factor,

$$F_{ml,m'l'} = \frac{2\pi}{\pi^2 R^4 J^2_{m+1}(x_{ml}) J^2_{m'+1}(x_{m'l'})} \int_0^R \mathrm{d}r\, r J_m^2\left(\frac{x_{ml} r}{R}\right) J_{m'}^2\left(\frac{x_{m'l'} r}{R}\right). \tag{6.8}$$

Each of the terms appearing in Eq. (6.6) can be straightforwardly interpreted in terms of transitions from valence to conduction band (or vice versa) assisted by the emission or absorption of a phonon [9, 10]. Correspondingly, energy conservation accompanying these interband transitions and involving both intersubband scattering with wave vectors changing along the axial direction, is typically ensured by Dirac delta functions of the form $\delta(E_{\mathrm{v},l,m} - E_{\mathrm{c},l',m'} \pm \hbar\omega_{\mathbf{k}_0})$ appearing in the spectral functions, as explained in Ref. [10]. In contrast to carrier confinement being reflected in the form factors that directly affect carrier – phonon coupling, phonon confinement is ignored in this work. The justification lies in the nanowire diameter range which, throughout this chapter, is deliberately chosen to exceed 4 nm. On one hand, Si nanowires in this range exhibit an indirect bandgap which is a key feature for studying phonon-assisted BTBT. On the other hand, it has been found that the phonon spectra of these thicker nanowires are rapidly approaching their bulk values. For instance, Raman spectroscopy of Si nanowires [64] reveals that the width of the Gaussian confinement function which is a valuable indicator of the dependence of phonon confinement on the wire diameter, is hardly sensitive to the diameter in the range 4 – 25 nm.

6.3 Results and discussion

The Zener tunneling current is calculated for a $p-n$ cylindrical diode Si nanowire at 300 K, as sketched in Fig. 6.1. The $p-n$ junction is located at $z = 6$ nm and is considered abrupt with the p-type source and n-type drain regions being

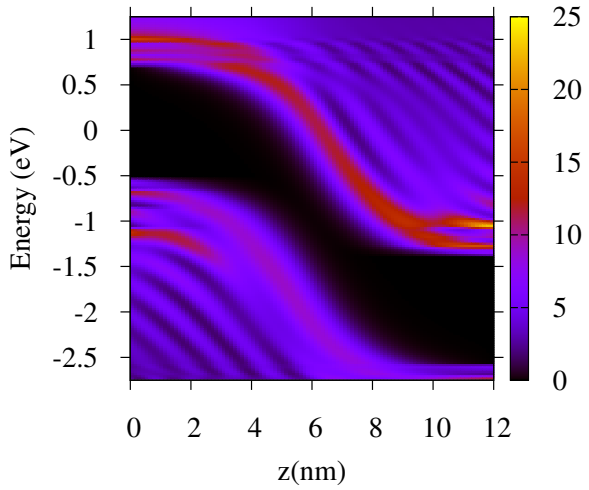

Figure 6.2: Contour plot of the valence and conduction band spectral functions (expressed in eV^{-1} nm^{-1}) for a $p-n$ diode in a cylindrical nanowire with length $L_{\rm W} = 12$ nm and radius $R = 2.5$ nm. The applied voltage is $V_{\rm pn} = 0.12$ V and the $p-n$ junction is located at $z = 6$ nm.

doped symmetrically up to $N_{\rm A} = N_{\rm D} = 10^{20}$ cm^{-3}, while the nanowire diameter ranges from 4 to 8 nm and its length is fixed to $L_{\rm W} = 12$ nm. In this study, the transport is assumed to be in the [100] direction. However, tunneling attributed to valleys with the heavy mass, $m_l = 0.916\, m_0$, in the transport direction [100] can be neglected. Only the contribution due to tunneling from the valence band, with (0.49,0.49,0.16)m_0, to the conduction band of valleys with transverse mass, $m_t = 0.19\, m_0$, in the [100] direction needs to be taken into account [62]. On the other hand, for the evaluation of the phonon-assisted tunneling probability, the transverse acoustic (TA) and transverse optical (TO) phonons provide the main contribution. For the TA branch, the electron-phonon strength is given by $\Omega|M'_{\mathbf{k}_0}|^2 = 4.86 \times 10^{-25}$ eV^2 cm^3 and the phonon energy reads $\hbar\omega_{\mathbf{k}_0} = 18.4$ meV, whereas for TO phonons we have $\Omega|M'_{\mathbf{k}_0}|^2 = 9.31 \times 10^{-25}$ eV^2 cm^3 and $\hbar\omega_{\mathbf{k}_0} = 57.6$ meV. The above parameters were taken from Ref. [62]. Fig. 6.2 shows a contour plot of the spectral functions for both the valence and conduction band of the cylindrical nanowire $p-n$ diode. Not only do the spectral functions reflect the signatures of the first few subbands, they are also found to oscillate due to quantum reflections of the wave functions along the z-direction. Particularly, the electron wave function states injected respectively from the source and drain

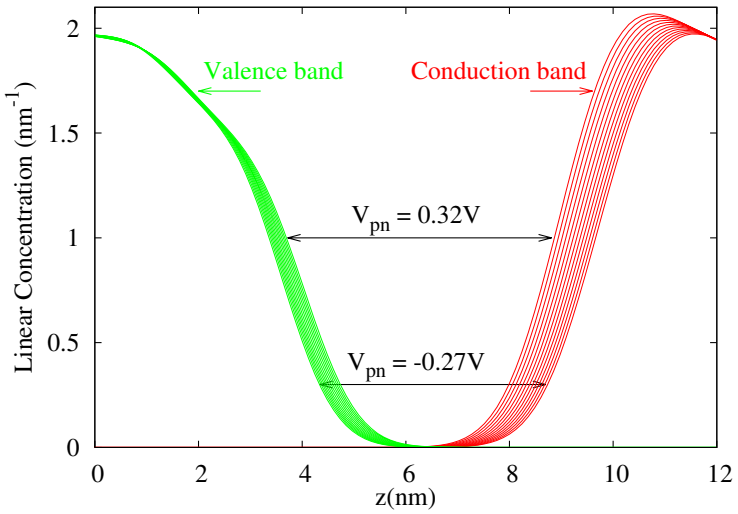

Figure 6.3: Linear electron concentration for the valence (green) and conduction band (red) along the $p-n$ junction of the cylindrical nanowire with $V_{\rm pn}$ ranging between -0.27 V and 0.32 V. The $p-n$ junction is located at $z = 6$ nm.

regions, are reflected by the Zener tunneling junction barrier causing interference with the injected states, while part of the wave function penetrates the barrier to decay in the opposite contact. The latter can be observed in Fig. 6.3 where the linear electron concentration – i.e. the number of electrons per unit length in the z direction – of the conduction and valence bands are shown for $V_{\rm pn}$ ranging from -0.27 V to 0.32 V. Near and inside the Zener tunneling barrier, the concentration is found to decay with a small amount of carriers residing inside the barrier region. The overlap between the corresponding states is triggering the Zener tunneling events and therefore the occurrence of the tunnel current. In Figs. 6.4(a, b) the Zener tunneling current densities are plotted separately for electrons interacting respectively with TO and TA phonons, for different nanowire radii. It turns out that the current substantially depends on the wire radius in the case of moderate backward bias ($V_{\rm pn} \approx -0.13$ V) and forward bias ($V_{\rm pn} > 0$). The current being lower in the thinner nanowires could be explained by noting that only the lowest subbands are occupied in thinner nanowires and, hence, the number of transmission channels contribution to the tunneling current is lower than in the case of thicker wires. In all cases, the presence of short-wavelength phonons is paramount to initiate interband transition whereas the direct tunneling component to the Zener current turns out to be negligible. The latter cannot be directly concluded from the present formalism which is by construction dealing only with phonon-assisted tunneling. Nevertheless, our conclusion is supported by direct

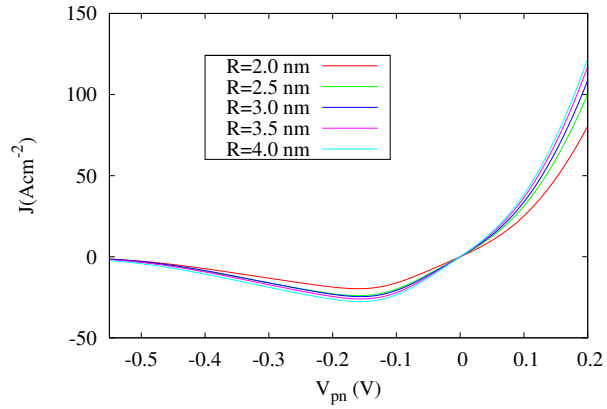

(a)

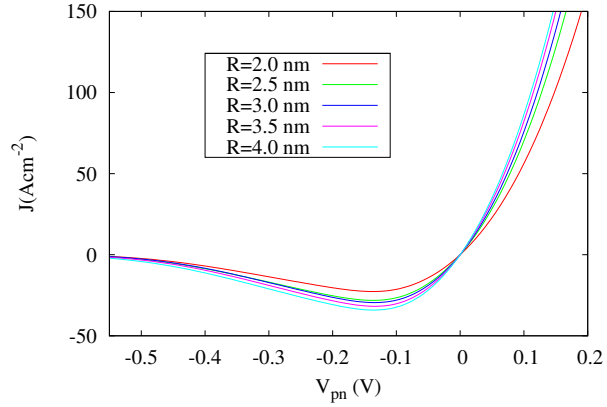

(b)

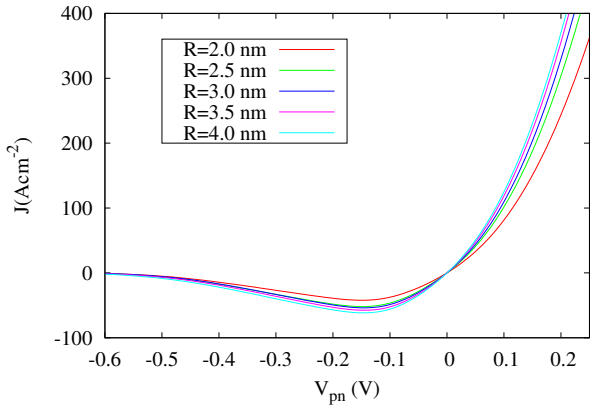

(c)

Figure 6.4: Zener tunneling current density versus bias voltage calculated for different Si body radii: contribution from electrons interacting with (a) TO phonons and (b) TA phonons. The total current is shown in (c). The doping concentrations are $N_{\rm D} = N_{\rm A} = 10^{20}$ *cm*$^{-3}$.

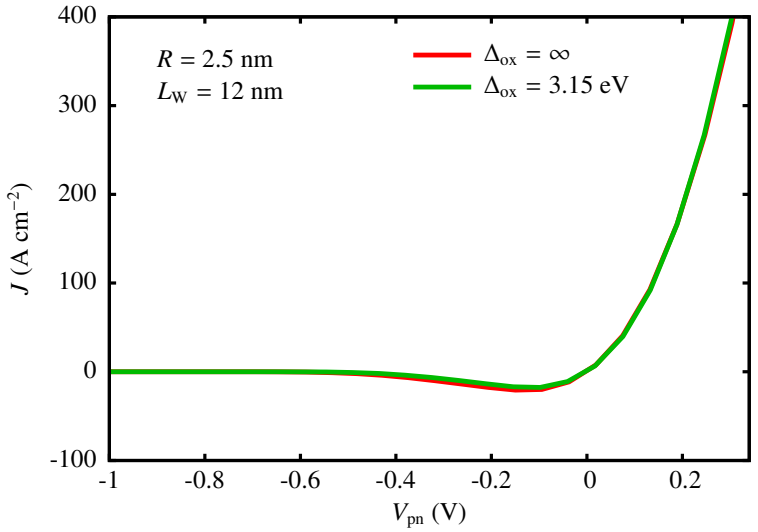

Figure 6.5: Comparison of the total tunneling current calculated for a finite oxide barrier (green) and its infinite barrier counterpart (red) along the $p-n$ junction of the cylindrical Si nanowire with $R = 2.5$ nm and $L_W = 12$ nm. Corresponding to SiO_2, the barrier height and the electron effective mass in the oxide region are resp. taken to be $\Delta = 3.15$ eV and $m_{ox} = 0.5m_0$, whereas the oxide layer thickness is assumed to be 1 nm.

comparison of the transmission coefficients $T_v^{abs}(E), T_v^{em}(E)$ with Kane's model used for direct tunneling. Kane's transmission coefficient for a uniform electric field F at the Γ-point can be expressed as [65, 66]

$$T_{\text{Kane}} = \frac{\pi^2}{9} \exp\left(-\frac{\pi E_{g,\text{direct}}^{3/2}}{4\hbar F} \sqrt{\frac{2m_0\, m_v}{m_0 + m_v}} \right) \tag{6.9}$$

where $E_{g,\text{direct}}$ and m_v respectively denote the direct band gap at the Γ-point and the valence band effective mass. Having adopted Si based parameter values, $m_v = 0.57m_0$, $E_{g,\text{direct}} = 3.2$ eV, we have estimated the direct transmission coefficient to be $T_{\text{Kane}} = 5 \times 10^{-11}$ where F is chosen to be the electric field at the center of the p-n junction. On the other hand, it turns out that the phonon-assisted BTBT transmission coefficient calculated in this work peaks around 5×10^{-6}, thus prominently surpassing direct tunneling by 5 orders of magnitude. Next, it should be noticed that, for $V_{pn} \gg 0$, the tunneling current assisted by TA phonons exceeds its counterpart due to TO phonons, especially in the high bias regime.

For the sake of comparison, we have further relaxed the infinite oxide barrier approximation and repeated the calculation for a 2.5 nm thick nanowire, allowing

for wave function penetration into the oxide layer. The corresponding tunneling current and its infinite barrier counterpart are plotted in Fig. 6.5. Comparison of both curves reveals that wave function penetration and the corresponding reduction of the ground-state subband energy do not lead to substantial current enhancement, particularly in the high bias regime. Finally, one should bear in mind that all calculations presented in this work rely on the effective mass approximation. Extending the results of this paper to wire diameters significantly smaller than 4 nm, one should realize that the valley separation in the subband ladders is no longer preserved, as was demonstrated by Neophytou et. al. [67]. Hence, a more sophisticated description of the band structure, e.g. using $\mathbf{k} \cdot \mathbf{p}$ theory or tight binding techniques, would be in order.

6.4 Conclusion

In summary, the phonon-assisted Zener tunneling current was computed in the case of a $p - n$ junction embedded in a cylindrical nanowire. A Schrödinger-Poisson self-consistent solution was performed in order to calculate the hole and electron spectral functions as well as the electrostatic potential. The basic expression for the tunneling current incorporates scattering between electrons and TA and TO phonons, and the calculations were repeated for different nanowire radii. As a result, the separate contributions to the current corresponding to the two phonon types as well as its dependence on the wire radius could be extracted. It is found that interband transitions caused by TA phonons provide the major contribution to the Zener tunneling current in the case of forward bias, while the contributions from TA and TO phonons are comparable in the reverse bias regime. Furthermore, penetration of the carriers into the oxide layer hardly enhances the tunneling current and does not appreciably affect the role of phonons as being the mediating mechanism. Finally, the tunneling current substantially depends on the wire radius for both moderate reverse and sufficiently large forward bias voltages.

7

Phonon-assisted Zener tunneling in a cylindrical nanowire TFET

7.1 Introduction

Recently, the tunneling field-effect transistor (TFET), based on Zener tunneling or band-to-band tunneling (BTBT), is considered as possible candidate to overcome the 60 mV/dec sub-threshold slope problem that limits the performance of nanometer-sized metal-oxide-semiconductor field-effect-transistors (MOSFETs). In this light, considerable efforts have been made to optimize the TFET working principle, and various device configurations have been proposed [68,69], consisting of a reverse-bias $p-i-n$ diode structure with the p (n) doped region which acts as a source (drain) contact. Rather than having the intrinsic channel gated, an alternative device with a gate surrounding the top of the source region [9] was proposed, and it was found that, under high gate bias, a tunneling current proportional to the gate length – also referred to as line tunneling current – emerges in the case of a planar TFET. In this chapter, we investigate the line tunneling of a cylindrical nanowire TFET with an all-round gate covering the source as depicted in Fig. 7.1, in analogy with the planar device. We will focus on relatively thick wires, i.e. 5-8 nm diameter, for which the band structure is bulk-like with an indirect bandgap. Moreover, we will adopt the effective mass approximation and account for the leading effects of the phonon distribution on the tunneling current. The inclusion of the latter is paramount as BTBT in an indirect semi-

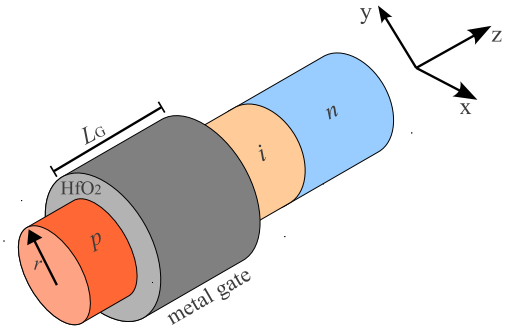

Figure 7.1: Cylindrical nanowire TFET with an all-around gate on top of the source.

conductor is mediated by electron-phonon interaction. In order to calculate the BTBT current, the new approach proposed in Ref. [10], will be adopted that is able to deal with large electric fields in the one-electron Schrödinger equations for the valence and conduction bands. Considering a long gate on top of the source and neglecting edge effects and fringing fields, one may restrict the self-consistency requirement to the source region.
Moreover, most of the available transport formalisms, such as the non-equilibrium Green's function method [17], Pauli's master equation [39], Wigner's transport equation [37] and the quantum mechanical energy and momentum balance equations [70] are computationally expensive when it comes to include the subband structure of both the valence and the conduction band. Therefore, we will implement the non-linear MLDA-based variational approach being devised originally for treating electronic transport in ordinary nanowire MOSFETs as explained in chapters 4 and 3. In the subsequent sections, we will show how to extend the MLDA-based variational approach to calculate the carrier concentrations in both the conduction and valence bands, as well as, the tunneling current formula and the tunneling probabilities within the framework of the MLDA. As a major conclusion, it is observed that the onset voltage of the tunneling current crucially depends on the nanowire radius.

7.2 The MLDA for a cylindrical nanowire TFET

In principle, any detailed study of the concentration of electrons in both the valence and conduction band involve a self-consistent solution of the 3D Schrödinger and Poisson equations. Adopting again the effective-mass approximation, the one-electron Hamiltonian for a perfect cylindrical nanowire may con-

veniently express as

$$H = E_{0\mathrm{v(c)}} \pm \frac{\hbar^2}{2m_{\mathrm{v(c)}\alpha\perp}} \left(\frac{\partial^2}{\partial r^2} + \frac{1}{r}\frac{\partial}{\partial r} + \frac{1}{r^2}\frac{\partial^2}{\partial \phi^2} \right) \pm \frac{\hbar^2}{2m_{\mathrm{v(c)}\alpha z}} \frac{\partial^2}{\partial z^2} + U(r,z), \tag{7.1}$$

where the valence (conduction) band edge is denoted by $E_{0\mathrm{v(c)}}$. α is a conduction band valley index whereas $m_{\mathrm{v(c)}\alpha\perp}$ and $m_{\mathrm{v(c)}\alpha z}$ are the effective masses in the planar cross-section of the wire and the longitudinal mass the in z-direction, respectively. The total potential energy $U(r,z) = -eV(r,z) + U_{\mathrm{B}}\,\theta(r > R)$ incorporates the electrostatic potential $V(r,z)$ obeying Poisson's equation

$$\nabla^2 V(r,z) = -\frac{1}{\epsilon}\,\rho(r,z) \tag{7.2}$$

as well as the abrupt energy barrier U_{B} at the semiconductor/oxide interface $r = R$. For the sake of simplicity, the barrier height U_{B} is assumed to be infinitely high, thereby confining all electrons to the interior of the wire.

Dealing particularly with line tunneling related to the radial gate action of a nanowire TFET, we treat the radial potential variations using a genuine quantum description whereas the z dependence of the potential profile is included as a classical perturbation. As a first step, we consider the radial potential $V_1(r)$ corresponding to an all-round biased gate that is sufficiently long to neglect the z-dependence of V_1. Next, we assume that the z-dependence of the real potential $V(r,z)$, reflecting the finiteness of the gate and the applied drain voltage V_{ds} is smooth compared to the steepness of the radial potential well $V_1(r)$ due to the positive gate voltage V_{G}. At this point, we may invoke the MLDA, which accordingly to section 4.3, the Hamiltonian (7.1) can be conveniently split in two parts, $H = H_1 + H_2$, with

$$\begin{aligned} H_1 &= E_{0\mathrm{v(c)}} + \hat{T}_\perp - eV_1(r) \\ &= E_{0\mathrm{v(c)}} \pm \frac{\hbar^2}{2m_{\mathrm{v(c)}\alpha\perp}} \left(\frac{\partial^2}{\partial r^2} + \frac{1}{r}\frac{\partial}{\partial r} + \frac{1}{r^2}\frac{\partial^2}{\partial \phi^2} \right) - eV_1(r) \end{aligned} \tag{7.3}$$

$$H_2 = \hat{T}_\parallel - eV_2(r,z) = \pm\frac{\hbar^2}{2m_{\mathrm{v(c)}\alpha z}}\frac{\partial^2}{\partial z^2} - eV_2(r,z). \tag{7.4}$$

$\hat{T}_\perp$ and $\hat{T}_\parallel$, respectively, represent the transverse and longitudinal parts of the kinetic energy operators while the eigenvalue problem of H_1 is supposed to be solved rigorously for its eigenfunctions

$$\frac{\mathrm{e}^{\mathrm{i}m\phi}}{\sqrt{2\pi}} R_{\nu\mathrm{v(c)}}(r) \tag{7.5}$$

and the corresponding eigenvalues $W_{\nu\mathrm{v(c)}}$, whereas the correcting potential $V_2(r,z)$ $= V(r,z) - V_1(r)$, i.e. the difference between the real and model potential, is treated classically, then it can be added to the energy in the LDOS obtained by integrating (3.16) for $\mathbf{r} = \mathbf{r}'$,

$$A_{\mathrm{v(c)}}(r,z,r,z;E) = \sqrt{\frac{m_{\mathrm{v(c)}\alpha z}}{8\pi^2\hbar^2}} \sum_{\nu} \left|R_{\nu\mathrm{v(c)}}(r)\right|^2 \left[\mp(E + eV_2(r,z)) \pm W_{\nu\mathrm{v(c)}}\right]^{-\frac{1}{2}}$$
$$= \sum_{\nu} \left|R_{\nu\mathrm{v(c)}}(r)\right|^2 A_{\nu\mathrm{v(c)}}(z,z;E + eV_2(r,z)). \tag{7.6}$$

Note that, for the sake of notational simplicity, the angular momentum quantum number m and the valley index α are absorbed in the index ν which labels the radial subband ladder.

Accordingly to (7.6), the concentration of electrons occupying the valence and conduction subbands inside the nanowire TFET are expressed as

$$n_{\mathrm{v(c)}}(r,z) = 2\int \mathrm{d}E A_{\mathrm{v(c)}}(\mathbf{r},\mathbf{r};E)\,\mathcal{F}_{\mathrm{v(c)}}(E)$$
$$= \frac{1}{\pi}\sum_{\nu}\left|R_{\nu\mathrm{v(c)}}(r)\right|^2 \int \mathrm{d}k\,\mathcal{F}_{\mathrm{v(c)}}[E_{k\nu\mathrm{v(c)}} + W_{\nu\mathrm{v(c)}} - eV_2(r,z)], \tag{7.7}$$

with $\mathcal{F}_{\mathrm{v}}(E) = 1 - f_{\mathrm{v}}(E)$ and $\mathcal{F}_{\mathrm{c}}(E) = f_{\mathrm{c}}(E)$. $f_{\mathrm{v}}(E)$ and $f_{\mathrm{c}}(E)$ denote the Fermi-Dirac functions for the valence and conduction band determined by the source and drain applied voltage, respectively. Appearing in $E_{k\nu\mathrm{v(c)}} = \pm\hbar^2k^2/2m_{\mathrm{v(c)}z\alpha}$, k represents the wave vector in the z-direction. As an immediate consequence of the MLDA approximation, the total charge density containing the contributions outlined in (7.7), emerges as a local functional of $V_2(r,z)$, i.e.

$$\rho[r,V_2(r,z)] = e\Big(n_{\mathrm{v}}[r,V_2(r,z)] - n_{\mathrm{c}}[r,V_2(r,z)] - N_{\mathrm{A}}\Big), \tag{7.8}$$

where N_{A} is the acceptor concentration. Consequently, we are in a position to apply a non-linear variational principle that was introduced earlier in chapter 3 to simplify the self-consistent solution of the Poisson and Schrödinger equations within the framework of the MLDA. The contributions to the action functional due to the mobile electrons in the valence(conduction) band can be extracted from

$$S_{\mathrm{v(c)}} = \mp 2\pi k_{\mathrm{B}}T \sum_{\nu} C_{\nu\mathrm{v(c)}} \int_0^R \mathrm{d}r\, r \left|R_{\alpha,\mathrm{v(c)}}(r)\right|^2 \int_0^{L_{\mathrm{G}}} \mathrm{d}z$$
$$\times \int \mathrm{d}k \ln\left[1 + \exp\left(\mp\frac{E_{k\nu,\mathrm{v(c)}} - E_{\mathrm{Fv(c)}} - eV_2(r,z)}{k_{\mathrm{B}}T}\right)\right], \tag{7.9}$$

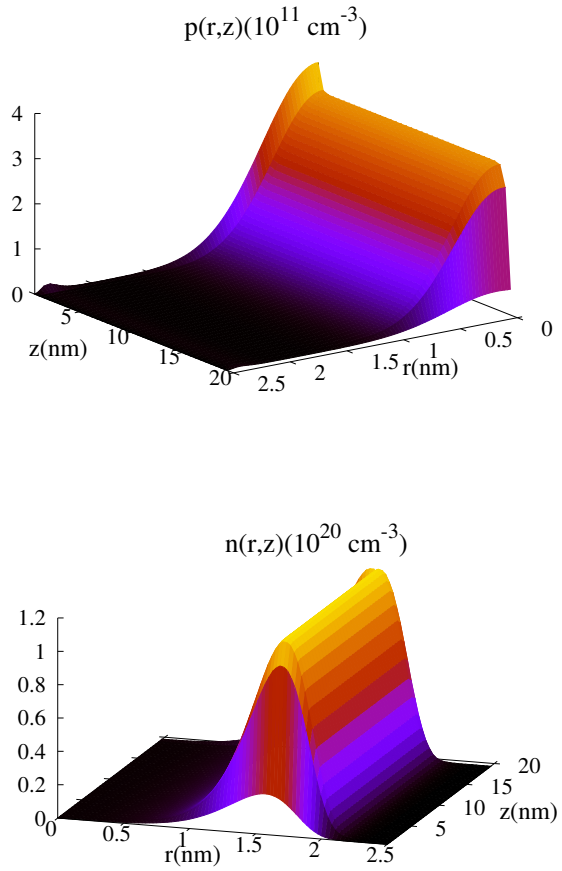

Figure 7.2: 3D (a) hole and (b) electron concentration as function of z and r inside the nanowire TFET at $V_{\rm ds} = 0.6$ V and $V_{\rm G} = 2.4$ V.

where $E_{\rm Fv(c)}$ is the Fermi-level for electrons in the valence (conduction) band. The contributions arising from the fixed acceptor dopants can be calculated similarly.

7.3 Band-to-Band tunneling current within MLDA

Once the Schrödinger and Poisson equations are solved self-consistently, the potential profile $V(r, z)$ is known and the band-to-band tunneling probability

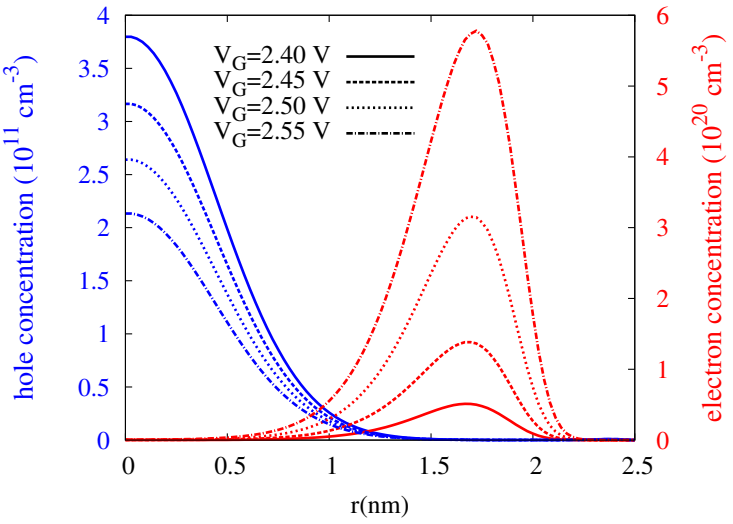

Figure 7.3: Hole and electron concentration along the radial direction at the center of a cylindrical nanowire TFET ($z = L_G/2$) for various V_G ranging from 2.4 V to 2.55 V with steps of 0.05 V for $V_{ds} = 0.6$ V. The oxide barrier is at $r = 2.5$ nm, and the gate work function is taken to be WF = 4.66 eV.

can be computed from (2.41) within the MLDA as,

$$\begin{aligned} T_{\mathrm{v}}^{\mathrm{abs,em}}(E) \;=\; & \Omega\,|M'_{\mathbf{k}_0}|^2 \sum_{\nu,\nu'} \int_0^R \mathrm{d}r\, r R^2_{\nu\mathrm{c}}(r) R^2_{\nu'\mathrm{v}}(r) \\ & \times \int_0^{L_G} \mathrm{d}z\, A_{\nu'\mathrm{v}}\left(z,z;E+eV_2(r,z)\right) A_{\nu\mathrm{c}}\left(z,z;E+eV_2(r,z)\pm\hbar\omega_{\mathbf{k}_0}\right) \\ & = \sum_{\nu,\nu'} \int_0^R \mathrm{d}r\, r R^2_{\nu\mathrm{c}}(r) R^2_{\nu'\mathrm{v}}(r)\, T^{\mathrm{abs,em}}_{\nu\nu'\mathrm{v}}(r;E). \end{aligned} \tag{7.10}$$

$M'_{\mathbf{k}_0} = D|\mathbf{k}_0|\sqrt{\hbar/2\rho_s\omega_{\mathbf{k}_0}\Omega}$ is the electron-phonon interaction matrix element for a phonon with energy $\hbar\omega_{\mathbf{k}_0}$ that mediates a transition between the valence band top and one of the conduction band minima, whereas ρ_s, $D|\mathbf{k}_0|$ and Ω, respectively, stand for the semiconductor mass density, the interband deformation potential and the device volume. Then, the phonon-assisted line current density

which reduces to its z-component is computed from as

$$J_z(r) = -\frac{2e}{\hbar}\sum_{\nu,\nu'} R^2_{\nu\mathrm{c}}(r)R^2_{\nu'\mathrm{v}}(r)\int\frac{\mathrm{d}E}{2\pi} \times\Bigg[\Bigg(f_{\mathrm{v}}(E)(1-f_{\mathrm{c}}(E-\hbar\omega_{\mathbf{k}_0}))(\nu(\hbar\omega_{\mathbf{k}_0})+1) -f_{\mathrm{c}}(E-\hbar\omega_{\mathbf{k}_0})(1-f_{\mathrm{v}}(E))\nu(\hbar\omega_{\mathbf{k}_0})\Bigg)T^{\mathrm{em}}_{\nu\nu'\mathrm{v}}(r;E) +\Bigg(f_{\mathrm{v}}(E)(1-f_{\mathrm{c}}(E+\hbar\omega_{\mathbf{k}_0}))\nu(\hbar\omega_{\mathbf{k}_0}) -f_{\mathrm{c}}(E+\hbar\omega_{\mathbf{k}_0})(1-f_{\mathrm{v}}(E))(\nu(\hbar\omega_{\mathbf{k}_0})+1)\Bigg)T^{\mathrm{abs}}_{\nu\nu'\mathrm{v}}(r;E)\Bigg], \quad (7.11)$$

where $\nu(E) = (\exp(\beta E)-1)^{-1}$ is the Bose-Einstein distribution function. Note that each of the terms in (7.11) can be interpreted in terms of transitions from the valence to the conduction band – or vice versa – assisted by the emission or absorption of a long-wavelength phonon. Moreover, $J_z(r)$ being dependent only on r is an immediate consequence of the requirement that a stationary current be solenoidal. Finally, the total line tunneling current is obtained by integrating $J_z(r)$ over the wire cross section,

$$I = 2\pi\int_0^R \mathrm{d}r\, r J_z(r) = -\frac{2e}{\hbar}\int\frac{\mathrm{d}E}{2\pi} \times\Bigg[\Bigg(f_{\mathrm{v}}(E)(1-f_{\mathrm{c}}(E-\hbar\omega_{\mathbf{k}_0}))(\nu(\hbar\omega_{\mathbf{k}_0})+1) -f_{\mathrm{c}}(E-\hbar\omega_{\mathbf{k}_0})(1-f_{\mathrm{v}}(E))\nu(\hbar\omega_{\mathbf{k}_0})\Bigg)T^{\mathrm{em}}_{\mathrm{v}}(E) +\Bigg(f_{\mathrm{v}}(E)(1-f_{\mathrm{c}}(E+\hbar\omega_{\mathbf{k}_0}))\nu(\hbar\omega_{\mathbf{k}_0}) -f_{\mathrm{c}}(E+\hbar\omega_{\mathbf{k}_0})(1-f_{\mathrm{v}}(E))(\nu(\hbar\omega_{\mathbf{k}_0})+1)\Bigg)T^{\mathrm{abs}}_{\mathrm{v}}(E)\Bigg]. \quad (7.12)$$

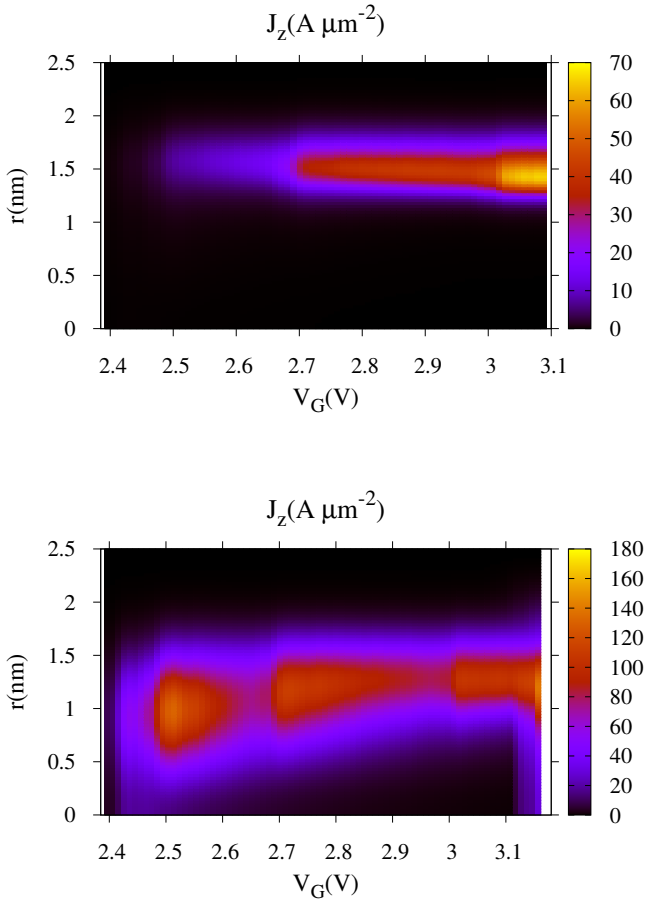

Figure 7.4: Contour plot of the current densities as function of $V_{\rm G}$ and r inside the nanowire TFET. The applied drain voltage is: (a) $V_{\rm ds} = 0.4$ V, and (b) $V_{\rm ds} = 0.6$ V.

7.4 Simulations

In order to study the Zener tunneling current of the device sketched in Fig. 7.1, we considered a silicon nanowire of radius $R = 2.5$ nm and gate length $L_{\rm G} = 20$ nm, operating at room temperature. The six [100] oriented conduction band valleys are characterized by their longitudinal mass $m_l = 0.916m_0$ and transverse mass $m_t = 0.19m_0$, whereas the heavy and light hole valleys of the valence band are taken into account, with respectively masses $m_{hh} = 0.49m_0$ and $m_{lh} = 0.16m_0$. For the simulated results presented for the carrier concentrations, in figures 7.2-7.3 and current below, the following parameters have been used: $E_{\rm g} = 1.12$ eV, $\epsilon_{\rm s} = 11.5\epsilon_0$, $\epsilon_{\rm ox} = 15\epsilon_0$, $t_{\rm ox} = 1$ nm, $\rho_s = 2.328$ g/cm^3.

The acceptor doping concentration, the interband deformation potential and the phonon energy are respectively taken to be $N_{\rm A} = 10^{20}$ cm^{-3}, $D|\mathbf{k}_0| = 2.45 \times 10^8$ eVcm^{-1} and $\hbar\omega_{\mathbf{k}_0} = 18.4$ meV. The 3D carrier concentration profiles computed according to the MLDA are plotted in Fig. 7.2 for $V_{\rm G} = 2.4$ V and $V_{\rm ds} = 0.6$ V. On the one hand, we observe that the mobile holes are located near the center of the wire due to the positive gate voltages. On the other hand, the electron concentration profile forms an n-channel near the semiconductor/oxide interface. In Fig. 7.3, we may also see that the electron concentration is gradually enhanced with increasing gate voltage. In particular, we have observed that for a $V_{\rm G}$ exceeding 2.38 V, a substantial overlap between the hole and electron profiles occurs around $r = 1.1$ nm thereby reflecting the increased BTBT probability. The latter is confirmed by the current density profiles shown in Fig. 7.4, in which the 3D current density $J_z(r)$ calculated from (7.11) is shown as a function of $V_{\rm G}$ and r. An important figure of merit characterizing the line tunneling current is the BTBT onset voltage which reaches a high value of $V_{\rm G} \approx 2.38$ V. This is a direct consequence of the strong carrier confinement which results in relatively high electron subband energies and low hole subband energies. As expected, due to a more pronounced radial quantization, this results in a higher onset voltage, which is determined by the first accessible subbands of electrons and holes, as compared to the case of planar line tunneling structures [9] where the valence band energy spectrum is predominantly continuous. Figs. 7.4((a),(b)) further reveals that the current density significantly increases with increasing gate voltage. In the case of $V_{\rm ds} = 0.4$ V (Fig. 7.4(a)), the current density remains low near the center of the nanowire and at the Si/oxide interface in spite of the high values of $V_{\rm G}$. On the other hand, a significant part of the current density profile is located in the overlap region, roughly between $r = 0.5$ nm and $r = 2$ nm. For larger $V_{\rm ds}$, e.g. for $V_{\rm ds} = 0.6$ V, we may observe a qualitatively similar behavior. However, the current density at the center of the nanowire is found to be larger due to the contribution of the highest occupied subbands of the conduction band valleys.

Finally, figs. 7.5((a),(b)) show the line tunneling current as a function of $V_{\rm G}$ for various values of $V_{\rm ds}$, the nanowire radii being set to $R = 2.5$ nm and $R = 4$ nm, respectively. In case of the thinner wire, the current starts to increase rapidly and saturates when the gate voltage approaches 2.5 V. For thicker wires (see Fig. 7.5(b)), the BTBT onset occurs at a lower onset voltage, $V_{\rm G} \approx 1.17$. This is because the band structure of thick wires is closer to the bulk band structure with a less pronounced confinement effect. Also, the current for different $V_{\rm ds}$ voltages shows various distinct saturation regions, as can be seen from Fig. 7.5(b). Careful inspection of Figs. 7.5((a),(b)) finally reveals that the onset voltage depends on the nanowire radius, i.e. the onset voltage of the thinner nanowire obviously exceeds that of the thicker wire. The reason is that with increasing radial confinement, the energy gap separating the lowest subband level of the conduction band

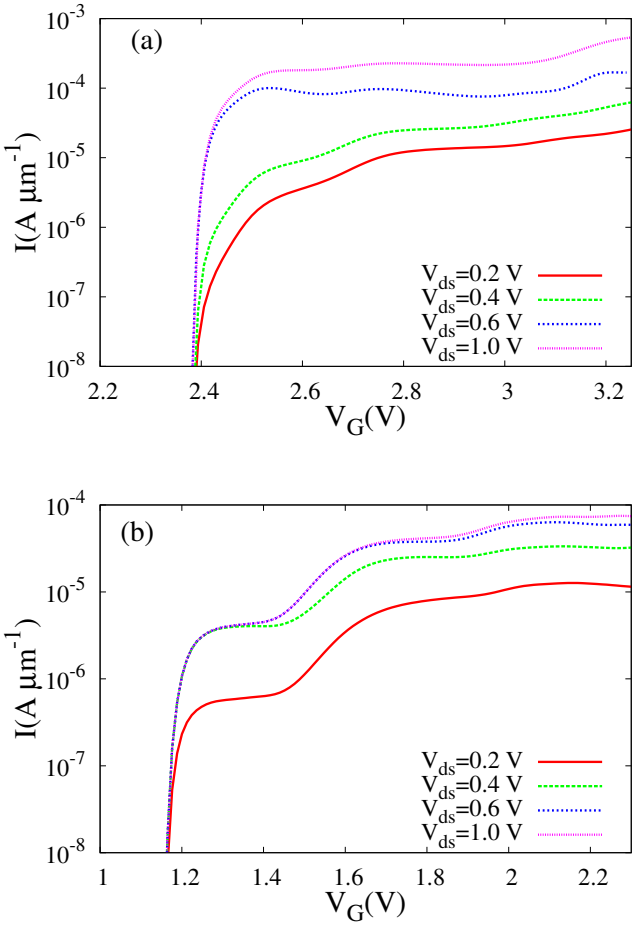

Figure 7.5: Line tunneling current as function of the gate voltage for different $V_{\rm ds}$ in case of a nanowire TFET of radius (a) $R = 2.5$ nm and (b) $R = 4$ nm. The vertical axis represents the tunneling current per unit gate length, as the line tunneling current is proportional to the gate length.

from the highest subband level in the valence band exceeds increases. Therefore, a larger gate voltage is needed in order to make the two levels line up at the point where line tunneling current starts flowing through the wire.

7.5 Conclusion

Having expressed the spectral functions for the valence and conduction bands semi-analytically in the framework of MLDA, we have solved self-consistently

the Schrödinger and Poisson equations by implementing a non-linear variational algorithm for the calculation of the hole and electron concentration in a nanowire TFET. Using the electrostatic potential and the spectral functions, we have extracted the line tunneling probability and the corresponding tunneling current from a formula that expresses the latter perturbatively in terms of the interactions of the electrons and the long-wavelength phonons that mediate BTBT events in an indirect band gap semiconductor. It is found that confinement effects in nanowire TFETS have a stronger impact on the onset voltage of the tunneling current than in the case of planar TFETs. Although the non-linear, MLDA-based variational method was applied to the simple case of a long nanowire, we believe that it can be extended to other devices for which the MLDA is an reasonable approximation.

8

Summary and Outlook

Summary

This PhD thesis addressed the study of the electronic transport properties in cylindrical nanowire devices such as MOSFETs and tunneling field-effect transistors. Our work may be briefly summarized as follows.

In chapter 3, we have presented both the modified local density approximation (MLDA) and non-linear variational method. Also, it was shown how the variational principle can be exploited as a numerical tool for the simultaneous self-consistent solution of the Poisson and Schrödinger equations within the framework of the MLDA. Since the non-linear Poisson equation is solved by minimizing numerically its corresponding action, it was found that our approach accelerates the evaluation of the quantum mechanical charge and current density profiles in the nanodevices studied in this thesis.

In chapter 4, we have proposed a quantum mechanical model for a cylindrical nanowire MOSFET consisting of a simplified Poisson-Schrödinger solver and a module for the current density by invoking the non-linear MLDA-based variational method. The latter has been extended to the 1D ballistic Boltzmann transport equation (BTE) in order to compute the non-equilibrium distribution function for electrons within the framework of the MLDA. The current density and its related current-voltage characteristic have been calculated from the 1D ballistic steady-state BTE which has been solved analytically by using the method of characteristic curves. It is worth to mention that our approach offers a

trade-off between quantum mechanical rigor and computational speed, however, it has the disadvantage of ignoring both reflection and tunneling events.

In chapter 5, the nonparabolic Kane and Poisson equation were solved self-consistently only in the radial direction by implementing the non-linear MLDA-based variational method in case of a very long cylindrical nanowire MOSFET. The nonparabolic coefficients were computed by comparing the analytical solution of Kane's model with the tight-binding calculation of the bandstructure for thin cylindrical nanowires. Once the potential is known, we have obtained the low-field mobility and low-field conductivity, for acoustic phonon and surface roughness (SR) scattering mechanisms, within the framework of the MLDA. Our findings suggest that the low-field mobility deteriorates at high gate voltage and the low-field conductivity exhibits negative transconductance in case of relatively thick wires, i.e. $R \gtrsim 1.5$ nm. Finally, for all nanowire radius considered in this chapter, i.e. $1 \text{ nm} \leqslant R \leqslant 2.5$ nm, it was found that the low-field conductivity is mainly dominated by the SR-limited conductivity.

In chapter 6, the Zener tunneling current flowing through a biased, abrupt $p - n$ junction embedded in a cylindrical silicon nanowire has been calculated. As the band gap becomes indirect for sufficiently thick wires, Zener tunneling and its related transitions between the valence and conduction bands are mediated by short-wavelength phonons interacting with mobile electrons. Therefore, not only the high electric field governing the electrons in the space-charge region but also the transverse acoustic (TA) and transverse optical (TO) phonons have been incorporated in the expression for the tunneling current. The latter is also affected by carrier confinement in the radial direction and therefore we have performed a full self-consistent solution of the Schrödinger and Poisson equations within the effective mass approximation for both conduction and valence band electrons. We have found that the tunneling current exhibits a pronounced dependence on the wire radius, particularly in the high-bias regime. Notice that the non-linear MLDA-based variational method has not been implemented in this chapter.

In chapter 7, the tunneling current was computed for a cylindrical nanowire TFET with an all-round gate that covers the source region. Since the band-to-band tunneling (BTBT) is mediated by electron – phonon interaction, it is affected by carrier confinement in the radial direction and therefore involves the self-consistent solution of the Schrödinger and Poisson equations. The latter has been accomplished by exploiting the non-linear MLDA-based variational method. Then, using the electrostatic potential and the spectral functions, we have expressed the formula for indirect BTBT within the framework of MLDA. As as major conclusion, we have found that the confinement effects in nanowires TFETs have a stronger impact on the onset voltage of the line tunneling current than in case of planar TFETs.

Outlook

A numerical tool to simplify the self-consistent solution to Poisson's and Schrödinger's equations as well as the constitutive equations generally involving the non-equilibrium distribution function, the MLDA-based variational scheme can in the future be refined to incorporate quantum effects on a more sophisticated level. Moreover, its application area is not restricted to conventional CMOS or post-CMOS devices appearing in the last decades of the reign of Moore's law but can be extended to various other devices and structures for which similar self-consistency requirements need to be met. As an illustration, we mention the concept of graphene nanoribbon field-effect transistors.
In order to extend the perspective of Moore's law, strong efforts have been launched for searching new transistor channel materials beyond silicon. For instance, graphene has shown to be a promising candidate for nano-electric applications [71]. However, its metallic properties limits graphene's applications for semiconducting devices. Instead, a recent experiment has demonstrated that all sub-10nm-wide Graphene Nanoribbons (GNRs) are semiconducting [72], which makes them more attractive for electronic device applications. Then, devices such as the GNR field-effect transistor (GNRFET) has been proposed [73, 74]. Numerically, simulation of such a GNRFET can be achieved by self-consistently solving a Weyl-like equation [75] for electrons in the GNR, coupled to a three dimensional Poisson equation. Therefore, we could implement the non-linear MLDA-based variational method in order to obtain a self-consistent solution of the coupled Poisson Dirac-Weyl equation. Choosing a zigzag nanoribbon to be infinite in the x direction, it is well-known, that the spinor wave function can be written as

$$\psi(x,y) = \frac{\mathrm{e}^{ik_x x}}{\sqrt{2\pi L_x}}\,\Phi(y), \quad \Phi(y) = \begin{pmatrix} \phi_{\mathrm{A}}(y) \\ \phi_{\mathrm{B}}(y) \end{pmatrix} \tag{8.1}$$

with eigenenergies $E_n(k_x) = \hbar v_F \sqrt{k_x^2 - \kappa_n^2}$, with n = 1, 2, ... The values of κ_n, around the Dirac point $\mathbf{K}$, can be obtained from the eigenvalue equation

$$\mathrm{e}^{2\kappa_n L_y} = \frac{k_x - \kappa_n}{k_x + \kappa_n}, \tag{8.2}$$

for surface edge states, whereas the solutions of

$$k_x = \frac{k_n}{\tan(k_n L_y)} \tag{8.3}$$

correspond to bound states with $\kappa_n = ik_n$. The eigenvalue equations for the inequivalent Dirac point $\mathbf{K}'$ are obtained by inversion, i.e. $k_x \to -k_x$. Within

the framework of the MLDA, the one-electron LDOS can be written as

$$A_{\mathrm{c}}(x,y,z;E) = \frac{1}{\pi}\sum_{n}|\Phi_n(y)|^2\left[\frac{(E+eV(x,y,z))^2+\kappa_n^2}{\hbar^2 v_F^2}\right]^{-\frac{1}{2}}, \tag{8.4}$$

and accordingly, the electron concentration, in equilibrium, inside the GNRFET is expressed as

$$\begin{aligned} n_{\mathrm{c}}[y,V(x,y,z)] &= 2\int \mathrm{d}E A_{\mathrm{c}}(x,y,z;E)F(E,E_{\mathrm{F}}) \\ &= \frac{2\hbar v_F}{\pi}\sum_{n}|\Phi_n(y)|^2\int_{-\infty}^{\infty}\mathrm{d}k_x\, k_x F(E_n(k_x)-eV(x,y,z),E_{\mathrm{F}}). \end{aligned} \tag{8.5}$$

Expressions for the concentration of electrons in the valence band and in case of an arm-chair GNR can be obtained analogously. From equation (9.5), we may infer that the total charge density is a local functional of the potential $V(x,y,z)$. Therefore the variational principle explained in chapter 3 could be implemented to solve self-consistently the Weyl-like and the three dimensional Poisson equation.

Maxwell's equations for 3D structures

In spite of its promising perspective, the non-linear MLDA-based variational method described in this PhD thesis as well as its implementation in numerical programs suffers from two major restrictions: 1) it has been formulated and worked out only for electrostatic fields governed merely by Poisson's equation, and 2) it heavily relies on the MLDA which is the key feature allowing for the introduction of self-consistency through the charge density which forcefully takes the form of a strictly local functional of the potential $V(\mathbf{r})$. In this light, we see two possible extensions of the present formalism. First, numerous applications related to carrier transport in semiconductors interacting with electromagnetic field in the ultra-high frequency range, only requires classical transport theory which remains compatible with the MLDA, whereas the real challenge is in writing proper numerical code that is capable of solving Maxwell's equations for 3D structures in the high-frequency range. Numerical code being developed to this end may therefore greatly benefit from an extended variational principle built on

the full electromagnetic action discussed in chapter 3, i.e.

$$S[V,\mathbf{A}] = \int_\Omega \mathrm{d}^3 r \left(\frac{1}{2}\epsilon \left|\nabla V(\mathbf{r})\right|^2 - \frac{1}{2}\epsilon \left|\nabla \times \mathbf{A}(\mathbf{r})\right|^2 - \int_{V_0}^{V(\mathbf{r})} \mathrm{d}V' \rho[V'] - \int_{\mathbf{A}_0}^{\mathbf{A}(\mathbf{r})} \mathrm{d}\mathbf{A}' \cdot \mathbf{J}[V,\mathbf{A}'] \right) \tag{8.6}$$

such that $\delta S[V,\mathbf{A}] = 0$ would analogously give rise to the four Maxwell's equations self-consistently coupled to the (classical) kinetic and constitutive equations. Secondly, a less straightforward approach could be envisaged in order to abandon the MLDA-related restriction while keeping focus on static fields, as would be required when a fully quantum mechanical treatment of transport becomes inevitable. Since the non-local dependence of the constitutive equations is pronouncedly present in the carrier wave functions, though in a very implicit way, an alternative and more transparent route may be provided by the formalism of path integrals.

9
Nederlandse samenvatting

Samenvatting

Dit proefschrift behandelt de elektronische transporteigenschappen van ladingdragers in componenten die bestaan uit cilindrische nanodraden, zoals MOSFET's en tunneling veld-effecttransistoren.
Het werk kan als volgt worden samengevat.

In hoofdstuk 3 hebben we de gemodificeerde lokale dichtheidsbenadering ("modified local density approach", afgekort tot MLDA) geïntroduceerd en in verband gebracht met niet-lineaire variatierekening. Meer bepaald hebben we aangegeven hoe het variatieprincipe kan worden benut als een numeriek model voor een simultane, zelfconsistente oplossing van de Poisson- en Schrödingervergelijkingen in het kader van de MLDA. Doordat de resulterende, niet-lineaire Poissonvergelijking wordt opgelost door de bijbehorende actiefunctionaal te minimaliseren, konden we aantonen dat onze aanpak de berekening van de kwantummechanische lading- en stroomdichtheidprofielen versnelt voor de nanodevices die in dit proefschrift zijn bestudeerd.

In hoofdstuk 4 hebben we een kwantummechanisch model opgesteld voor een cilindrische nanodraadMOSFET. Het model bestaat uit een vereenvoudigde Poisson-Schrödinger solver en een module ter berekening van de stroomdichtheid, beide gebaseerd op de MLDA-gerelateerde variatierekening. Deze laatste is, bij wijze van werkvoorbeeld, uitgebreid tot de 1D ballistische Boltzmann transportvergelijking waarbij ook niet-evenwichtsdistributiefuncties voor elek-

tronen kunnen worden uitgerekend. De stroomdichtheid en de bijbehorende stroom-spanningskarakteristiek die overeenkomen met de 1D ballistische stationaire toestand konden worden berekend door de ballistische Boltzmann transportvergelijking in de stationaire limiet analytisch op te lossen d.m.v. de methode van de karakteristieke krommen. Vermeldenswaard is dat deze aanpak een goed compromis biedt tussen kwantummechanische gestrengheid en rekensnelheid, wat weliswaar niet wegneemt dat kwantummechanische reflecties (aan barrières) en tunneling niet in rekening worden gebracht.

Hoofdstuk 5 behandelt de implementatie van de niet-parabolische bandstructuur, i.h.b het Kane-model, in de MLD-gerelateerde niet-lineaire variatierekening. Hierbij worden het Kane-model en de Poissonvergelijking zelf-consistent opgelost in radiale richting door uit te gaan van een zeer lange cilindrische nanodraadMOSFET. De parameters die de afwijking van de parabolische banden weergeven worden bepaald door de modelberekening te vergelijken met de resultaten van een tight-binding berekening van de bandstructuur voor dunne cilindrische nanodraden. Als de potentiaal eenmaal bekend is, kunnen de elektronenmobiliteit en -conductiviteit bij lage velden worden berekend in het kader van de MLDA, met inachtname van verstrooiing teweeggebracht door akoestische fononen en oppervlakteruwheid ("surface rougness"). De resultaten suggereren dat de lage-veld mobiliteit bij hoge gate-spanningen afneemt terwijl de lage-veld geleidbaarheid negatieve transconductantie vertoont in het geval van relatief dikke draden, dwz $R \gtrsim 1.5$ nm. Tenslotte werd vastgesteld dat, voor alle nanodraden behandeld in dit hoofdtuk (d.i. met een straal die varieert tussen 1 nm en 2.5 nm), de lage-veld geleidbaarheid dominant laag gehouden wordt door oppervlakteruwheid.

In hoofdstuk 6 hebben we de stroom uitgerekend die als gevolg van Zener-tunneling door een abrupte $p - n$-junctie loopt, die ingebed is in een cilindrische silicium nanodraad. Omdat de bandgap indirect wordt voor voldoende dikke draden, kunnen Zener-tunneling en de bijbehorende overgangen tussen de valentie- en conductiebanden alleen plaats vinden door de interactie van beweeglijke elektronen en fononen met korte golflengtes. Daarom hebben we in de theoretische beschrijving niet alleen de elektrische velden in de ruimteladingslagen, maar ook de transversaal akoestische (TA) en transversaal optische (TO) fononen meegenomen in de uitdrukking voor de tunnelstroom. Die laatste wordt vanzelfsprekend ook significant beïnvloed door de ruimtelijke opsluiting ("confinement") van de ladingdragers in de radiale richting zodat een volledig zelfconsistente oplossing van de Schrödinger- en Poissonvergelijking (in de effectieve massabenadering) noodzakelijk is voor zowel de conductie- als de valentieband. We hebben afgeleid dat de tunnelstroom een uitgesproken afhankelijkheid van de straal van de nanodraad vertoont, in het bijzonder als de aangelegde spanning hoog is. De methode van de niet-lineaire, MLDA-gerelateerde

variatierekening is niet toegepast in dit hoofdstuk.

Hoofdstuk 7 behandelt de tunnelstroom in een cilindrische nanodraad tunnelFET (TFET) met een allround gate die het hele brongebied omvat. Omdat enerzijds band-to-band tunneling (BTBT) in structuren met een indirecte bandgap geïnitieerd wordt door elektron-fononinteractie, maar anderzijds ook hier de ruimtelijke opsluiting van de elektronen in de radiale richting een cruciale rol speelt, zijn de Schrödinger- en de Poissonvergelijking zelfconsistent opgelost, en wel via de MLDA-aanpak. In deze context werden ook de spectraalfuncties uitgerekend die samen met de elektrostatische potentiaal voorkomen in de uitdrukking voor de BTBT-transmissiecoëfficiënt, die werd afgeleid d.m.v. de MLDA-methode. Als belangrijkste conclusie tekenen we op dat bij TFET's die gefabriceerd zijn op basis van silicium nanodraden confinement een veel grotere impact heeft op de spanning die de aanzet van de tunnelstroom t.g.v. line tunneling markeert, dan bij planaire TFET's.

Vooruitzicht

Oorspronkelijk bedoeld als een numeriek algoritme ter vereenvoudiging van de zelf-consistente oplossing van de Poisson- en de Schrödingervergelijking evenals de constitutieve vergelijkingen die de expliciete distributiefunctie voor niet-evenwicht bevatten, kan de niet-lineaire, MLDA-gerelateerde variatierekening in de toekomst worden verfijnd om kwantumeffecten op een meer rigoureuze manier in rekening te brengen. Bovendien is het toepassingsgebied niet beperkt tot conventionele CMOS- of post-CMOS-componenten die zich aandienen in de eindfase van de wet van Moore, maar kan het worden uitgebreid tot talloze devices en structuren waarbij vergelijkbare zelfconsistentie-eisen worden gesteld. Ter illustratie vermelden we het concept van de veldeffectransistor gebaseerd op grafeen nanoribbons.

Teneinde het perspectief van de wet van Moore alsnog te bestendigen, wordt er vandaag intensief gezocht naar naar nieuwe materialen die silicium als basismateriaal voor transistorkanalen kunnen vervangen. In dit opzicht lijkt grafeen een veelbelovende kandidaat voor nano-elektronische toepassingen [71]. Alleen zijn de metallische eigenschappen van grafeen problematisch voor de realisatie van typische halfgeleiderapplicaties. Anderzijds heeft een recent experiment aangetoond dat alle sub-10nm-brede grafeen nanoribbons (GNRs) halfgeleidend zijn [72], waardoor ze enig perspectief bieden voor elektronische toepassingen zoals bijvoorbeeld de GNR veldeffecttransistor (GNRFET) [73, 74]. De numerieke simulatie van een dergelijke GNRFET vereist de zelfconsistente oplossing van een soort Weyl-vergelijking [75] voor elektronen in de GNR en een driedimensionale Poissonvergelijking. Voor dergelijke zelfconsistente oplossing kunnen

we in principe voordeel halen uit de combinatie van de MLDA en niet-lineaire variatierekening. De spinorgolffunctie voor een elektron in een zigzag nanoribbon die oneindig ver doorloopt in de x-richting, kan geschreven worden als

$$\psi(x,y) = \frac{\mathrm{e}^{ik_x x}}{\sqrt{2\pi L_x}}\,\Phi(y), \quad \Phi(y) = \begin{pmatrix}\phi_{\mathrm{A}}(y)\\ \phi_{\mathrm{B}}(y)\end{pmatrix} \tag{9.1}$$

met als eigenenergieën $E_n(k_x) = \hbar v_F\sqrt{k_x^2 - \kappa_n^2}$, waarbij n = 1, 2, ... De waarden van κ_n, die overeenkomen met Dirac-punt $\mathbf{K}$, volgen uit de oplossing van de eigenwaardenvergelijking

$$\mathrm{e}^{2\kappa_n L_y} = \frac{k_x - \kappa_n}{k_x + \kappa_n}, \tag{9.2}$$

voor oppervlaktetoestanden bij de rand en

$$k_x = \frac{k_n}{\tan(k_n L_y)} \tag{9.3}$$

voor gebonden toestanden met $\kappa_n = ik_n$. De eigenwaardenvergelijkingen die horen bij het niet-equivalente Dirac punt $\mathbf{K}'$ worden verkregen door inversie, d.i. $k_x \to -k_x$. In het kader van de MLDA, kan de lokale elektronentoestandsdichtheid ("local density of state – LDOS") worden geschreven als

$$A_{\mathrm{c}}(x,y,z;E) = \frac{1}{\pi}\sum_n |\Phi_n(y)|^2 \left[\frac{(E + eV(x,y,z))^2 + \kappa_n^2}{\hbar^2 v_F^2}\right]^{-\frac{1}{2}}, \tag{9.4}$$

zodat de elektronenconcentratie voor een GNRFET in evenwicht volgt uit

$$\begin{aligned} n_{\mathrm{c}}[y, V(x,y,z)] &= 2\int \mathrm{d}E A_{\mathrm{c}}(x,y,z;E) F(E, E_{\mathrm{F}}) \\ &= \frac{2\hbar v_F}{\pi}\sum_n |\Phi_n(y)|^2 \int_{-\infty}^{\infty} \mathrm{d}k_x\, k_x F(E_n(k_x) - eV(x,y,z), E_{\mathrm{F}}). \end{aligned} \tag{9.5}$$

Uitdrukkingen voor de concentratie van elektronen in de valentieband en bij een "armchair" GNR kunnen op analoge wijze worden verkregen. Uit vergelijking (9.5) kunnen we afleiden dat de totale ladingsdichtheid een lokale functionaal is van de potentiaal $V(x,y,z)$ wat ons in staat stelt om het variatieprincipe toegelicht in hoofdstuk 3 opnieuw te benutten om nu de Dirac-Weyl- en de driedimensionale Poissonvergelijking zelf-consistent op te lossen.

Maxwell's equations for 3D structures

Ondanks het veelbelovende perspectief van de niet-lineaire MLDA op basis van variatierekening, zoals beschreven en toegepast in dit proefschrift, zijn er twee grote beperkingen: 1) de huidige formulering is uitsluitend uitgewerkt voor elektrostatische velden die voldoen aan de Poissonvergelijking, en 2) ze is gedomineerd door de MLDA die de implementatie van de zelf-consistentie beperkt tot de gevallen waarin de ladingsdichtheid een strikt lokale functionaal is van de potentiaal $V(\mathbf{r})$. In die context denken we aan twee mogelijke uitbreidingen van de huidige formalisme.

Allereerst is er een groot aantal toepassingen in het hoogfrequente gebied waarbij het transport van elektronen en gaten op voldoende accurate manier kan worden beschreven door klassieke kinetische vergelijkingen die compatibel blijven met de MLDA, terwijl de numerieke knelpunten veeleer gesitueerd zijn in de oplossing van de Maxwellvergelijkingen voor 3D structuren en hoge frequenties. Numerieke code ontwikkeld om dit doel te bereiken kan dan ook veel baat hebben bij een gelijkaardig variatieprincipe dat het volledige elektromagnetische veld behelst, zoals aangehaald in in hoofdstuk 3 en met een actiefunctionaal gegeven door

$$S[V,\mathbf{A}] = \int_\Omega \mathrm{d}^3 r \left(\frac{1}{2}\epsilon \left|\nabla V(\mathbf{r})\right|^2 - \frac{1}{2}\epsilon \left|\nabla \times \mathbf{A}(\mathbf{r})\right|^2 - \int_{V_0}^{V(\mathbf{r})} \mathrm{d}V' \rho[V'] - \int_{\mathbf{A}_0}^{\mathbf{A}(\mathbf{r})} \mathrm{d}\mathbf{A}' \cdot \mathbf{J}[V,\mathbf{A}'] \right) \tag{9.6}$$

zodat $\delta S[V,\mathbf{A}] = 0$ op analoge wijze als voor de Poisson-vergelijking zou leiden tot de vier Maxwellvergelijkingen en hun zelfconsistente koppeling met de (klassieke) kinetische en constitutieve vergelijkingen. Een tweede uitbreiding zou erin kunnen bestaan de rechttoe-rechtaan benadering via de MLDA op te geven wanneer een volledig kwantummechanische behandeling van de transportkarakteristieken niet langer valt te vermijden, weliswaar met beperking tot statische velden. Aangezien de constitutieve vergelijkingen in dat geval geen lokale of expliciete functionalen van de potentiaal meer bevatten, zou men kunnen overwegen om de afhankelijkheid van de potentiaal in een gegeneraliseerde MLDA op transparante wijze te implementeren via padintegralen.

A

Electron distribution: ballistic Boltzmann transport equation

Consider a generic 1D device along the z-direction with an active region sandwiched between two contact regions, through which identical particles with mass m are moving. Neglecting all collisions, we need to solve the 1D BTE

$$\frac{\partial f(z,p,t)}{\partial t} + \frac{p}{m}\frac{\partial f(z,p,t)}{\partial z} - \frac{\partial U(z)}{\partial z}\frac{\partial f(z,p,t)}{\partial p} = 0 \tag{A.1}$$

in order to extract the ballistic distribution function $f(z,p,t)$. In previous works it was observed that the method of the characteristic curves (MCC) – also referred to as the Lagrange-Charpit method – described in Refs. [14, 15, 76], can be employed in the framework of the Boltzmann equation. Below, we give a brief description of how the MCC may be implemented in our particular model without addressing the details of the method. Assuming that we know the classical trajectories $Z(s), P(s)$ in the "past", i. e. for times s in the interval $-t \leq s \leq 0$ and with the initial conditions $Z(0) = z$, $P(0) = p$, the solution of Eq. (A.1) at an arbitrary time $t > 0$ is completely specified provided that the initial distribution function $f_0(z,p)$ is known as well, yielding $f(z,p,t) = f_0(Z(-t), P(-t))$. In what follows, we assume that $f_0(z,p)$ is the equilibrium Fermi-Dirac distribution, $F(E, E_\mathrm{F}) = [1 + \exp\big(\beta(E - E_\mathrm{F})\big)]^{-1}$ where $\beta = 1/k_\mathrm{F}T$ and E_F denotes the equilibrium Fermi energy (or chemical potential). A full time-dependent analysis of the distribution function would require a numerical computation.

On the other hand, the steady-state limit of the ballistic distribution function $f_{\mathrm{B}}(z,p) = \lim_{t\to\infty} f(z,p,t)$ obeying

$$\frac{p}{m}\frac{\partial f_{\mathrm{B}}(z,p)}{\partial z} - \frac{\partial U(z)}{\partial z}\frac{\partial f_{\mathrm{B}}(z,p)}{\partial p} = 0, \tag{A.2}$$

can be calculated analytically by considering the properties of the classical paths in the infinite past, i.e. $Z(-\infty)$ and $P(-\infty)$. However, there is a limitation: the potential energy profile $U(z)$ characterizing the final steady-state should: (i) become flat far away from the active region, $\lim_{z\to-\infty} U(z) = 0, \quad \lim_{z\to\infty} U(z) = -eV_{\mathrm{ds}}$ and (ii) reach a single, unique maximum U_{M} for $z = z_{\mathrm{M}}$, i.e. $U_{\mathrm{M}} = U(z_{\mathrm{M}})$ where z_{M} is located inside the active region. This limitation is compatible with the architecture of most MOSFET channels. Next, we combine the observation that, depending on the initial conditions $Z(0) = z, P(0) = p$, $Z(-\infty)$ will asymptotically tend to $\pm\infty$ where the potential is flat, with the principle of energy conservation to obtain $P(-\infty)$ from

$$P^2(-\infty) = p^2 + \sqrt{2m\big(U(z) - U(Z(-\infty))\big)}. \tag{A.3}$$

As U_{M} represents an absolute maximum, i.e. $U_{\mathrm{M}} \geqslant U(z)$ for all z, we can defined a unique "critical momentum function" $p_{\mathrm{M}}(z) = \sqrt{2m\big(U_{\mathrm{M}} - U(z)\big)}$, which determines how the particles can occupy the states in their parabolic kinetic energy band, following a procedure similar to that of Ref. [35].

States above U_{M}.

- $p \geqslant p_{\mathrm{M}}(z)$:
  Particles injected from the left contact have enough energy to overcome with the potential barrier. As a result they keep moving to the right contact:

$$\begin{aligned} f_{\mathrm{B}}(z,p) &= f_0\left(-\infty, \sqrt{p^2 + 2mU(z)}\right) \\ &= F\left(\frac{p^2}{2m} + U(z), E_{\mathrm{F}}\right). \end{aligned} \tag{A.4}$$

- $p \leqslant -p_{\mathrm{M}}(z)$:
  Analogously, particles injected from the right contact move to the left:

$$\begin{aligned} f_{\mathrm{B}}(z,p) &= f_0\left(\infty, -\sqrt{p^2 + 2m\big(U(z) + eV_{\mathrm{ds}}\big)}\right) \\ &= F\left(\frac{p^2}{2m} + U(z) + eV_{\mathrm{ds}}, E_{\mathrm{F}}\right) \\ &= F\left(\frac{p^2}{2m} + U(z), E_{\mathrm{F}} - eV_{\mathrm{ds}}\right). \end{aligned} \tag{A.5}$$

States below U_{M}, $|p| \leqslant p_{\mathrm{M}}(z)$.

Particles injected from both the left and the right contacts having energies lower than U_{M} will hit the potential barrier and get reflected. We consider the following two cases:

- $z \leqslant z_{\mathrm{M}}$:
  Particles coming from the left, with $p \geqslant 0$ hit the barrier and are reflected back while changing the sign of their momentum:

$$\begin{aligned} f_{\mathrm{B}}(z,p) &= f_0\left(\infty, \sqrt{p^2 + 2mU(z)}\right) \\ &= F\left(\frac{p^2}{2m} + U(z, E_{\mathrm{F}})\right). \end{aligned} \tag{A.6}$$

- $z \geqslant z_{\mathrm{M}}$:
  Particles leaving the right contact can be treated in complete anology, leading to:

$$\begin{aligned} f_{\mathrm{B}}(z,p) &= f_0\left(\infty, -\sqrt{p^2 + 2m\left(U(z) + eV_{\mathrm{ds}}\right)}\right) \\ &= F\left(\frac{p^2}{2m} + U(z) + eV_{\mathrm{ds}}, E_{\mathrm{F}}\right) \\ &= F\left(\frac{p^2}{2m} + U(z), E_{\mathrm{F}} - eV_{\mathrm{ds}}\right). \end{aligned} \tag{A.7}$$

Equivalently, the complete solution can now be summarized as follows:

- For $z \leqslant z_{\mathrm{M}}$,

$$f_{\mathrm{B}}(z,p) = \begin{cases} F(E, E_{\mathrm{F}}) & \text{if } p \geqslant -p_{\mathrm{M}}(z) \\ F(E, E_{\mathrm{F}} - eV_{\mathrm{ds}}) & \text{if } p \leqslant -p_{\mathrm{M}}(z). \end{cases} \tag{A.8}$$

- For $z \geqslant z_{\mathrm{M}}$,

$$f_{\mathrm{B}}(z,p) = \begin{cases} F(E, E_{\mathrm{F}}) & \text{if } p \geqslant p_{\mathrm{M}}(z) \\ F(E, E_{\mathrm{F}} - eV_{\mathrm{ds}}) & \text{if } p \leqslant p_{\mathrm{M}}(z), \end{cases} \tag{A.9}$$

where an unambiguous definition of the chemical potential needs not be imposed as a boundary condition but naturally emerges from the dynamics of the BTE. The above procedure treating 1D devices can be extended straightforwardly to a 3D device provided the topology of the 3D potential profile in the

longitudinal direction is preserved for every value of the transverse coordinates. In the case of a cylindrical wire, the extension amounts to the replacements $U(z) \rightarrow U_e(r,z), U_{\rm M}(z) \rightarrow U_{\rm M}(r,z), z_{\rm M} \rightarrow z_{\rm M}(r)$ and $p_{\rm M}(z) \rightarrow p_{\rm M}(r,z)$ while, in addition, the set of equations (A.8)-(A.9) is to be invoked with r as a fixed parameter and the inequality $U_{\rm M}(r) \geqslant U_e(r,z)$ is assumed to hold for all r.

References

[1] G. E. Moore *Electronics*, vol. 38, 1965.

[2] R. Myslewski, *PCs and Chips*, ch. Intel's TriGate gamble: It's now or never. 9thMay 2011.

[3] D. K. Ferry *Science*, vol. 319, p. 579, 2008.

[4] Y. Wang, V. Schmidt, S. Senz, and U. Gösele *Nature Nanotechnology*, vol. 1, p. 186, 2006.

[5] B. Tian, X. Zheng, T. J. Kempa, Y. Fang, N. Yu, G. Yu, J. Huang, and C. M. Lieber *Nature*, vol. 449, p. 885, 2007.

[6] L. Hu and G. Chen *Nano. Lett.*, vol. 7, p. 3249, 2007.

[7] A. M. Ionescu and H. Reil *Nature*, vol. 479, p. 329, 2011.

[8] J. Knoch and J. Appenzeller *Digest Device Res. Conf.*, p. 153, 2006.

[9] W. G. Vanderberghe, B. Sorée, W. Magnus, G. Groeseneken, and M. V. Fischetti *App. Phys. Lett.*, vol. 98, pp. 143503–143505, 2011.

[10] W. G. Vanderberghe, B. Sorée, W. Magnus, and M. V. Fischetti *J. App. Phys.*, vol. 109, p. 124503, 2011.

[11] G. Paasch and H. Übensee *Phys. Status Solidi B*, vol. 113, p. 165, 1982.

[12] K. H. Cho, K. H. Yeo, Y. Y. Yeoh, S. D. Suk, M. Li, J. M. Lee, M.-S. Kim, D. W. Kim, D. Park, B. H. Hong, Y. C. Jung, and S. W. Hwang *App. Phys. Lett.*, vol. 92, p. 052102, 2008.

[13] M. J Cáceres, J. A. Carrillo, and T. Goudon *Commun. PDE*, vol. 28, p. 969, 2003.

[14] M. J Cáceres, J. A. Carrillo, I. Gamba, A. Majorana, and C. W. Shu *J. Comput. Electron.*, vol. 5, p. 471, 2006.

[15] F. Brosens and W. Magnus *Phys. Status Solidi B*, vol. 246, p. 1656, 2009.

[16] S. Datta *Superlattices and Microstructures*, vol. 28, p. 253, 2000.

[17] S. Datta, *Electronic transport in Mesoscopic Systems*. Cambridge, UK: Cambrigde University Press, 1997.

[18] M. P. L. Sancho, J. L. Sancho, and J. Rubio *J. Phys. F: Met. Phys.*, vol. 15, p. 851, 1985.

[19] C. M. V. Vliet and A. Barrios *Physica A*, vol. 315, p. 493, 2002.

[20] C. M. V. Vliet, *Equilibrium and Non-equilibrium Statistical Mechanics*. World Scientific, London, Singapore, 2 ed., 2010.

[21] J. D. Jackson, *Classical Electrodynamics*. Addison Wesley Publishing Company, New York, USA, 2 ed., 2005.

[22] W. Magnus and W. Schoenmaker, *Introduction to Electromagnetism*. Elsevier North Holland, Amsterdam, The Netherlands, 1 ed., 2005.

[23] C. Y. Lee and C. K. Kim *IEEE Trans. Electron Devices*, vol. 44, p. 1507, 1997.

[24] P. Hohemberg and W. Kohn *Phys. Rev.*, vol. 136, p. B864, 1964.

[25] J. M. Ziman, *Principles of the Theorie of Solids*. Cambridge Unibersity Press, United Kindong, 1 ed., 1972.

[26] V. L. Bonch-Bruevich and S. Kalashnikov, *Fizika poluprovodnikov*. Nauka, Moscow, 1 ed., 1977.

[27] W. Kohn and L. Sham *Phys. Rev.*, vol. 140, p. A1133, 1965.

[28] K.-H. Schwarz *Phys. Rev. B*, vol. 5, p. 2466, 1972.

[29] L. Hedin and B. Lundqvist *J. Phys. C: Solid State Phys.*, vol. 4, p. 2064, 1971.

[30] J. P. Perdew and A. Zunger *Phys. Rev. B*, vol. 23, p. 5048, 1981.

[31] A. L. Fetter and J. Walecka, *Quantum Theory of Many-Particle Systems*. Dover Books on Physics, USA, 1 ed., 1971.

[32] T. Ando, A. Fowler, and F. Stern *Rev. Mod. Phys.*, vol. 54, p. 437, 1982.

[33] K. Tarnay *Physica scripta*, vol. 24, p. 446, 1981.

[34] F. Stern *Phys. Rev B*, vol. 5, p. 4891, 1972.

[35] J. H. Rhew, Z. Ren, and M. Lundstrom *Solid-state Electron.*, vol. 46, p. 1899, 2002.

[36] W. Frensley *Rev. Mod. Phys.*, vol. 62, p. 745, 1990.

[37] M. D. Croitoro, V. N. Gladilin, V. M. Fomin, J. T. Devreese, W. Magnus, W. Schoenmaker, and B. Sorée *J. Appl. Phys.*, vol. 96, p. 2305, 1990.

[38] S. Barraud *J. Appl. Phys.*, vol. 106, p. 063714, 2009.

[39] M. V. Fischetti *Phys. Rev. B*, vol. 59, p. 4901, 1990.

[40] F. Castella *J. Stat. Phys.*, vol. 104, p. 387, 2001.

[41] J. Wang, E. Polizzi, and M. Lundstrom *J. Appl. Phys.*, vol. 96, p. 2192, 2004.

[42] S. N. Balaban, E. P. Pokatilov, V. M. Fomin, V. N. Gladilin, J. T. Devreese, W. Magnus, W. Schoenmaker, M. V. Rossum, and B. Sorée *Solid-state Electron.*, vol. 46, p. 435, 2002.

[43] L. J. Lauhon, M. S. Gudiksen, D. W. Wang, and C. M. Lieber *Nature (London)*, vol. 420, p. 57, 2002.

[44] W. H. Press, B. P. Flannery, S. A. Teukolsky, and W. T. Vetterling, *Numerical Recipes in Fortran 77: The art of Scientific Computing*. Cambrigde University Press, Cambridge, UK, 1992.

[45] A detail discussion of possible factors which can cause increments of the current in the saturation region in ultra-thin MOSFET may be found in Refs. 1 and 10.

[46] J. R. Barker and Murray *Phys. Lett.*, vol. 93A, p. 271, 1983.

[47] M. Luisier, A. Schenk, W. Fichtner, and G. Klimeck *Phys. Rev. B*, vol. 74, p. 205323, 2006.

[48] S. Jin, M. V. Fischetti, and T. W. Tang *J. Appl. Phys.*, vol. 102, p. 083715, 2007.

[49] A. Esposito, M. Luisier, M. Frey, and A. Schenk *Solid-State Electron.*, vol. 53, p. 376, 2009.

[50] J. A. Lopez-Villanueva, F. Gámiz, I. Melchor, and J. A. Jiménez-Tejada *J. Appl. Phys.*, vol. 75, p. 4267, 1994.

[51] A. Godoy, Z. Yang, U. Ravaioli, and F. Gámiz *J. Appl. Phys.*, vol. 98, p. 013702, 2005.

[52] H. Tanimoto, N. Yasuda, K. Taniguchi, and C. Hamaguchi *Jnp. J. Appl. Phys.*, vol. 4, p. 563, 1988.

[53] R. Kotlyar, B. Obradovic, P. Magtagne, M. Stettler, and M. Giles *App. Phys. Lett.*, vol. 84, p. 5270, 2004.

[54] Y. Lee, K. Kakushima, K. Natori, and H. Iwai *J. App. Phys.*, vol. 109, p. 113712, 2011.

[55] M. V. Fischetti and S. Laux *Phys. Rev. B*, vol. 48, p. 2244, 1993.

[56] S. Banerjee, W. Richardson, J. Coleman, and A. Chatterjee *IEEE Electron Device Lett.*, vol. EDL-8, p. 347, 1987.

[57] J. Appenzeller, Y. Lin, Z. Chen, and P. Avouris *IEEE Trans. Electron Devices*, vol. 52, p. 2568, 2005.

[58] A. S. Verhulst, W. G. Vandenberghe. K. Maex, and G. Groeseneken *Appl. Phys. Lett.*, vol. 91, p. 053102, 2007.

[59] M. Luisier and G. Klimeck *IEEE Electron Device Lett.*, vol. 30, p. 602, 2009.

[60] S. H. Kim, S. Agarwal, Z. A. Jacobson, P. Matheu, C. Hu, and T. K. Liu *IEEE Electron Device Lett.*, vol. 31, p. 1107, 2010.

[61] B. Sorée, W. Magnus, and W. Schoenmaker *Phys. Rev. B*, vol. 66, p. 035318, 2002.

[62] C. Rivas, R. Lake, G. Klimeck, W. R. Frensley, M. V. Fischetti, P. E. Thompson, S. Rommel, and P. Berger *Appl. Phys. Lett.*, vol. 78, p. 814, 2001.

[63] H. Carrillo-Nuñez, W. Magnus, and F. M. Peeters *J. App. Phys.*, vol. 108, p. 063708, 2010.

[64] K. W. Adu, H. Gutiérrez, U. J. Kim, G. Sumanasekera, and P. Eklund *Nano Lett.*, vol. 5, p. 409, 2005.

[65] E. O. Kane *J. Phys. and Chem. of Solids*, vol. 12, p. 181, 1959.

[66] E. O. Kane *J. Appl. Phys.*, vol. 32, p. 83, 1961.

[67] N. Neophytou, P. Abhijeet, M. Lundstrom, and G. Klimeck *IEEE Trans. Electron Devices*, vol. 55, no. 6, p. 1286, 2008.

[68] S. K. Banerjee, W. Richadrson, J. Coleman, and A. Chatterjee vol. 8, pp. 347–349, 1987.

[69] A. S. Verhulst, B. Sorée, D. Leonelli, W. G. Vanderberghe, and G. Groeseneken *J. App. Phys.*, vol. 107, pp. 024518–024526, 2010.

[70] B. Sorée, W. Magnus, and W. Schoenmaker *Phys. Rev. B*, vol. 66, p. 035318, 2002.

[71] C. Berger, Z. Song, X. Li, X. Wu, N. Brown, C. Naud, D. Mayou, T. Li, J. Hass, A. N. Marchenkov, E. H. Conrad, P. N. First, and W. A. de Heer *Science*, vol. 312, p. 1191, 2006.

[72] X. Li, X. Wang, L. Zhang, S. Lee, and H. Dai *Science*, vol. 319, p. 1229, 2008.

[73] P. Zhao and J. Guo *J. App. Phys.*, vol. 105, p. 034503, 2009.

[74] G. Flori and G. Iannaccone *IEEE Elec. Dev. Lett.*, vol. 28, p. 760, 2007.

[75] H. Weyl *Zeitschrift für Physik*, vol. 56, p. 330, 1929.

[76] B. J. Geurts *J. Phys: Condens. Matter*, vol. 3, p. 9447, 1991.

Curriculum Vitae

Condensed Matter Theory Group
Department of Physics
Universiteit Antwerpen
Groenenborgerlaan 171 / U209
BE-2020 Antwerpen
email 1: hacarrillo@gmail.com
email 2: hamilton.carillonunoz@ua.ac.be

Education

2008 - 2012: Ph.D. in Physics, Universiteit Antwerpen, Belgium.
2006 - 2008: M.S. in Physics, Universidade Estadual de Campinas, Brazil.
2001 - 2006: B.S. in Physics, Universidad Industrial de Santander, Colombia.

Expertise

Programming languages: C/C++, Fortran 90
Finite differences method.
Non-equilibrium Green function method: Recursive Algorithm
Electronic transport in nanostructures and mesoscopic systems

Languages

	Listening	**Speaking**	**Reading**	**Writing**
English	good	fair	good	fair
Portuguese	good	good	good	fair
Spainish	Native	Native	Native	Native

Original publications

- **H. Carrillo-Nuñez**, Wim Magnus, William G. Vandenberghe, Bart Sorée and F. M. Peeters, *Band-to-band tunneling in the framework of the modified local density approximation*, manuscript in preparation.

- **H. Carrillo-Nuñez**, Wim Magnus, William G. Vandenberghe, Bart Sorée and F. M. Peeters, *Phonon-assisted Zener tunneling in a p-n diode silicon nanowire,* **Solid-State Elec., 79**, 196 (2013).

- Wim Magnus, **H. Carrillo-Nuñez** and Bart Sorée, *"The variational principle: a valuable ally assisting the self-consistent solution of Poisson's equation and semi-classical transport equations"*, **book chapter** in *CMOS Nanoelectronics: Innovative Devices, Architectures and Applications*, N. Collaert. Ed. Pan Stanford Publishing, September 2012.

- **H. Carrillo-Nuñez**, Wim Magnus, and F. M. Peeters. *A simplified quantum mechanical model for nanowire transistors based on non-linear variational calculus,* **J. App. Phys.**, **108**, 063708 (2010). Also selected for the September 27, 2010 issue of **Virtual Journal of Nanoscale Science & Technology**.

- **H. Carrillo-Nuñez** and Peter A. Schulz. *Localization of electronic states in finite ladder models: Participation ratio and localization length as measures of the wave-function extension,* **Phys. Rev. B**, **78**, 235404 (2008).

Conference proceedings

- **H. Carrillo-Nuñez**, Wim Magnus and F. M. Peeters. *A Non-linear variational principle for the self-consistent solution of Poisson's equation and a transport equation in the local density approximation*. Online by IEEE Xplore, Proc. of SISPAD 171 (2010). In: SISPAD 2010, Bologna, Italy.

- **H. Carrillo-Nuñez** and Peter A. Schulz. *Scrutinizing localization properties in heuristic models for DNA molecules: Localization lengths versus participation ratios*. Microelectronics Journal, **39**, 1220 (2008). In: 13th CLACSA 2008, Santa Marta Colombia.

- **H. Carrillo-Nuñez** , Oscar. L. Acevedo and Ilia D. Mikhailov. *Density of impurity states in flat quantum dots with different shapes*, Rev. Col. Fs., **39**, 127 (2007). In: 7th National School of Condense Matter Physics, Duitama, Colombia.

Main participations in events

- "*On the calculation of phonon-assisted band-to-band tunneling currents in Si nanowires*". (*Poster presentation*)
  H. Carrillo-Nuñez, Wim Magnus, W. Vandenberghe, Bart Sorée and F. M. Peeters
  International Workshop on Computational Electronics (IWCE). 22-25 May 2012, Madison, Wisconsin, USA.

- "*On the non-linear MLDA-based variational principle: the cases of Nanowires*". (*Poster presentation*)
  H. Carrillo-Nuñez, Wim Magnus, and F. M. Peeters
  International Physics School on Fundamentals of Nanoelectronics. 12-17 Febraury 2012, Tenerife, Spain.

- "*A Non-linear variational principle for the self-consistent solution of Poisson's equation and a transport equation in the local density approximation*". (*Oral presentation*)
  H. Carrillo-Nuñez, Wim Magnus and F. M. Peeters
  SISPAD 2010, International Conference on Simulation of Semiconductor Processes and Devices. September 2010, Bologna, Italy.

- Capri Spring School on Transport in Nanostructures: "non-equilibrium phenomena". Mar. 29 - Apr. 5 2009, Capri, Italy.

- " *Localization properties in heuristic models for DNA molecules: different localization definitions*". (*Poster presentation*)
  H. Carrillo-Nuñez and Peter A. Schulz
  29th ICPS, International Conference on the Physics of Semiconductors. July 2008, Rio de Janeiro, Brazil.

- "*Scrutinizing localization properties in heuristic models for DNA molecules: Localization lengths versus participation ratios*". (*Oral presentation*)
  H. Carrillo-Nuñez and Peter A. Schulz
  13th CLACSA, Latin American Conference on Surface Science and Applications. December 2007, Santamarta, Colombia.

- *Density of impurity states in flat quantum dots with different shapes*. (*Poster presentation*)
  H. Carrillo-Nuñez , Oscar. L. Acevedo and Ilia D. Mikhailov.
  7th National School of Condense Matter Physics. October 2006, Duitama, Colombia.